Electronic and Ionic Transport in

Carbon Nanotubes and Other Nanostructures

by

Di Cao

A Dissertation Presented in Partial Fulfillment
of the Requirements for the Degree
Doctor of Philosophy

Approved November 2011 by the
Graduate Supervisory Committee:

Stuart Lindsay, Chair
Sara Vaiana
Robert Ros
Robert Marzke
John Shumway

ARIZONA STATE UNIVERSITY

December 2011

ABSTRACT

This thesis describes several experiments based on carbon nanotube nanofludic devices and field-effect transistors. The first experiment detected ion and molecule translocation through one single-walled carbon nanotube (SWCNT) that spans a barrier between two fluid reservoirs. The electrical ionic current is measured. Translocation of small single stranded DNA oligomers is marked by large transient increases in current through the tube and confirmed by a PCR (polymerase chain reaction) analysis. Carbon nanotubes simplify the construction of nanopores, permit new types of electrical measurement, and open new avenues for control of DNA translocation. The second experiment constructed devices in which the interior of a single-walled carbon nanotube field-effect transistor (CNT-FET) acts as a nanofluidic channel that connects two fluid reservoirs, permitting measurement of the electronic properties of the SWCNT as it is wetted by an analyte. Wetting of the inside of the SWCNT by water turns the transistor on, while wetting of the outside has little effect. This finding may provide a new method to investigate water behavior at nanoscale. This also opens a new avenue for building sensors in which the SWCNT functions as an electronic detector. This thesis also presents some experiments that related to nanofabrication, such as construction of FET with tin sulfide (SnS) quantum ribbon. This work demonstrates the application of solution processed IV-VI semiconductor nanostructures in nanoscale devices.

DEDICATION

For my beloved parents and friends

ACKNOWLEDGMENTS

First of all, I'd like to give my special thanks to my advisor Professor Stuart Lindsay. He supports me through all my Ph.D. study for five years. He is a very kind person and has passion with discovery and innovation. His strong ability in social networking gives us changes to collaborate with other advanced groups in other university. In the research field, he gave me the directions and also leaves me enough freedom to do the research that I am interested in. He always encourage me and with patient during my difficult times. I really appreciate that I learned a lot of research methods in Lindsay's lab and started to build path to my further career here.

I also give special thanks to Dr. Jin He. Jin was in charge of all our experimental work. He guided me to the research and taught me a lot of skills in measurement and micro fabrication. His strong hardware and programming skills always solved the equipment malfunction problems. He also helped me with paper work for publications. His diligence and hard work make sure the great ideas come out into reality.

I want to thank Maggie Black, Michael Dodson and Steve Woodward who helped me a lot for technical issues, Feng Liang, Brett Gyarfas, Shuhui Wan for their assistance in the chemical and computer engineering.

I would to thank the carbon nanotube group in Lindsay's lab, including Pei Pang, Hao Liu, Tao Luo and Weisi Song. We share progress and ideas with each other. They also assisted me in the fabrication work.

I also feel grateful to be able to work with my colleagues: Qiang Fu, Shuo Huang, Shuai Chang, Yanan Zhao, Sen Peng, Padmini Krishnakumar, Parminder Kaur. They give me lots of fun of the life in the lab.

These faculty members also gave me invaluable help in research. Dr. Hao Yan's group collaborated with our group for Plasmon Printing (Suchetan Pal) and Quantum Ribbon (Dr. Zhengtao Deng) project. Dr. Su Lin helped me with optics equipments. Dr. Nongjian Tao's group helped me with electronics and hardware. Dr. John Shumway and Dr. Peiming Zhang help our group in the recognition project.

I also acknowledge valuable discussions in DNA translocation and modeling for CNT water wetting with Dr Jinyao Tang, Dr. Haitao Liu, Dr. Collin Nuckolls, Dr. P. Krstic, Dr. S. Joseph, and Dr. J. H. Park.

The experiments in my thesis were supported by the grants from the DNA sequencing technology program of the National Human Genome Research Institute (1R21HG004770-01, 1RC2HG005625-01), Arizona Technology Enterprises and the Biodesign Institute. This research used resources of the Oak Ridge Leadership Facility at the Oak Ridge National Laboratory. We also acknowledge the use of nanofab within Center for Solid State electronic research (CSSER) and SEM and TEM within the Center for Solid State Science (CSSS) at Arizona State University.

TABLE OF CONTENTS

Page

CHAPTER Page

LIST OF TABLES

Table Page

LIST OF FIGURES

Figure Page

Figure Page

Figure Page

Parts of this dissertation include collaborative published work, in which I am as the first, the second listed co-author or later.

Chapter 4 is adapted with permission from Haitao Liu, Jin He, Jinyao Tang, Hao Liu, Pei Pang, Di Cao, Predrag Krstić, Sony Joseph, Stuart Lindsay and Colin Nuckolls. The reported experiments were performed by Haitao Liu, Jin He, Jinyao Tang, Hao Liu, Pei Pang and Di Cao under the guidance of Stuart Lindsay and Colin Nuckolls. Haitao Liu and Jin He performed the measurement and data collection. Hao Liu ran the quantitative polymerase chain reaction (QPCR). Both Pei Pang and Di Cao did device fabrication work and parts of the measurement. Predrag Krstić and Sony Joseph performed theoretical simulations. Stuart Lindsay and Colin Nuckolls wrote the manuscript. The results were separately published in two journals: Science (DNA translocation) and Journal of Physics: Condensed Matter (nucleotide translocation as a review report).

Chapter 5 is adapted with permission from Di Cao, Pei Pang, Jin He, Tao Luo, Jae Hyun Park, Predrag Krstić, Colin Nuckolls, Jinyao Tang and Stuart Lindsay. The reported experiments were performed by Di Cao and Pei Pang under the guidance of Stuart Lindsay and Jin He. Both Di Cao and Pei Pang did device fabrication work and performed the measurement and data collection. Tao Luo grew carbon nanotubes. Jin He did the data analysis. Predrag Krstić and Jae Hyun Park performed theoretical simulations. Colin Nuckolls and Jinyao Tang carried out primary measurement work and shared helpful discussion. Stuart Lindsay and Jin

He wrote the manuscript. The results from this work were published in ACS Nano.

Chapter 7 is adapted with permission from Zhengtao Deng, Di Cao, Jin He, Stuart M. Lindsay, Hao Yan, Yan Liu. The reported experiments were performed by Zhengtao Deng and Di Cao under the guidance of Hao Yan and Stuart Lindsay. Zhengtao Deng did SnS nanoribbons synthesis and structure and TEM measurements. Di Cao finished the nanoribbon based field effect transistor device fabrication work and performed the measurement, data collection and part of the data analysis. Zhengtao wrote the manuscript, which was and modified by Hao Yan, Stuart Lindsay and Jin He. The results from this work were submitted to Angewandte Chemie.

Chapter 1

INTRODUCTION

This thesis describes several experiments that form part of a project to develop a new DNA sequencing technology called “Sequencing by Recognition”, proposed by Professor Stuart Lindsay in the Biodesign Institute, Arizona State University. Carbon nanotubes (CNT) can be used as combined nanochannel and readout electrodes for DNA detection.

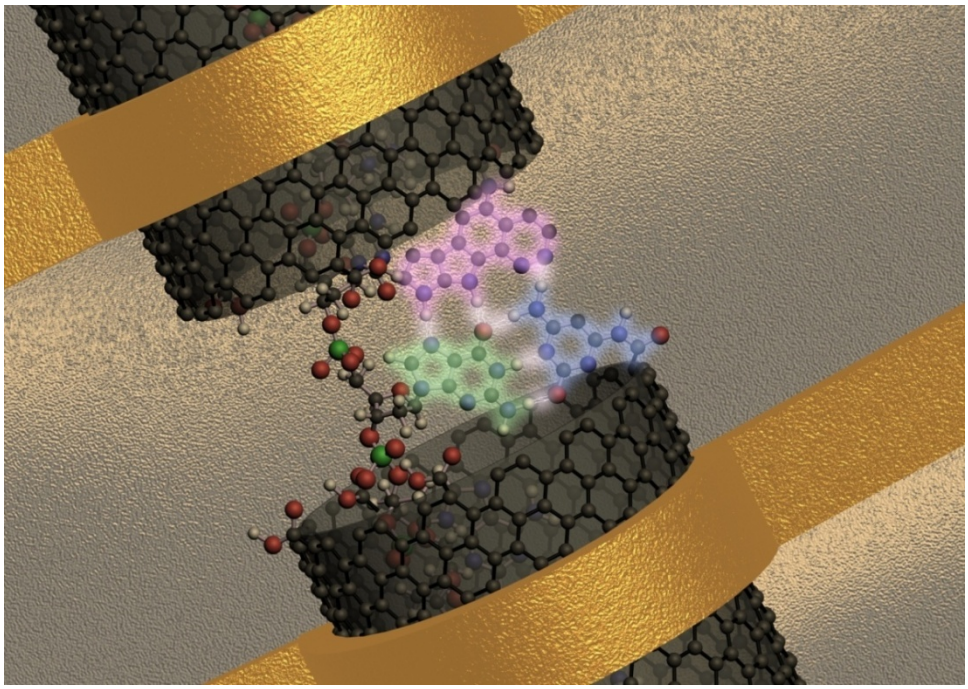

Figure 1.1 DNA Sequencing by Recognition proposed by Dr. Stuart Lindsay at ASU

In Figure 1.1, a recognition molecule is attached on the electrode, reading a specific DNA base[1]. As the ssDNA passes the electrode readers via the CNT, the sequence is identified. To utilize CNT as a nanopore or nanochannel, it is important to first understand the transport properties through CNT[2]. Carbon

nanotube (CNT) based Nanofluidic devices are studied in my experiments (see Chapter 4); they show their special electrical and mechanical properties for DNA translocation.

The exploration of carbon nanotubes as 1D transport systems is not limited to DNA sequencing; they also have the potential to form the basis of new types of electronic sensor. The electronic properties, small size and large surface to volume ratio of single-walled carbon nanotubes (SWCNT) give them particular sensitivity as transistors. Jinyao Tang at Columbia University [3] found that the CNT-FET becomes insensitive to gating after the CNT was filled with water, see figure 1.2. We will do further research in this direction and also explore the effect of other solvents such as acids and bases, see Chapter 5 and 6.

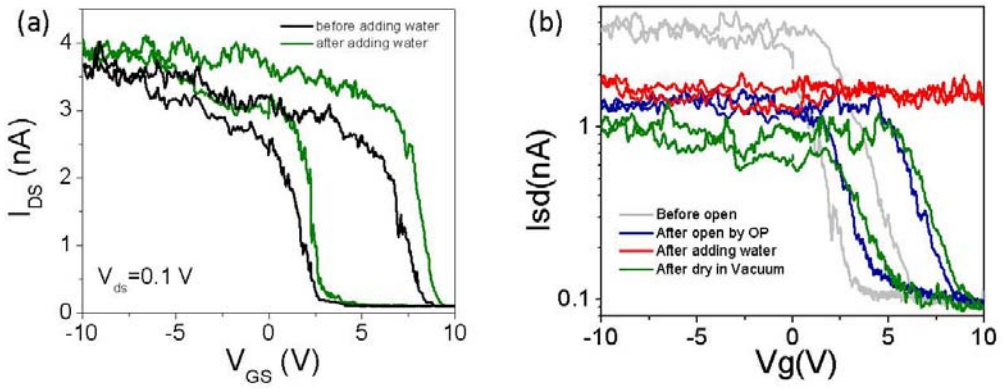

Figure 1.2 a) Electrical response to water filling into the reservoir of the intact nanotube device. b) Electrical response to water filling of the nanotube device after plasma treatment.

In Chapter 2, the basic theory of carbon nanotube is discussed, including structure, electronic characteristics, and field-effect transistor (FET) principle.

Chapter 3 discusses the growth of carbon nanotube and fabrication of carbon nanotube based nanofluidic channel and field-effect transistors.

Chapter 4 describes direct electrical measurement of molecules and small ssDNA transport through CNT nanofludic device, in which one SWCNT spans a barrier between two fluid reservoirs. The signals are described and analyzed.

Chapter 5 elucidates the effect of water filling to the electron transport properties of CNT devices. By building field-effect transistor connections onto the SWCNT nanofluidic channel, we have discovered that internal wetting of the SWCNT by water turns semiconducting tubes on, and renders them insensitive to gating, mimicking metallic behavior.

Chapter 6 takes one step further to discuss the filling effect of salt solutions, including different concentration, different pH values, and different ion sizes. We demonstrate that the electrical properties of SWCNT are also sensitive to the ionic solution inside. Discussion in Chapter 5 and Chapter 6 opens a new avenue for building sensors in which the SWCNT simultaneously functions as a concentrator, nanopore and extremely sensitive electronic detector, exploiting the enhanced sensitivity of the interior surface.

Chapter 7 describes project utilizing other types of nanostructures. In the quantum ribbon project, we constructed FET with a new semiconducting material, tin sulfide, a SnS quantum ribbon.

Chapter 8 briefly discusses the future directions and the major problems for Nanofabrication.

Chapter 2

CARBON NANOTUBE FUNDAMENTALS

This chapter will introduce the background for the physical and electronic structure of carbon nanotubes (CNT). We start from the structure of graphene, then go forward to form the structure of carbon nanotubes. We will discuss how the structure influences the electronic properties, such as band gap and density of states of carbon nanotubes. The metallic and semiconducting properties will influence the translocation of ions through CNT; this is discussed in Chapter 4. The semiconducting CNT will be discussed in detail to explain the field effect phenomenon when it is fabricated on the silicon dioxide substrate. This is the basis for water wetting experiments shown in Chapters 5 and 6.

2.1 The structure of carbon nanotubes

A carbon nanotube can be imagined as graphene rolled up into a tube [4]. Graphene is a single layer sheet of sp^2 bonded carbon atoms is packed in a honeycomb crystal lattice. The structure of graphene is shown in Figure 2.1. The unit cell is the grey diamond that contains two atoms. The lattice vectors are shown as $\overrightarrow{a_1}$ and $\overrightarrow{a_2}$ [5]. Graphite has multiple layers stacked on top of each other. Since our experiments using single-walled carbon nanotube, the graphene structure (a single layer of graphite) is discussed here.

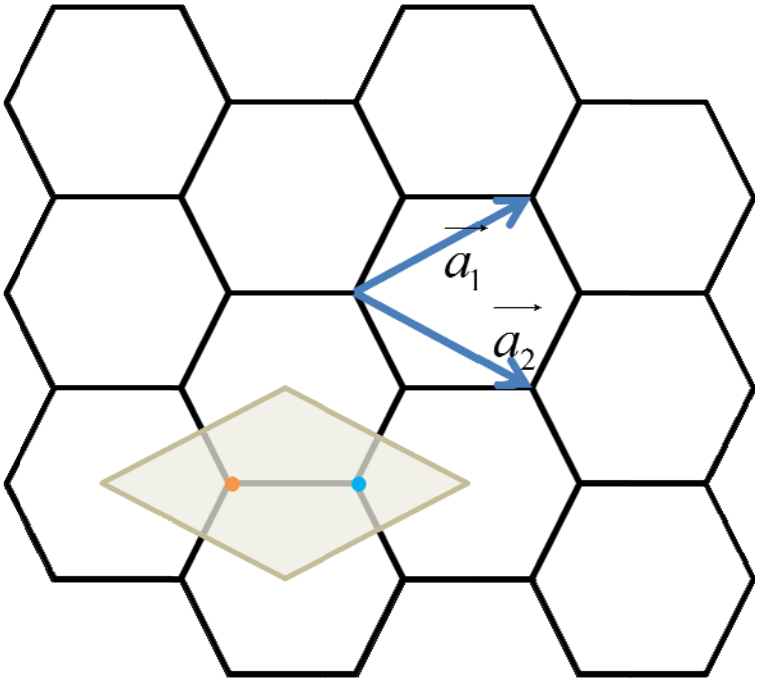

Figure 2.1 The structure of graphene. The lattice vectors are the blue arrows, the unit cell is the grey diamond.

The lattice vectors have equations:

$$\vec{a}_1 = -\frac{a}{2}\vec{x} + \frac{a\sqrt{3}}{2}\vec{y} \tag{2.1}$$

$$\vec{a}_2 = \frac{a}{2}\vec{x} + \frac{a\sqrt{3}}{2}\vec{y} \tag{2.2}$$

We have:

$$\vec{a}_1 \bullet \vec{a}_1 = \vec{a}_2 \bullet \vec{a}_2 = a^2 \tag{2.3}$$

$$\vec{a}_1 \bullet \vec{a}_2 = \frac{a^2}{2} \tag{2.4}$$

The lattice constant $a = \sqrt{3} \times a_{c-c} = 0.246nm$, while a_{c-c} is the bond length of two carbon atoms[6].

The structure of a carbon nanotube is formed by rolling up a graphene sheet into a cylinder. If more than one layer of graphene is rolled around each other, forming N concentric tubes, it is called a multi-walled carbon nanotube (MWCNT). If only one layer of graphene is rolled in to a cylinder, it is called single-walled carbon nanotube (SWCNT). In our fabrication, most carbon nanotubes are single-walled carbon nanotubes. So we restrict our discussion to single-walled carbon nanotubes.

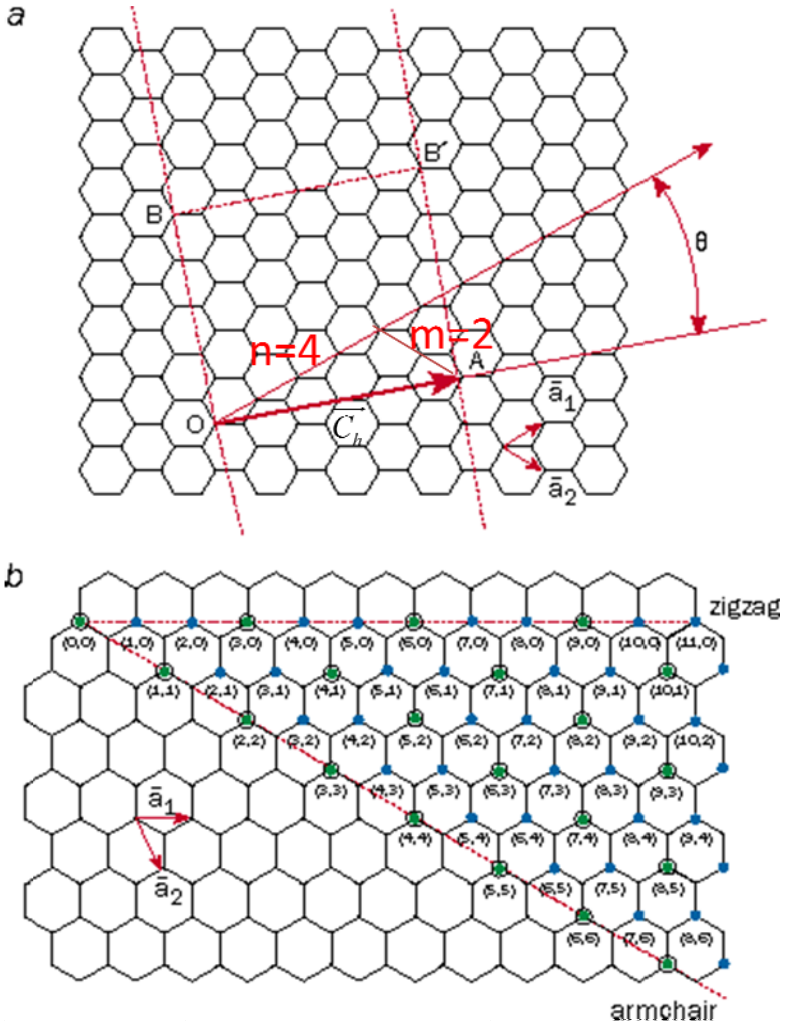

Figure 2.2 A carbon nanotube is based on a two-dimensional graphene sheet (adapted from ref. [7]). (a) The chiral vector is defined on the hexagonal lattice as $C_h = n\hat{a}_1 + m\hat{a}_2$, where $\hat{a}_1$ and $\hat{a}_2$ are unit vectors, and *n* and *m* are

integers. The chiral angle, θ, is measured relative to the direction defined by â$_1$. This diagram has been constructed for (n, m) = (4, 2), and the unit cell of this nanotube is bounded by OAB'B. To form the nanotube, imagine that this cell is rolled up so that O meets A and B meets B', and the two ends are capped with half of a fullerene molecule. Different types of carbon nanotubes have different values of n and m. (b) Zigzag nanotubes correspond to (n, 0) or (0, m) and have a chiral angle of 0°, armchair nanotubes have (n, n) and a chiral angle of 30°, while chiral nanotubes have general (n, m) values and a chiral angle of between 0° and 30°. According the theory, nanotubes can either be metallic (green circles) or semiconducting (blue circles).

Figure 2.2a shows how a graphene layer rolled up to form a nanotube. AB′BO is the unit cell of this carbon tube. To form the tube, the graphene is rolled up so that O meet A and B meet B′. The vector $\overrightarrow{C_h}$ describes the integer combination of the lattice vectors. $\overrightarrow{C_h}$ is defined as the chiral vector. In general, chiral vector is written as:

$$\overrightarrow{C_h} = n\overrightarrow{a_1} + m\overrightarrow{a_2} \tag{2.5}$$

The length of the chiral vector is:

$$\left|\overrightarrow{C_h}\right| = \left|n\overrightarrow{a_1} + m\overrightarrow{a_2}\right| = a\sqrt{n^2 + m^2 + nm} = \sqrt{3}a_{c-c}\sqrt{n^2 + m^2 + nm} \tag{2.6}$$

Where n and m are integers, by convention n≥m [8]. The chiral angle θ is measured relative to the direction of $\overrightarrow{a_1}$. In the figure, (n,m)=(4,2). The different n and m numbers define the different types of carbon nanotubes. If one number is zero, like (n,0) , the chiral angle is 0°, we call it a zigzag nanotube. If n=m, while a chiral angle is 30°, we call it an armchair nanotube. In general, n and m can be random numbers, and chiral angle varies between 0° and 30°, we call it a chiral nanotube[6]. See Figure 2.3 for examples.

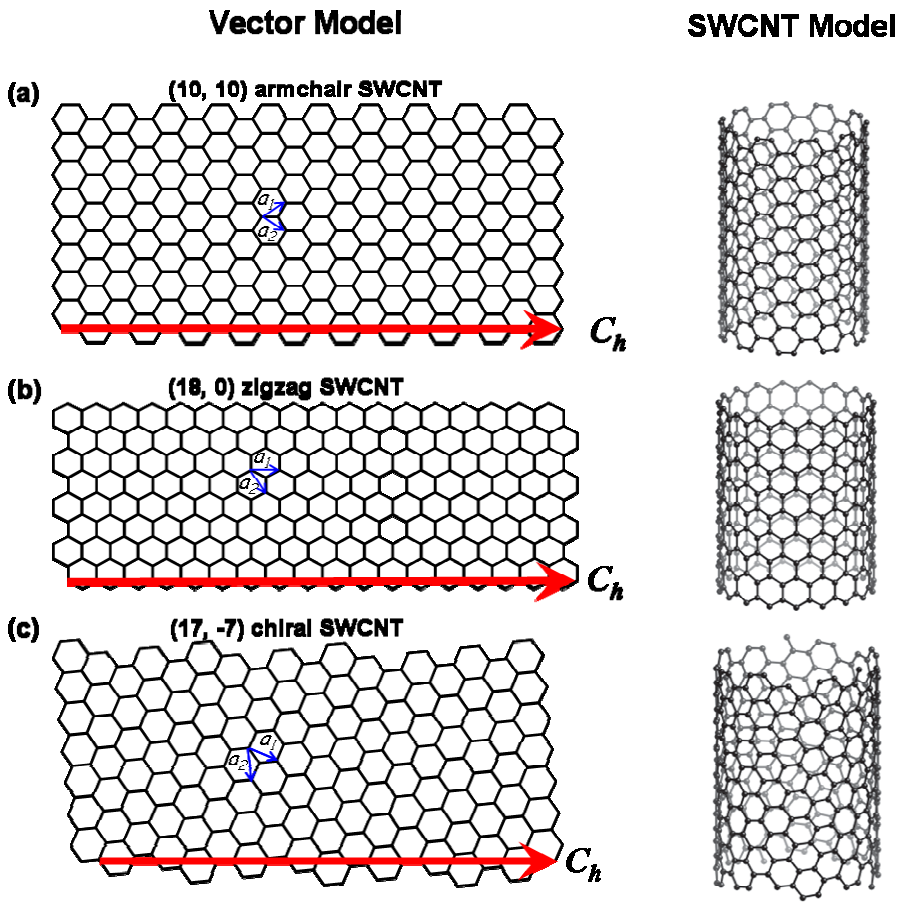

Figure 2.3 Schematic illustration of the SWCNT chirality: (adapted from ref.[6]) (a)–(c) armchair (10,10), zigzag (18,0) and chiral (17,-7). The left column shows the rolling of graphene sheets to a carbon nanotube, illustrating the chiral vector $\boldsymbol{C}_h$ with respect to the unit vectors $\boldsymbol{a}_1$ and $\boldsymbol{a}_2$ in the honeycomb crystal lattice of the graphene. The right column displays the corresponding SWCNT models.

The properties of nanotubes are determined by the chiral angle and diameter, which is defined by n and m. the diameter d is simply the length of the chiral vector divided by π:

$$d = \frac{\left|\overrightarrow{C_h}\right|}{\pi} == \frac{\sqrt{3}}{\pi} a_{c-c} \sqrt{n^2 + m^2 + nm} \tag{2.7}$$

Bending the planar π bonds into a cylinder results in a decrease of bonding energy, which gives a limit of 0.7nm diameter for stable carbon nanotube[6].

The chiral angle is given by

$$\tan^{-1}\left(\sqrt{3}n/(2m+n)\right) \tag{2.8}$$

The measurement of diameter and chiral angle is done by scanning tunneling microscopy and transmission electron microscopy, but it is very difficult to measure diameter and chiral angle at the same time as measuring another physical property. Microscopy is difficult because the tube is so small and the carbon atoms are in constant thermal motion, and it is very easy to damage the tube by the electron beam in the microscope.

AB′BO is the unit cell of this carbon tube. The unit cell of a nanotube contains N hexagons, each of which contains two carbon atoms; thus the unit cell of a nanotube contains 2N carbon atoms. If the unit cell of a nanotube is *N* times larger than that of a hexagon, the unit cell of the nanotube in reciprocal space is 1/*N* times smaller than that of a single hexagon.

There is no theoretical limit to the length of the carbon nanotube[9]. In our lab, the longest CNT can be as long as centimeters, so the length to diameter ratio can be as high as seven orders of magnitude. The end of the carbon nanotube can be capped with carbon atoms in hexagons and pentagons[7]. But in our experiments, carbon nanotubes with open ends were used, achieving by burning the carbon nanotube ends in an oxygen plasma.

2.2 Electrical properties of CNT

The electronic structures of a carbon nanotube and graphene are similar. The band structure of carbon nanotube is modified by its reduced dimensionality. We will

first discuss the band structure of graphene, and then discuss how the carbon nanotube chirality determines its electrical properties. We will show how the semiconducting and metallic nature of carbon nanotubes and their density of states are determined.

2.2.1 Electrical structure of graphene

The graphene planar arrangement of carbon atoms result from sp^2 hybridization, with three bond direction of 120° between them. Figure 2.4a show the graphene lattice, the diamond area is the unit cell, A and B are inequivalent sites marked with orange and blue.

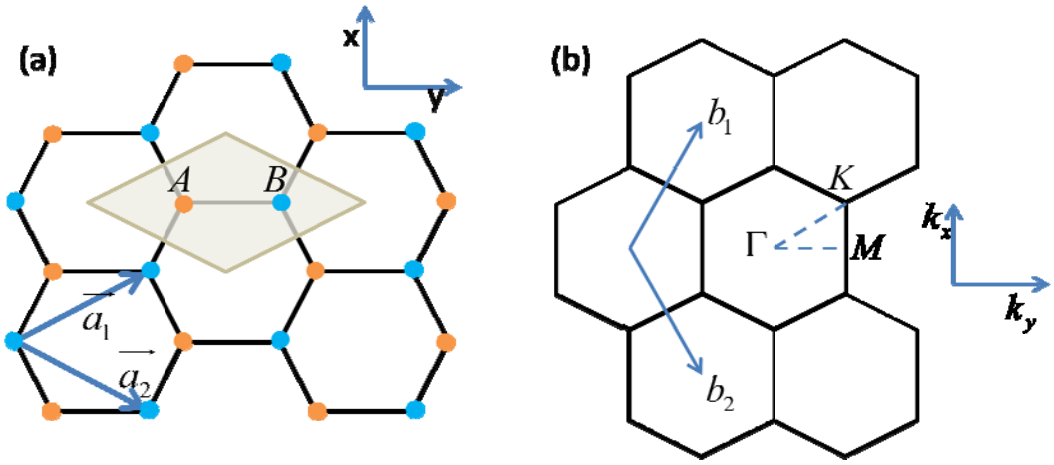

Figure2.4 (a) the lattice of graphene (b) the reciprocal lattice of graphene

Figure 2.4b show the reciprocal lattice of graphene, it shows the momentum states, $\vec{k}$, available to electrons in the graphene [10]. The first Brillouin zone is also a hexagon, with reciprocal lattice vectors:

$$\vec{b_1} = -\frac{2\pi}{a}\vec{k_x} + \frac{2\pi}{a\sqrt{3}}\vec{k_y} \tag{2.9}$$

and

$$\vec{b_2} = +\frac{2\pi}{a}\vec{k_x} + \frac{2\pi}{a\sqrt{3}}\vec{k_y} . \qquad (2.10)$$

In Figure 2.4b, some points of high symmetry are labeled. Γ is the center of hexagon where $\vec{k} = 0$. The middle point of the Brillouin zone boundary is marked as M, where $\vec{k} = \frac{2\pi}{a\sqrt{3}}\vec{k_y}$.

The vertices of the Brillouin zone, marked by K and K', are called Dirac points. There are three K and K' points in one Brillouin zone, each are equivalent to each other. The K and K' points are where $|\vec{k}| = \frac{4\pi}{3a}$ has its maximum value.

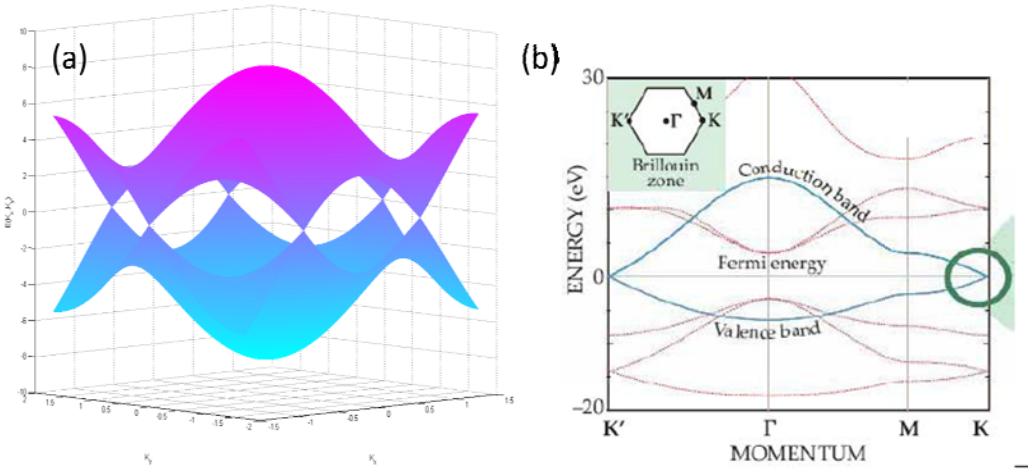

Figure 2.5 3-D and 1D model of band structure of graphene (b is adapted from Ref. [11])

Figure 2.5 shows the 3-D and 1D model of band structure of graphene. Figure 2.5a shows the allowed energy values for different $\vec{k}$. Figure 2.5b is the cross section of the first Brillouin zone. We can find that at K and K' points, the conduction band touches the valence band. From sp^2 hybridization, three electrons form the bonds, leaving one electron free for each atom. One unit cell has two

atoms, which has two free electrons. The two electrons fill the valence band, leaving graphene as a zero band-gap semiconductor[12].

At the K and K' points the band-gap is 0eV. At the Γ point, the band-gap is 16.2eV. At the M point, the band-gap is 5.4eV [13]. The fact that the valence band and conduction band touch means that there are available states for electrons to transit from valence band to conduction band, so graphene can be considered as a conductor.

Rolling the graphene sheet into a carbon nanotube restricted the graphene band structure. The periodic boundary condition along $\overrightarrow{C_h}$ quantize the graphene band structure. First we define translational vector $\vec{T}$ along the carbon nanotube axis, while $\overrightarrow{C_h}$ is along circumferential direction (perpendicular to $\vec{T}$), and we define reciprocal lattice vectors $\overrightarrow{K_1}$ in the circumferential direction and $\overrightarrow{K_2}$ along the axis. We have

$$\overrightarrow{C_h}\bullet\overrightarrow{K_2}=0\ ,\ \vec{T}\bullet\overrightarrow{K_2}=2\pi \tag{2.11}$$

$$\overrightarrow{C_h}\bullet\overrightarrow{K_1}=2\pi\ ,\ \vec{T}\bullet\overrightarrow{K_1}=0\ . \tag{2.12}$$

Where $\overrightarrow{K_1}$ and $\overrightarrow{K_2}$ are given by:

$$\overrightarrow{K_1}=\frac{1}{N}(-t_2\vec{b_1}+t_1\vec{b_2}) \tag{2.13}$$

$$\overrightarrow{K_2}=\frac{1}{N}(m\vec{b_1}-n\vec{b_2})\ . \tag{2.14}$$

The wave vector is quantized along the $\overrightarrow{C_h}$ direction, but remains continuous along the $\vec{T}$ direction. The energy bands of carbon nanotube are made up with a set of one dimensional energy dispersion relations that are cross sections of the band structure of graphene.

The one dimensional energy dispersion relations are [14]

$$E_{CNT}^{\nu}(k) = E_{g-2D}(k\frac{\overrightarrow{K_2}}{|K_2|} + \nu\overrightarrow{K_1}) \quad , \tag{2.15}$$

where $-\pi / T < k < \pi / T$ is a one-dimensional wave-vector along the CNT axis and $\nu = 1,...,N$. The periodic boundary condition for a CNT gives discrete values in the circumferential direction. The N pairs of energy dispersion curves given by (2.15) correspond to the cross sections of the two-dimensional energy dispersion surface of graphene.

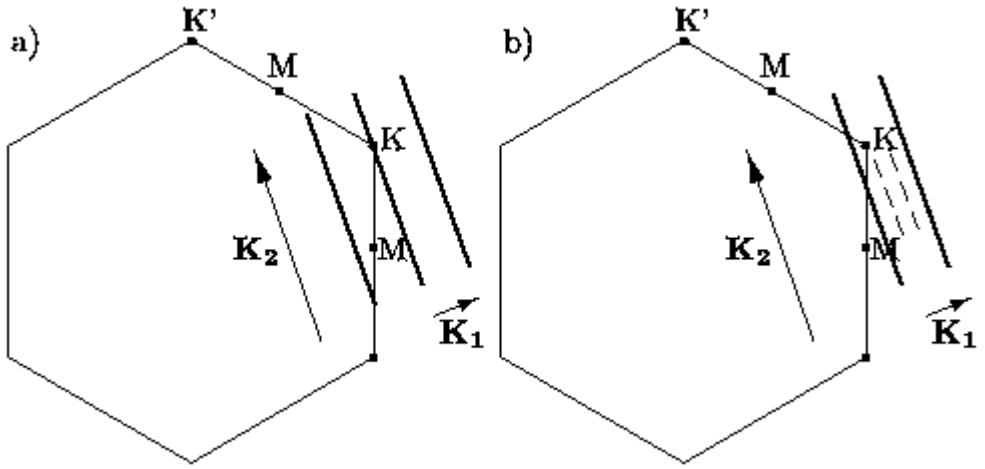

Figure 2.6 One dimensional available wave-vector (bold lines) k in the Brillouin zone of graphene(adapted from Ref. [6]) (a)for metallic CNTs (b) for semiconducting CNTs

Figure 2.6 shows several cutting lines near one of K points. The cutting line corresponds to an allowed $\vec{k}$ value in the band structure of the carbon nanotube. The distance between 2 adjacent lines is given by $\left|\overrightarrow{K_1}\right| = 2/d_{CNT}$ and the length is given by $\left|\overrightarrow{K_2}\right| = 2\pi/T$. If the cutting line pass through K or K' points, the band gap is zero, resulting in a conducting carbon nanotube. If the cutting line misses the K and K' points, there is a finite band-gap between the valence band and conduction band, resulting in a semiconducting nanotube. In general, for a (n,m) carbon nanotube, if n-m can be divided exactly by 3, this gives a metallic carbon nanotube. If not, this gives a semiconducting nanotube.[15]

It is predicted that the larger the diameter of a semiconducting carbon nanotube, the smaller the bandgap [6], as demonstrated by experiment by Jeroen [16]. The smallest stable CNT has a bandgap around 1eV. This gives an opportunity to customize the bandgap of semiconducting CNT based on the diameter, which can be a direction of further research.

2.2.2 DOS of carbon nanotube

The electrical properties of carbon nanotube are determined by the density of states. Figure 2.7 shows the density of state of metallic and semiconducting nanotubes. For metallic carbon nanotube, the density of state is constant between valence band and conducting band. For a semiconducting nanotube, the density of states is zero between valence band and conducting band, having peaks at the edge of the band-gap. The transport properties of nanotubes are intimately related to their electronic band structure. The band gap for semiconducting carbon

nanotubes is predicted to be $E_g \sim 0.7eV / d_t(nm)$. Small band-gap nanotubes normally have a band gap less than 100mV. When the Fermi level is tuned into the band-gap, the semiconducting tube of large band-gap shows a broad region of near-zero conductance since $E_g \gg k_B T$, while a small band-gap tube shows only moderate dip in conductance since its band-gap is comparable to $k_B T$.

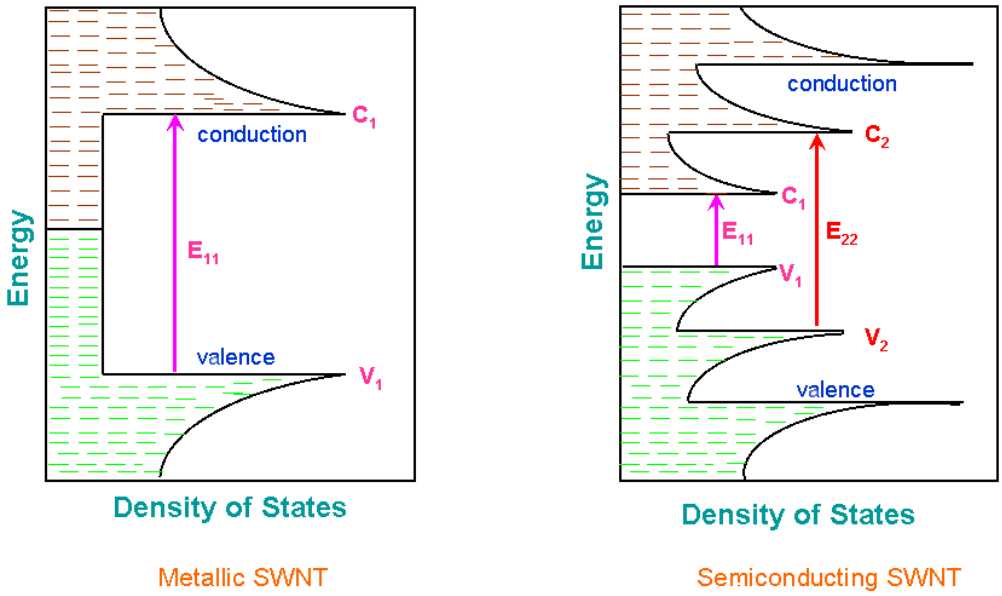

Figure 2.7 DOS of metallic and semiconducting CNT(adapted from Ref. [17])

Optical properties of carbon nanotubes derive from electronic transitions. The one dimensional material DOS has a feature that it is not a continuous function energy, but decrease gradually then increase in spikes. The sharp peaks in one dimensional material are called Van Hove singularities. Different nanotube structures have different energies between Van Hove singularities. It is relatively easy to detect optical signals from individual nanotubes and selectively excite certain indices (n,m) carbon nanotubes.

Good ohmic contacts made to metallic single-walled carbon nanotubes (SWNTs) have revealed them to be ballistic conductors that exhibit two units of quantum conductance, $4e^2/h$ ($R_Q = h/4e^2 = 6.5\ \mathrm{k}\Omega$) [18]. Metallic nanotubes have been reported to often approach such a quantized conductance value even at room temperature. Semiconducting nanotubes devices have a conductance within 25% of this theoretical limit [19, 20]. Additional resistance from the contacts can result in smaller conductance. At room temperature, the main origin of the resistivity at low bias in high-quality metallic single-walled nanotubes (SWNTs) is believed to be scattering by acoustic phonons. The scattering is weak, resulting in long mean-free paths at room temperature. Both measurements and calculations put the mean-free path in the range of a few hundred nanometers to several micrometers. At high biases, electrons gain enough energy to emit optical or zone-boundary phonons. Yao et al. showed that this scattering is very effective, leading to a saturation of the current at ~20 *u*A[21] at high biases.

2.3 Carbon nanotube field effect transistor (CNT-FET)

The semiconducting CNTs have general semiconducting electrical properties. They have an energy band gap in their band structure and conduct poorly when the Fermi level lies within the gap. An intrinsic semiconducting CNT can be doped with the environment, such as contact metals, as discussed later. P-type carbon nanotubes are made under typical experimental conditions. They are doped with an excess of positive charge. Otherwise, the Fermi level position along the axis of a semiconducting nanotube can be tuned capacitive by a

nearby electrode. This is analogous to the gate electrode of a metal-oxide-semiconductor field-effect transistor (MOSFET). Positive potential attraction results in negative charge builds up in the nanotube. The additional charge bends the valence and conduction bands relative to the Fermi level in the nanotube. This change the conductivity along the whole carbon nanotube [22].

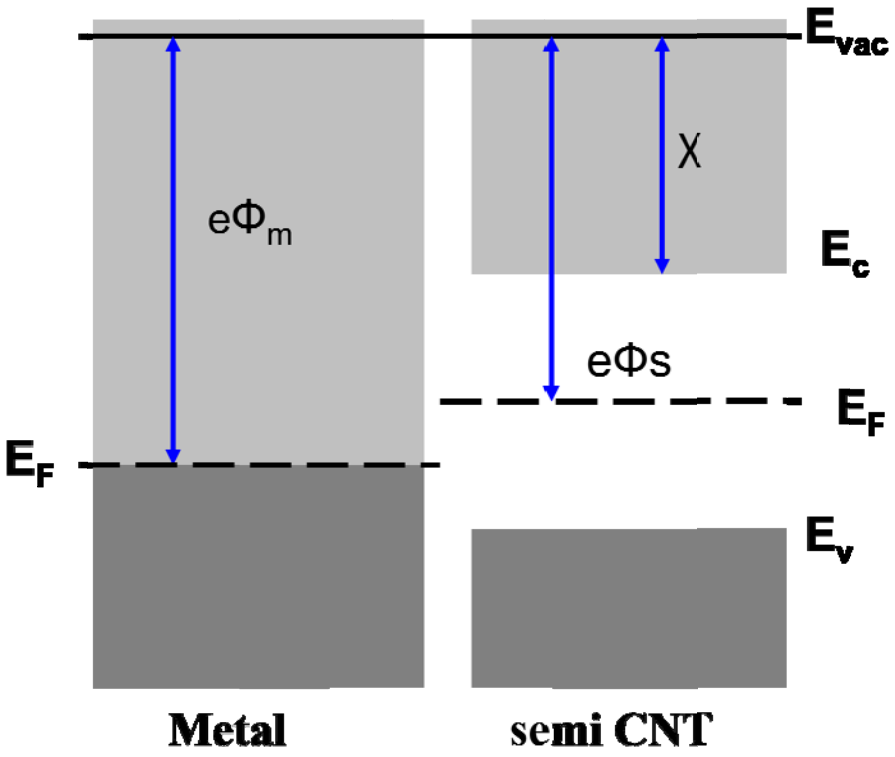

Figure 2.8 Fermi level of CNT lines up with the Fermi level of electrode before contact.

Figure 2.8 shows how the Fermi level of CNT lines up with the Fermi level of the electrode before contact. For an intrinsic semiconductor, the Fermi level of CNT is midway between the valence band and conducting band energies. The work function Φ_m is the difference between the Fermi energy of metal and the vacuum energy. In the same way, Φ_s is defined as the work function of the carbon

nanotube. The typical CNT work function is 4.5eV. When a CNT makes contact with electrodes regularly, if the work function of metal is larger than the work function of CNT ($\Phi_m > \Phi_s$), such as Pd (5.1eV), Au (5.1eV), Pt (5.7eV), the Fermi level of electrode tends to line up with the valence band of the CNT and form a p-channel for hole transport through the CNT. In contrast, if the work function of metal is smaller than the work function of CNT ($\Phi_m < \Phi_s$), such as Scandium (Sc) (3.5eV), the Fermi level of electrode tends to line up with the conduction band of the CNT and form an n-channel for electron injection from the metal electrode into the CNT.

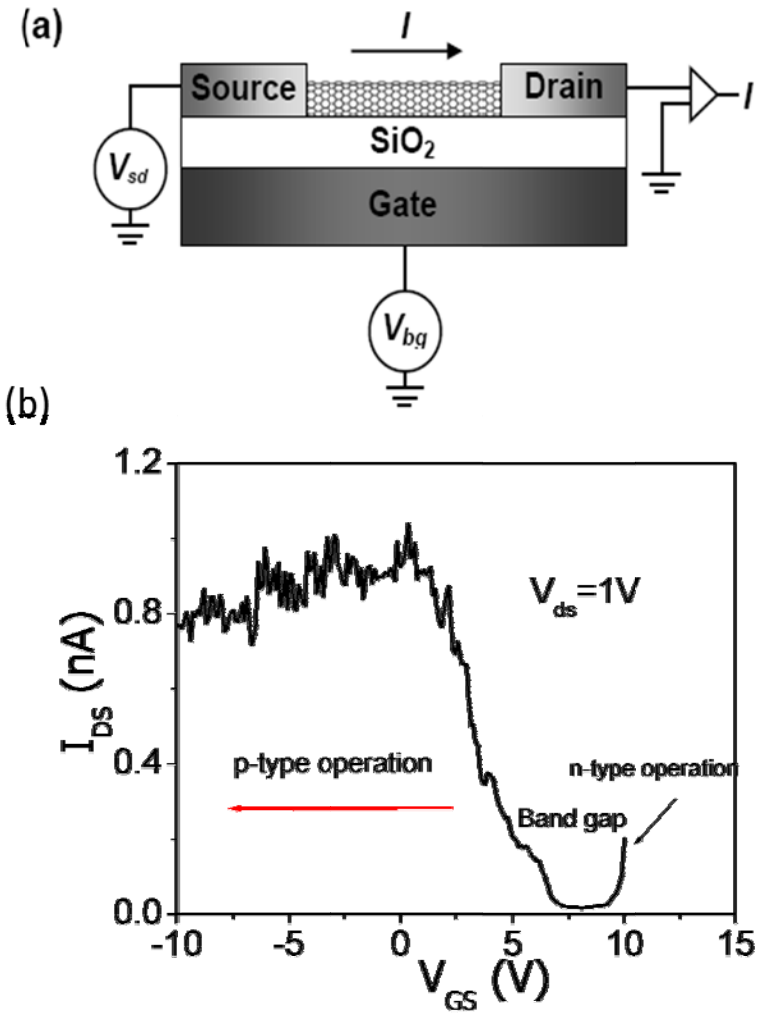

Figure 2.9 the I_{ds}-V_{gs} for a real ambipolar device. (a) is the basic structure of carbon nanotube field effect transistor (CNT-FET) (b) For I_{ds} curve, the p-type, band gap and n-type regions are indicated.

Under typical experimental conditions, we use gold (Au) as electrodes, so the CNTs are doped with positive charge by electron injection into the metal, resulting in a p-type channel. Transport in semiconducting nanotubes happens primarily due to holes. Generally the Fermi level is within the valence band when gate voltage is zero. Sweeping the gate voltage, however, can deplete the

semiconducting nanotube and turn it off. See Figure 2.9 for an example of a semiconducting nanotube. Figure 2.9a shows the typical structure of the carbon nanotube field effect transistor (CNT-FET). Two electrodes directly contact with the carbon nanotube, called the *source* and the *drain* electrode. A source-drain bias (V_{ds}) is applied to the source and drain electrode, directly contact with CNT, while the source-drain current (I_{ds}) is recorded. The dielectric silicon dioxide and the heavily doped p-type silicon substrate functions as a *back gate electrode*. A gate bias V_g is applied here with respect to the source. Figure 2.9b shows a p-type behavior at lower gate voltage. When $V_g \leq 0V$, the source-drain current is relatively stable (~1nA). With larger positive gate voltage, I_{sd} decrease rapidly, similar to the creation of an inversion layer in a MOSFET. Between a region 7V~10V, the source-drain current is almost zero (as low as 0.001nA compared with 1nA at negative gate voltage). This shows the band gap for a specific carbon nanotube. Given enough positive gate voltage, I_{sd} rises back, corresponding to n-type behavior. The conductance of the p-type region is 4~5 times larger than the n-type region. There is typically an intrinsic built-in barrier to n-type conduction. This results in a higher resistance for n-type transport relative to p-type transport [23]. Figure 2.9 illustrates the experimental results for an ambipolar device; the band model for p and n-type transport is discussed in Figure 2.10 for a similar device.

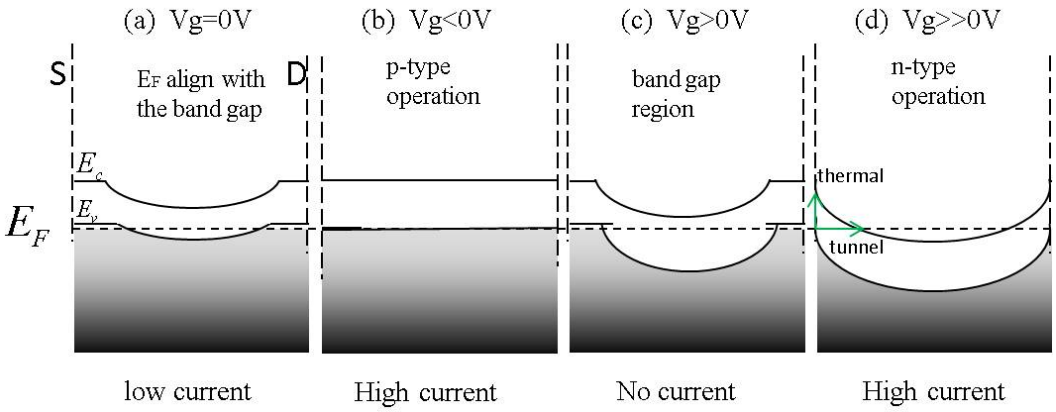

Figure 2.10 Energy vs. distance diagrams along the length of the carbon nanotube for a typical CNT-FET. (a) V_g=0, the Fermi level align with the valance band (b) negative gate voltage bend upward the bands, gives p-type behavior. (c) positive gate voltage bend downward the bands, turn off the FET. (d) When positive voltage is large enough, the bottom of the conduction band can be pulled below the Fermi level in the nanotube, gives n-type behavior.

Figure 2.10 shows the band diagrams along the length of a carbon nanotube attached to electrode contacts at both ends. E_c is the conduction band edge, E_v is the valence band edge. E_F is the Fermi level of metal contacts. S and D are the source and drain contacts. Typical metals make ohmic p-type contacts to carbon nanotubes. In this case Figure 2.10a represents zero gate voltage. Thermally excited carriers may aid transport. The band gap slightly bends downward because of injection of electrons to the metals, leaving holes in carbon nanotube as the carriers. There are no voltage drops either at the contact regions or in the gate dielectric (for V_g=0). Any small bias applied between source and drain will make carriers flow across the device. A negative gate voltage pulls the above the Fermi level, see Figure 2.10b, the Fermi level falls within the valence band, giving a high current. The CNT-FET is turned on. A positive gate voltage pulls

the bands below the Fermi level, and the nanotube is depleted of carriers in the bulk, as shown in Figure 2.10c. The CNT-FET is turned off. This gives extremely low or no current; the on-off ratio can be as high as five orders of magnitude. A more positive gate voltage pulls the conduction band edge below the Fermi level, shown in Figure 2.10d. This gives n-type operation; the current is several orders higher than Figure 2.10c but still lower than p-type operation. The carriers go through the band gap by tunneling from valence band states to conduction band states (horizontal arrow) and thermal activation of electrons over the band gap barrier (vertical arrow). Since the band gap is inversely proportional to diameter, both mechanisms become more relevant in larger diameter nanotubes[6]. The barrier for n-type conduction can be interpreted as a series contact resistance, explaining why experimentally observed p-type conduction is larger than n-type conduction (for p-type contacted nanotubes shown in Figures 2.9 and 2.10). Carbon nanotubes with comparable p- and n-type conductance are called *ambipolar* [24].

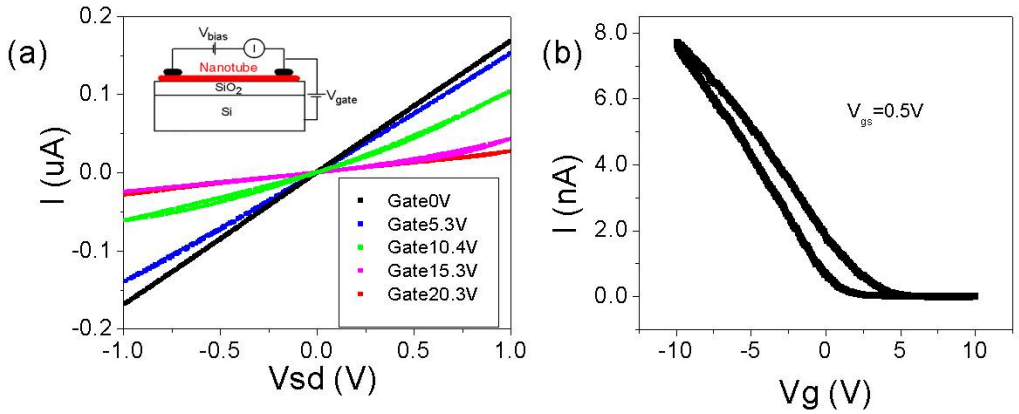

Figure 2.11 Typical behavior for a p-type CNT-FET. (a) The IV curve modified by the back gate, inset is the schematic of FET structure, and (b) a typical

I_{sd}-V_g curve, turned on by negative gate voltage, and turned off by positive gate voltage.

Under the typical experimental condition, a p-type CNT-FET is constructed. The most common measurements are current versus voltage (IV) as a function of different back gate voltages. Sweep IV at step gate (Figure 2.11a) gives the conductivity as well as the band gap changing by the back gate. The I_{sd}-V_g curve (figure 2.11b) is similar to that of a MOSFET ; it turns on at negative gate voltage, and turns off at positive gate voltage [24].

2.4 Calculation of carbon nanotube electrical elements

The capacitance per unit length C_t of the SWCNT is given by:

$$\frac{1}{C_t} = \frac{1}{C_q} + \frac{1}{C_g} \tag{2.16}$$

C_q is quantum capacitance. C_g is the gate capacitance. The classical C_g is the result of electrical field between conductors, depends on the geometry and dielectric materials. The quantum part C_q is the result of the constrains created by the discrete electronic states and related to the DOS and independent of electrostatics. For a back gate configuration, C_g $<<C_q$, so $C_t \sim C_g$.

$C_t=C_g=2\pi\varepsilon\varepsilon_0/\mathrm{Cosh}^{-1}(h/r)= 2\pi\varepsilon\varepsilon_0/\ln(2h/r)$. For a liquid gate, $C_g>>C_q$, $C_t \sim C_q$.[5, 24] Assuming diffusive transport, the conductance, G, of a semiconducting SWCNT can be approximated by [24],

$$G = en\mu . \tag{2.17}$$

Another way of looking at the number of available carriers is using equation Q=CV. Here we take the charge en as CΔV. The relevant capacitance is the capacitance per unit length, which determines Fermi level of CNT. The ΔV is the voltage difference between the gate voltage V_g and the threshold voltage V_0, we have $\Delta V = V_0 - V_g$. This gives the equation,

$$G = \frac{C_t \left| V_0 - V_g \right|}{L} \mu \quad . \tag{2.18}$$

We can deduce mobility μ from this equation by assuming that μ is constant. Mobilites in the range of 1000-4000 $cm^2 / V \cdot s$ are routinely obtained.

Transconductance can be calculated by,

$$g_m = (\partial Id / \partial Vg)\Big|_{Vd} = \frac{CtV_d \mu}{L} \quad . \tag{2.19}$$

The slope of $I_d - V_g$ reflects the capacitance/mobility change. The transconductance is often used to calibrate the sensitivity of FET for chemical and bio-sensor.

The number of charges trapped per unit length is:

$$Q = ne = C_g \left| V_0 - V_g \right| \sim C_g V_0 \quad . \tag{2.20}$$

The change of charge $\Delta Q = C_g \Delta V_0$ supposing C_g will not change. The shift of V_0 represents the change of charge.

Chapter 3

DEVICE FABRICATION AND EXPERIMENTAL SETUPS

This chapter describes key steps in the fabrication of the nanostructure used in thesis. In this thesis, several experiments use a similar design, with small changes for specific purposes. In the DNA translocation experiment (Chapter 4), we use CNT as a nanofludic channel, in which one SWCNT spans a barrier between two fluid reservoirs, enabling direct electrical measurement of ion and small ssDNA transport through the tube [1]. In the study of wetting and filling effect in CNT-FET (Chapter 5 and 6), we use a similar design to DNA translocation experiment, but embedded a field-effect transistor (FET) into the CNT nanofludic device, in which the interior of a CNT-FET acts as a nanofluidic channel that connects two fluid reservoirs, permitting measurement of the electronic properties of the SWCNT as it is wetted by an analyte [25]. The electrical measurement for DNA translocation and CNT-FET wetting used two different systems. DNA translocation experiments measured ionic current as a function of time using a sensitive current/voltage meter (Axon, Molecular Devices, Inc., CA); and the CNT-FET wetting experiment measured source-drain current versus gate. The measurements were taken place in a probe station use with a 2 channels low-noise Keithley current meter.

3.1 Growth of carbon nanotube

3.1.1 Long single-wall carbon nanotubes (SWCNTs) growth by chemical vapor deposition (CVD)

We used Co nanoparticles as catalysts and ethanol as the carbon source. This method shows great performance in SWCNT growth with control over orientation, length, and diameter[26]. The growth mechanism of ethanol CVD for SWCNTs involves the dissociation of ethanol molecules catalyzed by the transition metal, and dissolution and saturation of carbon atoms in the metal nanoparticles[26, 27]. The precipitation of carbon from the saturated metal particle leads to the formation of tubular carbon solids with sp^2 structure. Tubule formation is favored over other forms of carbon such as graphitic sheet with open edges. This is because a tube contains no dangling bonds and therefore is lower in energy[7]. At high temperature, carbon has finite solubility in this metal, which leads to the formation of metal-carbon solution and therefore forms the SWCNTs once the metal is saturated. The SWCNTs grown in this way can be 1 ~ 2nm in diameter. The longest SWCNT we have grown was 1.05 cm.

3.1.2 Experiment setup

Figure 3.1 shows the experiment set up. Hydrogen (H_2) and Argon (Ar) were used for the growth of SWCNTs by CVD. The two gases first pass through drying units (DRIERITE) and filters (Swagelok), which remove the water vapor and other impurities. A mass-flow controller (MKS type 1179) was used to control the flow and pressure of the two gases in this growth system. After passing the mass-flow controller, there are two paths for gas flow, as shown in Figure 3.1a top view. The lower part is for warming up the tube furnaces and removing the

polymer on silicon substrate; the upper part is used to deliver the ethanol,[26] kept in an ice/water bath (0 ˚C), into the tube furnace (Lindberg/Blue, mini-mite 1100C Tube furnace, single zone), where the SWCNT growth take place. The tube furnace is schematically shown in Figure 3.1b.

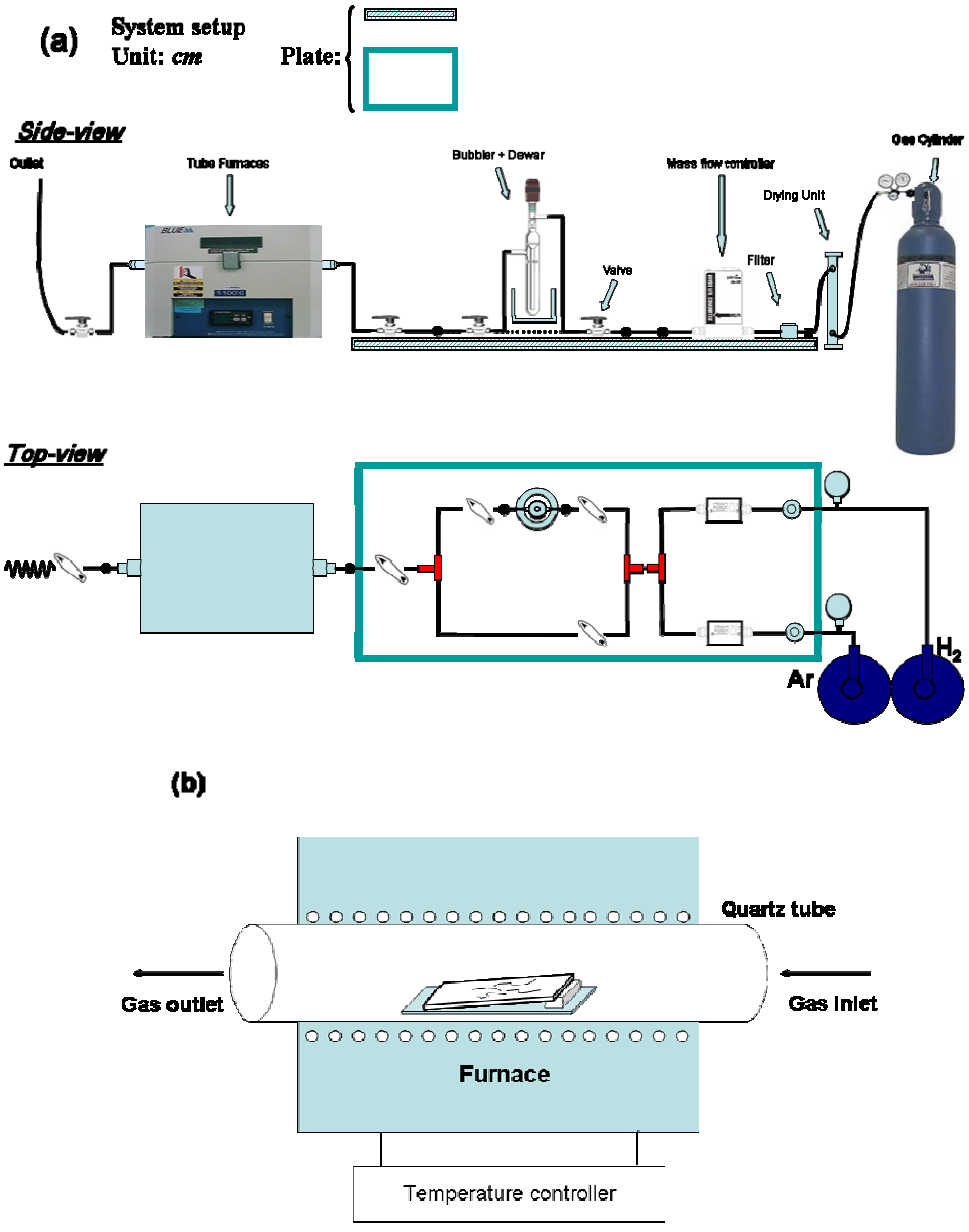

Figure 3.1. (a) Experiment setup: side- view and top-view; (b) schematic diagram of the ethanol chemical vapor deposition (CVD) in the tube furnace (one

inch diameter quartz tube, 15 inch heating zone), where the CVD for growing SWCNTs is performed over a Co catalyst.

3.1.3 CNT Growth procedure

Catalyst preparation: We used the block copolymer method[28] to synthesize transition metal Co nanoparticles with uniform size and distance between the nanoparticles, which can offer promise for the diameter- and position-controlled growth of carbon nanotubes. The polymer is Poly (styrene-b-4-vinyl pyridine) (PS-P4VP) (Mn-PS-b-4VP: 10400-b-19200; PDI: 1.27), received from Polymer Source, Inc. The transition metal Co is from Cobalt (II) acetate $(CH_3CO_2)_2Co$ (Sigma-Aldrich Inc.). 0.05 g of PS-P4VP di-block copolymer was added into 12.5 ml toluene and stirred at 70°C for 4–5 hours. Subsequently, 1.1 mg of $(CH_3CO_2)_2Co$ powder was added to the block copolymer solution and stirred for 24 hours at 30°C. With this process, the Co nanoparticles will be homodispersed in the polymer. The size of metal Co particle, of the order of nanometers, will determine diameters of newly grown SWCNTs. Therefore to synthesize SWCNTs of comparable diameters, a uniform nano-structure of the Co catalyst has to be prepared very carefully. The PS-P4VP block copolymer forms micelles in toluene which are capable of self-organizing into ordered structures on substrates. Interactions between the transition metal Co ions and the pyridine group were utilized to sequester metal ions in the spherical domains (nanoreactors) to form monodisperse metal nanoclusters. Coordinated covalent bonds are formed as a result of the interaction between the lone pair of electrons associated with the nitrogen atom in the pyridine group and Co with partially filled 3d orbital.

Catalyst Oxidation: A silicon substrate (15mm × 30mm) with 1.0 μm thick SiO_2 was cleaned by piranha solution (concentrated sulfuric acid to 30% hydrogen peroxide solution at 3:1 ratio) *(caution: Piranha solution should be handled with extreme caution as it can be explosive upon contact with organic materials)* and then rinsed by de-ionized water. After dipping the edge of silicon substrate into polymer Co catalyst solution, the substrate was put on a quartz sample boat (15mm × 50mm) with the catalyst side facing the gas flow entrance and sent into the center of the 1 inch diameter quartz tube, shown in Figure 3.1b. The substrate with a metal-salt-polymer strip was heated in the air at 750°C for about 15 min in order to oxidize the catalyst and to remove the polymer from the micelles. Please also note that other methods may be used to introduce catalyst onto the substrate such as PDMS stamping. The importance thing is to control the amount of catalyst. Instead of using a tube oven, oxygen plasma can also be used for catalyst oxidation.

Catalyst reduction: The substrate was taken out of the tube oven after oxidation. It is suggested that the CNT growth can be improved if the substrate is tilted by slightly increasing the height of the catalyst side of the substrate. As shown in Figure 3.1b, the substrate is tilted about 5 degree by inserting a small piece of silicon block under the substrate at the catalyst side. The substrate is reloaded into the tube furnace. With Ar flow at 300 sccm (standard cubic centimeter) and H_2 at 110 sccm, the temperature of the furnace is ramped up to pre-set 900°C with ramp rate of 18°C /min. The reduction time is about 15 minutes. The temperature distribution in the tube furnace is not uniform. It is important to keep the catalyst

edge aligned with the center of the tube furnace each time when loading sample to avoid yield fluctuation.

CNT growth: The furnace is kept at 900°C and the hydrogen gas flow rate reduced (H_2 at ~30 sccm and Ar at ~300 sccm). The nanotube growth is started by switching valves to allow ethanol vapor to get into the furnace (close lower path and open upper path in Figure 3.1a top view). The growth is normally carried out for 1.5 hour.

Finish growth: After growth, the hydrogen is closed. The quartz tube is allowed to cool down in Ar flow (~300sccm). The substrate is removed and cleaned with Acetone, IPA and DI water. The substrate is kept in water to avoid contamination prior to SEM imaging.

3.2 CNT nanofludic device fabrication

Cobalt catalyst particles were synthesized using the block copolymer method[29] and were introduced by a brush (or PDMS stamp) to the edge of a silicon chip that has 300 nm or 1000nm of thermally grown SiO_2 on the surface. Individual SWCNTs of low defect density (Figure 3.2) were grown by a chemical vapor deposition (CVD) process from cobalt catalyst particles using ethanol as the carbon source.[30] After growth, the chip was investigated by SEM and the chip with long SWCNTs was rinsed with organic solvent (IPA or acetone) and immediately covered with a thin PMMA layer (no baking) to keep for future use. The diameter of the SWCNTs was determined to be around 1.5-2nm. A

representative distribution is shown in Figure 3.2c. Other properties such as diameter and chirality can be determined by Raman spectra [31].

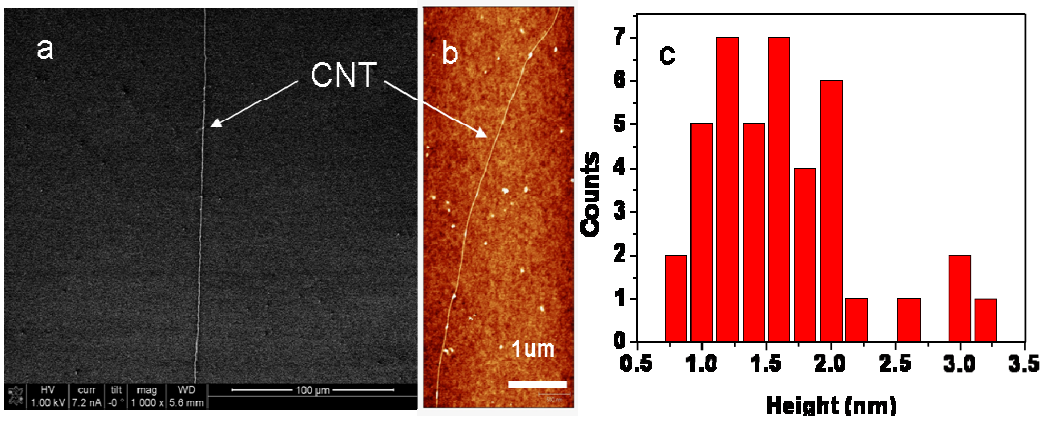

Figure 3.2 SEM (a) and AFM (b) images of SWCNTs as produced. c) Distribution of CNT diameter as determined by the AFM height measurement

3.2.1 Position of SWCNT with alignment marker

After CNT was grown on the silicon chip, the position of CNT must be found. We grew a layer of gold alignment markers on the chip. The gold alignment marker is divided into several blocks with coordinates marked with letters and numbers, see Figure 3.3. The position of CNT can be specified with the coordinate letter and number. The gold alignment marker was fabricated by optical lithography process or Electron beam Lithography (EBL) process. Optical lithography is fast and can be mass produced, but the resolution is low, around 2um. Electron beam lithography is slow but has much higher resolution, ~10nm [32].

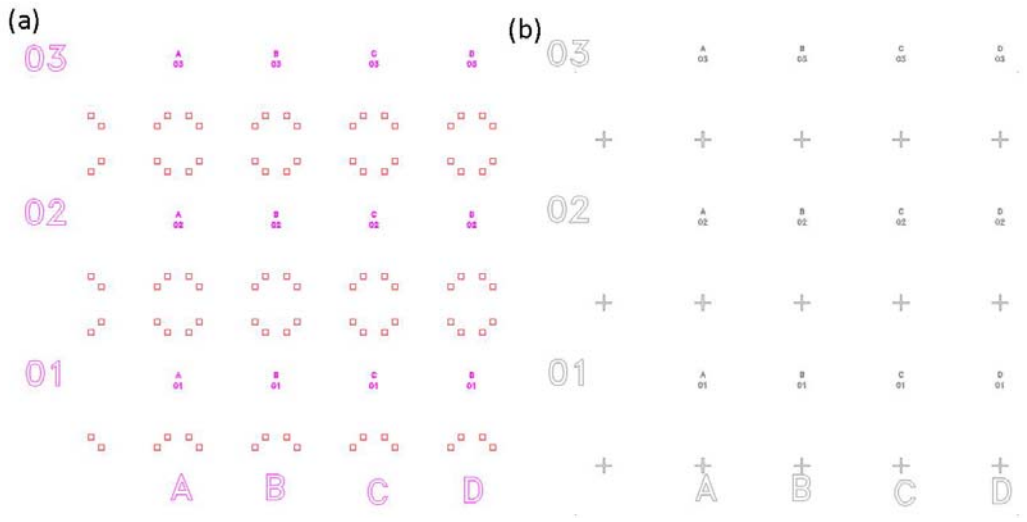

Figure 3.3 Gold alignment marker design for (a) photolithograph (b) EBL

For the optical lithography process, we used the cleanroom in the Center for Solid State Electronics Research (CSSER) in Arizona State University. An EVG620 aligner is used for exposure. First, we spin-coated the chip with photo resist AZ 5214 IR at 4000 rpm for 30 sec, which gave an expected thickness of 1.2~1.4um. (Image reversal was used here to facilitate liftoff [33]) Then the chip is soft baked at 100℃ for 90 sec. Then the EVG620 aligner was used to expose at dose 35mJ/cm^2 with the mask shown in figure 3.3. After exposure, the wafer was post-baked on hot plate 115℃ for 120sec. After post bake, the wafer was taken back to EVG620 aligner for flood exposure at dose 110mJ/cm^2. No mask was needed at this step. For the wafer development, the chip was immersed in AZ 300 MIF to develop for 1min. The patterns were checked under optical microscope. An adhesion promoter, HMDS, was not used here so that we can remove the photoresist.

The image reversal process reverses the action of positive photoresist so that negative images can be formed with the same resolution. After development, the photoresist in pattern area is gone, ready for metal deposition, see Figure 3.4b.

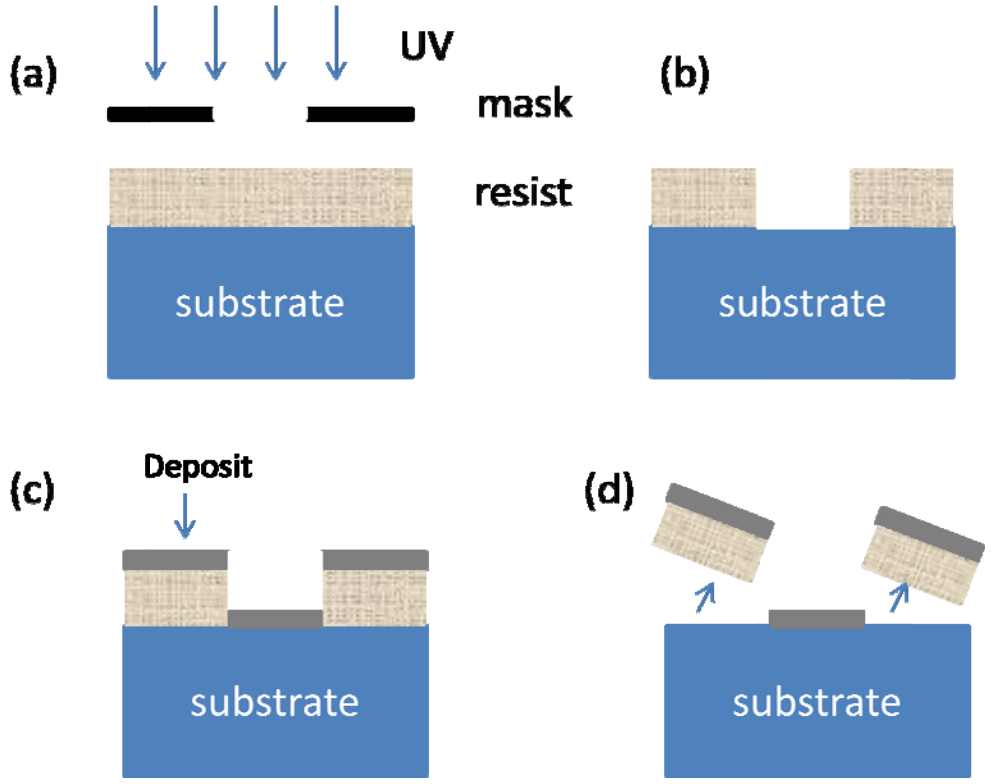

Figure 3.4 Photolithograph process (a) exposure (b) develop (c) metal deposition (d) liftoff

We use an evaporator (Edward 2) for metal deposition (Figure 3.4c), first adding liquid nitrogen; the vacuum is pumped below $3x10^{-6}$ torr. A large current was used to melt the metal, then 5nm chrome is deposited at current of 3.8~4.4amp and rate of 0.1nm/s. Then 30nm gold was deposited at current of 3.4amp and rate of 0.2nm/s. Chrome was used here to increase attachment between silicon dioxide and gold marker [32].

The photoresist was easy to liftoff by dipping the chip in acetone. The acetone can be heated up to 70°C and the solvent can be stirred to speed up the lift-off process. The metal pattern should appear after lift-off, see Figure 3.4d.

The Electron Beam Lithography (EBL) process procedure is very similar to photolithography with some operation differences. One big difference is that photolithography needs pre-designed mask, while EBL does not need a mask and only needs the pattern to be drawn on the computer, leaving much freedom for modification. We use the EBL process because the photolithography often leaves residues on the substrate which are hard to be cleaned. However, the EBL is much slower than photolithography.

We used the JEOL JBX-6000FS EBL system. Before proceeding, the alignment marker pattern was drawn on autoCAD, and saved as dxf 2000. We used linkCAD to convert the file to GDSII format. The GDSII files were sent to the EBL computer. Units used were micrometers. On the EBL computer, GDSII was converted to j51 file, then the .pchk file was used to check patterns, and finally the .ptd and .ptn files were created.

For the sample preparation we used E-beam resist PMMA A 8 or ZEP. The process is the same for these two kinds of resist. Chips were spin coated for 30sec at 3000rpm, and then pre-baked on the hotplate at 170°C for 15min.

After the sample was loaded in the chamber, before further operation, the parameters of the lithography were written into .jdf and .sdf file, including the dose and the position of pattern we want to expose. The mgn file for was created

for the exposure. The sample jdf and sdf files are in the Appendix A. Exposure and development of E-beam resist are discussed in Sections 3.2.3 and 3.2.4.

Metal deposition is the same as photolithography. For PMMA lift off, the chip is immersed in dichloromethane (CH_2Cl_2) for 10 to 20min, flushed with acetone. For ZEP lift off, immersed in ZDMAC (remover made by Zeon Chemicals L. P.) with small amount acetone heated to 80°C for half an hour (maybe even longer), flushed with acetone.

After liftoff, the alignment marker was complete. The alignment marker was designed by several blocks array in row and columns. The row was marked by number and the column is marked by letters. The location of particular block was fixed if we find out the number and letters. The block corners were placed on squares, used for more precise positions. Figure 3.5 shows the alignment marker after fabrication.

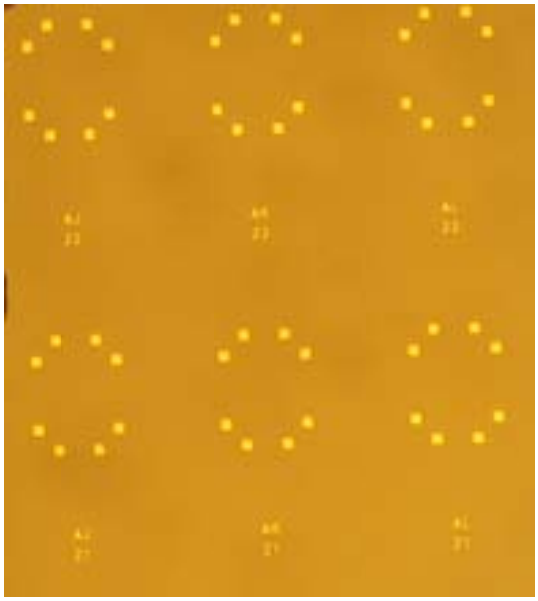

Figure 3.5 the gold alignment marker done by photolithograph. The row is marked by number and the column is marked by letters.

3.2.2 Determine the location of CNT by SEM

After gold alignment marker is done, the CNT is located by SEM imaging. Using FESEM (CSSER) or FIB (CSSS), with the measurement condition of voltage 1kV, current 0.46nA (FIB). The catalyst area was found first, and then the sample was moved a little bit below the catalyst area, and swept from the left end to the right end. The whole rectangular grid is imaged with CNT in it. An example was shown in Figure 3.6.

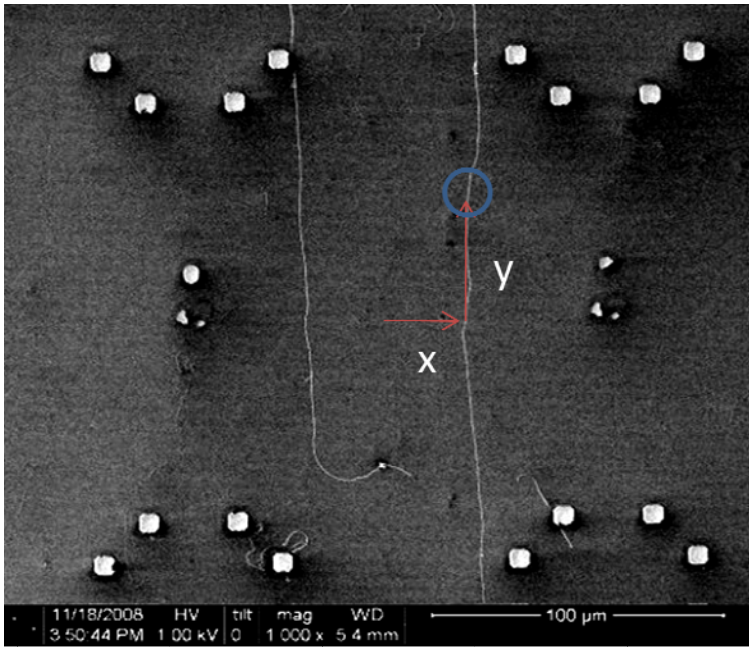

Figure 3.6 SEM image of gold alignment markers. The circle is where we want to put reservoirs, x and y are the coordinate relative to the center

After the SEM was taken, next step was to find CNT coordinates in this grid using the SEM image, See Figure 3.5. Graphics software ImageJ was used; first the center point of the rectangular grid was set. Then we found the coordinate position (x, y) of the position where we want to put reservoirs relative to the center. Then the row and column number of this rectangular grid was recorded.

The EBL exposing pattern file was updated using the coordinates of the CNT. This file was written as jdf file; please see Appendix A for sample files. In the file, the reservoir type was chosen from pre-defined patterns. Also some grid positions were chosen for control devices (No CNT). Six to eight reservoirs were opened on one chip at one time. A record was made for chip and positions where the reservoirs are opened.

After SEM imaging, the chip was cleaned for next step use. This was very critical for successful CNT opening for subsequent measurements. For the cleaning, the chip was rinsed with organic solvent (acetone and IPA). It was blown to dry in nitrogen gas flow. The chip was cleaned by heating in a furnace at 400°C in Ar and H_2 flow for at least one hour. The chip was spin-coated with PMMA A8 resist immediately.

3.2.3 Making reservoirs by EBL

Both PMMA and ZEP can be used for reservoir patterning. For the same condition, ZEP gives thinner layer and need less dose for exposure.

For PMMA, we chose PMMA A 8, the chip was spin-coated at 3000rpm for 30sec with the thickness of 900nm. The chip was prebaked on hotplate at 170°C for 15min, or oven at 160°C for more than 4 hours. The Exposure dose was chosen 540uC/cm^2. (using the command "EOS 7,'U50_100pA' SHOT A,4 RESIST 540,4".) The expose time was around 30 to 40min.

For ZEP, we use ZEP520A. ZEP was stored in the refrigerator at 4°C, and taken out to spin immediately. The chip was spin coated at 3000rpm for 30sec, with the thickness of 400nm. Then it was pre-baked on hotplate at 170°C for 15min. The

exposure dose is 100uC/cm2. (using the command “EOS 7,'U50_100pA' SHOT A, 4 RESIST 100, 4”.) The expose time was about 5 to 10min.

Before loading the sample, gold marker was found with an optical microscope; two crosses on the gold marker are chosen for alignment. For alignment, cross coordinates were found from the autoCAD file. Then the whole chip was divided into several rows and columns for fine alignment. The up-left corner of the whole marker was set as the beginning of row and column number. The CNT coordinates were determined by the row, column, and the shift relative to the grid center (x,y from SEM images). This information was put in to jdf files, while we include in the Appendix A.

3.2.4 Development of the EBL pattern.

This step was performed right before the measurement. The optical image of the device after development is shown in Figure 3.7.

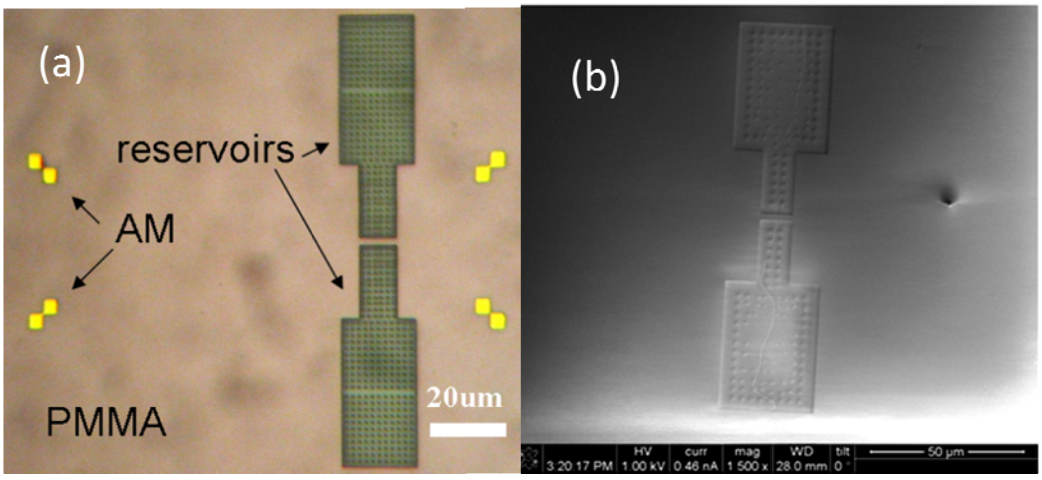

Figure 3.7 (a) Optical image of the CNT nanofluidic device after development. ‘AM’ means alignment marker. (b) SEM image of reservoirs after development. The CNT can be seen to pass the barrier between the two reservoirs.

For PMMA, the chip was immersed in developer (MIBK:IPA=1:3) for 90sec (or longer if needed) and stopped in IPA for 30sec, then blown dry with nitrogen.

A high contrast developer was also used by mixing solutions as the ratio MIBK':CS:MEK=11:10:1. (MIBK'=MIBK:IPA=1:3 used in ERC138) This recipe is patented by CSSER in Arizona State University. The regular developer is a simpler method (MIBK:IPA=1:3 use in lab).

For ZEP, the chip was immersed in ZED-N50 (room temperature) for 1min and stopped in MIBK (room temp) for 30sec, then blown dry with nitrogen. Post bake was optional; the chip was put on hotplate 120°C for 2min.

After resist development, the chip will be treated by oxygen plasma (0.6 Torr, 7.3W, 20sec) around 30sec to cut and open the ends of CNT for nanofluidic measurement.

3.2.5 MWCNT device fabrication

The MWCNT was purchased from Sigma-Aldrich Inc, with outer diameter 10-30nm and inner diameter 5-10nm. The nanotube was dispersed inside PMMA A5 solutions by mild stirring over 24 hours. The concentration was around 0.1mg/ml. After the suspension was well dispersed, the nanotube/PMMA mixture was applied on substrate with a small brush. Then the substrate was baked at 180℃ for 10min and transferred into the tube furnace immediately for PMMA removal. PMMA was removed by heating the substrate to 400℃ under 300 sccm Ar flow for at least 1 hour. The SEM and AFM image of the MWCNT chip is shown in Figure 3.7.

The rest of the fabrication procedure was the same as the SWCNT. The MWCNT was more difficult to be opened by oxygen plasma treatment.

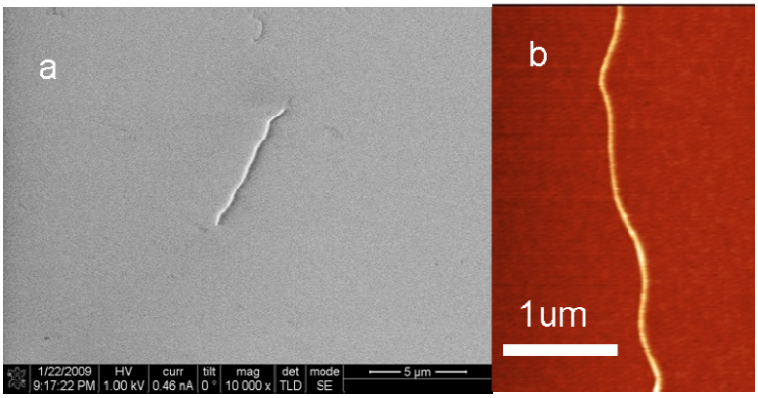

Figure 3.8 SEM (a) and AFM (b) images of well-dispersed MWCNT on silicon oxide substrate.

3.3 Fabrication of the PDMS microfluidic delivery device

The PDMS microfluidic delivery device, which can be easily integrated with the carbon nanotubes based nanofluidic device, is a significant part for the measurement of the ion current[34]. The chemical structure of PDMS, with chemical formula is $(CH_3)_3SiO[Si(CH_3)_2O]_nSi(CH_3)_3$, is shown in Figure 3.9.

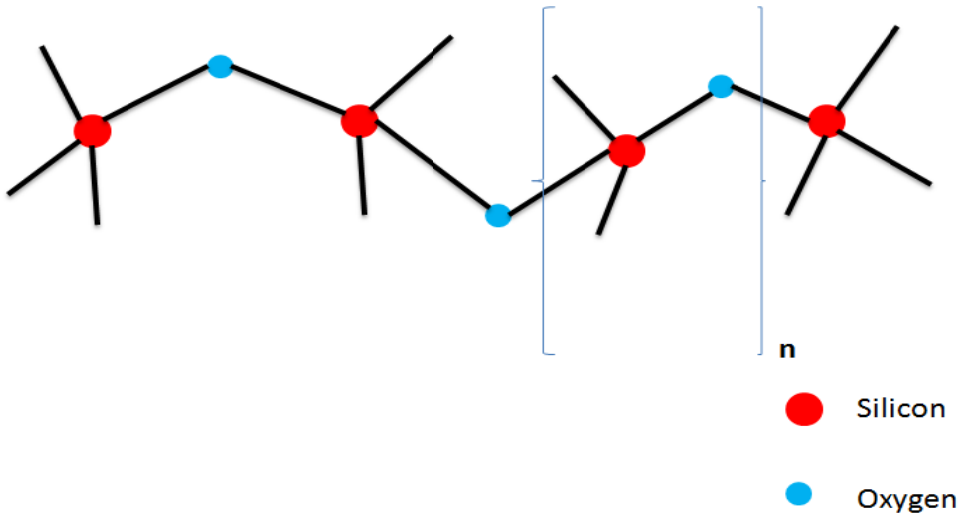

Figure 3.9 The schematic diagram of the PDMS structure.

The PDMS delivery device was prepared before measurement. It connects the macrostructure with the CNT nanofludic structure.

First, the PDMS base was mixed (Sylgard 184 Silicone Elastomer kit) with its curing agent at a ratio of 10.75:1 and stirred about 2 minutes in order to obtain the uniform solution. The mixture was degassed at low pressures (35 Torr) for 30 minutes or more until all bubbles in the solution are removed. Then the mixture was poured into two petri dishes which contain the top pattern and bottom pattern in Figure 3.10. The two PDMS stamps which form the delivery device were placed for 48 hours at the room temperature to become hard.

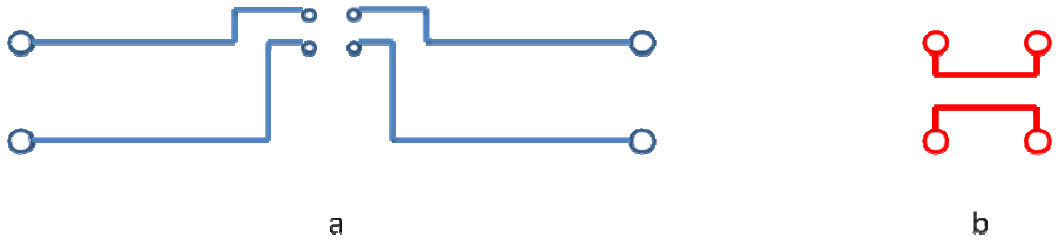

Figure 3.10 a) The pattern of the top PDMS stamp. b) The Pattern of the bottom PDMS stamp

We use the stainless steel tubes to make the holes of the PDMS stamps in order to make ion current transport through the device. The two layers were placed in oxygen plasma cleaner to be treated at high level (550~600 mTorr, 19.8 W) for 40 sec. We aligned the two layers under optical microscope as shown in Figure 3.11.

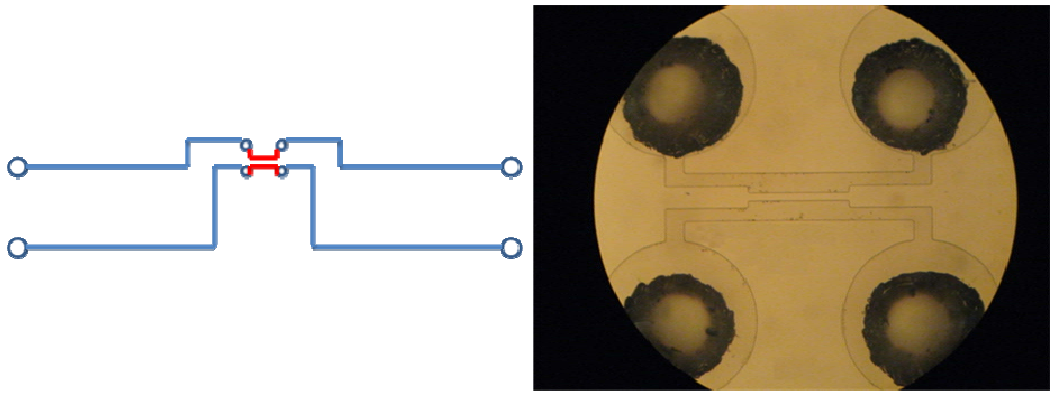

a b

Figure 3.11 a) Alignment of two PDMS layers. b) Photo after the alignment.

The PDMS device was heated for 60 sec at 70 ^{o}C to make sure the two layers stick together. Stainless steel tubes were inserted into the top PDMS stamp, and silicone tubes are used to connect the syringe. See Figure 3.12 for the PDMS microfluidic delivery device.

Figure 3.12 PDMS microfluidic delivery device.

We preformed leakage test to make sure that the PDMS device was good for the ion current transport experiment. We first filled the PDMS device channel with 2 mol/L potassium chloride (KCL). Then we applied a bias 500 mV between two channels and measured the leakage current, making sure it is less than 0.01 nA. It was concluded that the PDMS microfluidic delivery device is excellent and well sealed.

After confirming the PDMS microfluidic delivery device was good, the final step was to combine the PDMS microfluidic delivery device with the CNT nanofludic device. Under a microscope, the PDMS device was covered on the CNT chip, aligning the micro-channel with the position of reservoirs. See Figure 3.13 for details. The PDMS and the PMMA surface are both hydrophobic, after PDMS is sealed with PMMA, the microfludic channels were built. Finally, the solution was induced by the syringe, lead by PDMS microfludic channel to the PMMA reservoir, and finally filling the CNT between the two reservoirs.

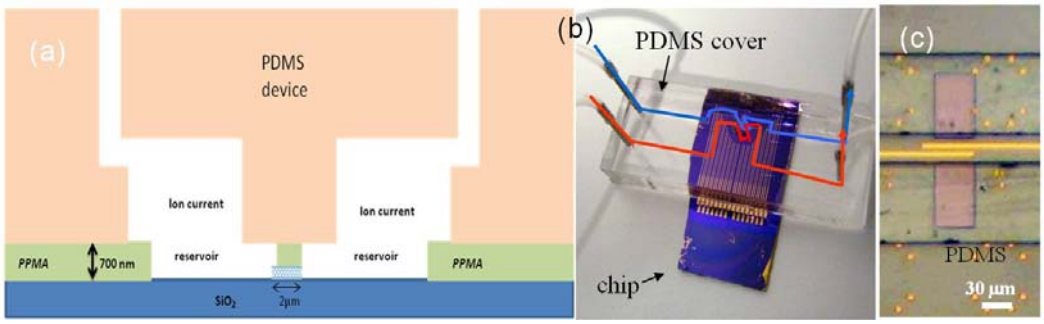

Figure 3.13 Cover PDMS device to the CNT nanofludic device (a,b) align the PDMS microfludic device with the PMMA chip surface. (c) Optical image under microscope show the channel of PDMS align with the reservoirs.

3.4 Building CNT-FET into a nanofludic device

In our CVD method growth of carbon nanotube, almost 90% of super long carbon nanotubes were semiconducting CNT[35]. This gives a broad application of using CNT as a semiconducting material in the transistors. In our experiments, the CNT-FET was embedded into nanofludic device by adding source-drain electrode in the barrier area between two reservoirs[23]. This step was added after SEM imaging, before making reservoirs. After locating CNT, the first electrodes were drawn by autoCAD, and then EBL and metal deposition was used to grow gold electrodes on the CNT. The CNT chip was soft baked before deposition to decrease the water molecules bonds on the surface of silicon dioxide, in order to decrease the hysteresis of the finally current versus gate-voltage curve[36]. We usually used electrodes of widths around 1 to 5um, and the distance between the source and drain electrodes was 1um to 20um. This scale was good for use of a CNT as a FET. If nanometer spatial control is needed, the electrodes should also be in nanometer scale. The EBL can give tens of nanometers electrode with good metal liftoff. Dekker *et al.* reported a silica nanopore method to fabricate gold electrode with nanometer precision[37].

The next step was to open reservoir at exactly the same position as the electrodes, leaving the electrodes between the two reservoirs, Figure 3.14a, fabricating the electrodes right between the two reservoirs.

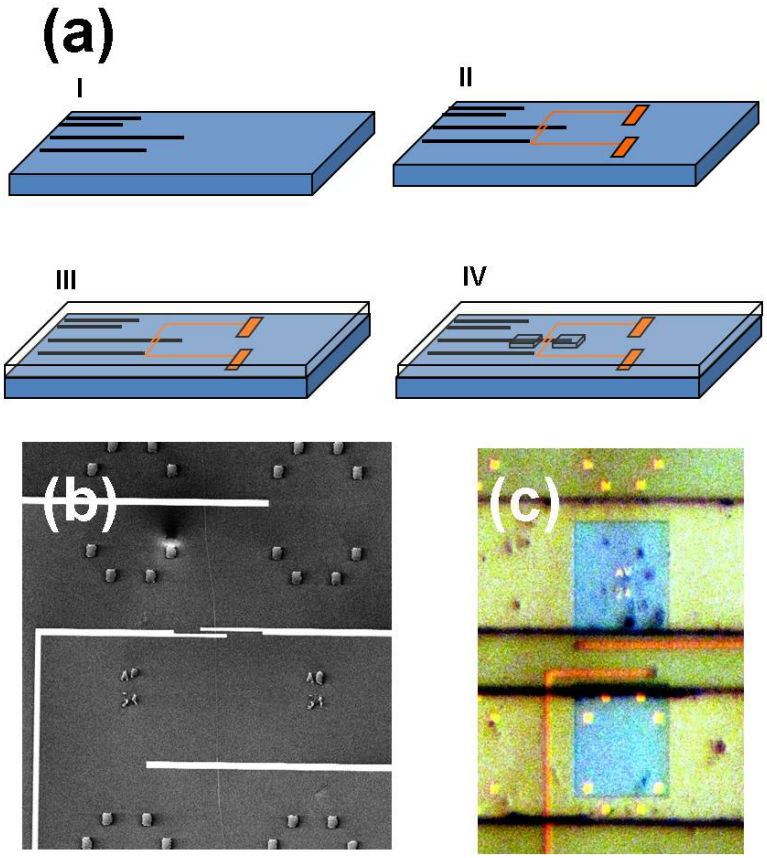

Figure 3.14 (a)Schematic of electrodes on nanotube nanofludic device fabrication (b) SEM image of carbon nanotube with gold electrode and alignment marks. (c) Optical image of developed patterned reservoirs covered by PDMS microfluidic channels.

The source-drain electrodes were connected with an electrical meter that could apply a bias and measure the current at the same time. Another gate electrode was added at the back of the chip, Figure 3.15, directly in contact with the silicon substrate. A voltage was added to the gate electrode relative to the source electrode. The gate electrode controls the potential of CNT, which will control the carriers along the tube. Compared with metal-oxide-semiconductor field-effect transistor (MOSFET), a bias was added to the source-drain electrode, while the gate electrode turned on and off the conducting channel between them. Thus the

carbon nanotube based field effect transistor (CNT-FET) was constructed. When the CNT was opened and added solution in the resevoirs, the interior of the CNT-FET acted as a nanofluidic channel that connects two fluid reservoirs, permitting measurement of the electronic properties of the SWCNT as it was wetted by an analyte. Measurement toke place in the Faraday cage with probe station. A Keithley SourceMeter 2636A, a Keithley low noise current meter 6514 and a function generator (DS 345, Stanford research system) were used and controlled by custom labview programs.

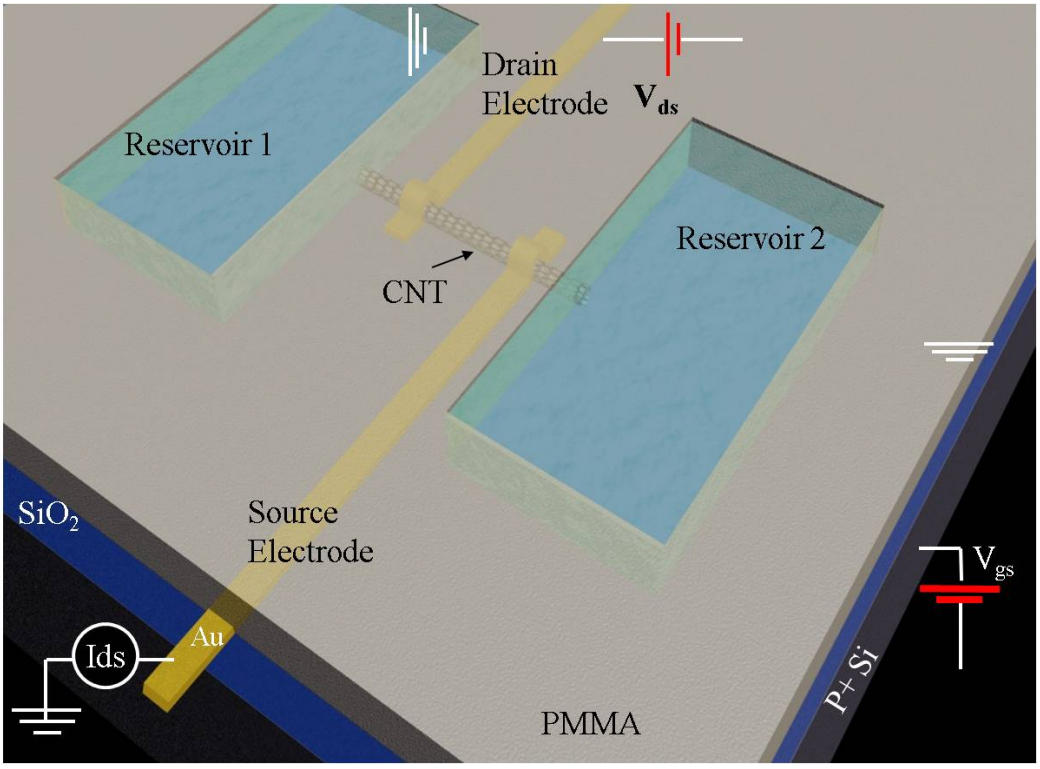

Figure 3.15 FET was built into CNT nanofludic device.

Chapter 4

TRANSOLCATION EVENTS THROUGH SINGLE-WALL CARBON NANOTUBES

We report the fabrication of devices in which one single-walled carbon nanotube (SWCNT) spans a barrier between two fluid reservoirs, enabling direct electrical measurement of ion and DNA transport through the tube. DNA translocation events are accompanied by giant current pulses, the origin of which remains obscure. Here, we show that introduction of a nucleotide alone, guanosine triphosphate into the input reservoir of a carbon nanotube nanofluidic also gives giant current pulses. Taken together with data on oligomer translocation, theses new results suggest that pulse width has a non-linear, power-law dependence on the number of nucleotides in a DNA molecule. Translocation of small single stranded DNA oligomers is marked by large transient increases in current through the tube and confirmed by a PCR analysis. Each current pulse contains about 10^7 e, an enormous amplification of the translocated charge. We have also measured the time for the onset of DNA translocation pulses after bias reversal, finding that the time for the onset of translocation is directly proportional to the period of bias reversal. Carbon nanotubes simplify the construction of nanopores, permit new types of electrical measurement and open new avenues for control of DNA translocation.

This chapter is based on the papers *"Translocation events in a single-walled carbon nanotube"* published in *Journal of Physics: Condensed Matter*, 2010 [2]

and *"Translocation of single-stranded DNA through single-walled carbon nanotubes"* published in *Science,* 2010 [1]. My contribution is construction the procedure of the carbon nanotube nanofluidic device fabrication and taking some of the carbon nanotube ionic current and translocation measurements.

4.1 Introduction

Nanopores are orifices of molecular diameter that connect two fluid reservoirs [38]. Kasianowicz *et al* first demonstrated translocation of DNA through a α-hemolysin (αHL) protein nanopore under external electrical field in 1996 [39]. Since then, there have been growing interests in applying nanopores as single molecule sensors and biophysics tools for studying biomolecules (DNA, RNA, protein, etc) [40, 41]. Single molecule DNA sequencing is one of the exciting applications proposed for nanopore [42]. The principle underlying nanopores is straightforward: nanopores can act as Coulter counters. When a single molecule carrying net charges is driven through the molecular size pore by an applied electric potential, it can physically block the pore during the translocation, which produces measurable and distinctive changes in ionic current.

There are mainly two types of nanopores: biological nanopores (e.g., αHL) and synthetic nanopores (also known as solid state nanopores). Recently, the carbon nanotube (CNT) emerged as a new type of synthetic nanopore. CNTs are remarkable materials [4, 6]. They are perfect seamless cylinders, formed by rolling up a graphene sheet (figure 4.1(a)) and capping each ends with half of a fullerene molecule. Depending on the number of layers, the CNT can be divided

into single-walled carbon nanotube (SWCNT), double-walled carbon nanotube (DWCNT), and multi-walled carbon nanotube (MWCNT). Carbon Nanotube based nanofluidic is a burgeoning field [43-46]. From a biological point of view, the CNT is an ideal model to help understand the biological membrane channels that work in aqueous environments with hydrophobic inner walls and nanometer channel sizes. From a fundamental research point of view, it's an exciting system to test classical theories of fluid flow at the nanoscale. From an application point of view, CNTs are perfect candidates for nanopores or nanochannels in nanofluidic devices. (1) They require no special nanofabrication to achieve a pore size of less than 5 nm. They have an atomically smooth surface and perfect uniformity over large distances. (2) For high quality CNTs, the chemistry and structures of the interior surface are well-defined, which simplifies theoretical simulations. (3) The excellent electrical properties of CNT provide new routes to electrical detection, trapping and manipulation of charged biomolecules and nanoparticles. (4) Well-defined sites are available for chemical functionalization at the ends of the tubes. Such modifications will be extremely useful for ion and molecule selection, gating or separation.

To utilize CNT as a nanopore or nanochannel, it's important to first understand the transport of water through CNT. It seems counter intuitive that water will enter and transport through hydrophobic and nanometer-sized CNT. However, Hummer et al. have used large scale molecular dynamics (MD) simulations to observe the spontaneous wetting and filling of a (6,6) CNT (1.34 nm in length) with water molecules [47]. The nanoscale confinement and the

interactions between water and CNT surface are found critical. The water molecules form ordered structures inside CNT, which makes confined water within the CNT more stable than bulk water. The lower free energy of confined water drives water molecules into the CNT automatically. Very fast water transport through CNT was predicted because of the friction-less motion. Following the pioneering work of water molecule transport, the translocations of more complicated molecules, such as long chain polymer molecules [48], DNA [49] and RNA [50] through CNT were simulated as well. Simulations revealed that DNA molecules enter CNT spontaneously with the aid of van der Waals and hydrophobic interaction forces [51] and the translocation events can be driven by electric field [49].

So far, experimental studies by nuclear magnetic resonance (NMR) [52], X-ray diffraction (XRD) [53], IR spectroscopy [54], transmission electron microscope (TEM) [55] and scanning electron microscope (SEM) [56] have confirmed that water could enter and form ordered structures in SWCNTs or MWCNTs. More direct transport measurements are finished by using CNT membrane, which consists of millions of carbon nanotubes in parallel [46]. Hinds' group has pioneered a MWCNT membrane fabrication strategy [57]. They cast a polystyrene polymer layer on a vertical aligned MWCNT forest to fill the gaps between MWCNTs and form an impenetrable membrane. Then both ends of the MWCNT were opened by oxygen plasma. Holt *et al* followed the work by replacing the polymer with low-stress silicon nitride and using smaller sized DWCNT [58]. Both groups found that the mobility of gas, water and ions can be

indeed greatly enhanced inside the tube. The transport of small redox and fluorescent molecules through CNTs has also been measured [59, 60]. The CNT membrane is relatively easy to fabricate and is perfect for applications such as molecular separation and sea water desalination [60, 61].

Inspired by these experiments and theories, we set out to fabricate *single* carbon nanotube based nanofluidic device. There are several reasons to pursue individual CNT based nanofluidic device. First, the CNTs are heterogeneous in physical properties. The single CNT approach allows us to carefully study the properties of individual CNT nanopores, facilitating development of a fundamental understanding of the mechanisms. Second, the single CNT approach provides great potential for detecting and controlling the translocation of water, ion and small organic/bio molecules through CNT. The excellent electrical properties of individual CNTs are readily utilized. We have shown that the semiconducting CNTs were permanently switched on after filling CNT with pure water [1]. The transition of CNT electrical properties during water filling and conduction will provide a valuable probe for studying CNT based nanofluidic phenomena. Crook's group did some preliminary experiments in the single CNT direction by fabricating devices containing only one carbon nanofiber (about 150 nm in diamter) in epoxy membrane [62]. Shashank et al also reported the fabrication and fluid flow measurements of devices based on individual carbon nanopipe (about 300 nm in diameter) [63]. We have successfully fabricated molecular size CNT (about 2 nm in diameter) based nanofluidic device with only one SWCNT bridging two fluid reservoirs. The translocation of short single-

stranded DNA through SWCNT (mainly metallic) was studied, as marked by unusual electrical signals and confirmed by polymerase chain reaction (PCR) [1]. Interestingly, the ionic current signatures during DNA translocation in SWCNT are quite different from those in silicon based nanopore/nanochannel [64-66]. The origin is not clear yet. One reason may stem from the unique geometrical and electrical property of CNT. In addition, experimental and theoretical studies have revealed the complicated interactions between DNA oligomers and the graphitic surface [67-71], which should also affect the translocation dynamics of DNA and hence the electrical signal structures in ionic current. It's still a challenging task to understand the DNA translocation events in CNT, which requires numerous experiments and simulations.

In this chapter, we will first briefly explain the device fabrication and ionic current measurement. High ionic current was measured in a fraction of the devices, and was attributed to the rapid electro-osmotic flow in the tube according to the multi-scale simulations. It appears that small molecules will enter the tube much more readily than long polymers, so we have studied the signals obtained from guanosine triphosphate (GTP) as a model of an N=1 molecule (or N=3 based on charges). We cannot use PCR to confirm translocation (cf. section 3), but the similarity in signals suggests that translocation of GTP does occur. We also present data for translocation of small single stranded DNA oligomers and on the onset time for DNA translocation signals as a function of the time for which bias was previously reversed.

4.2 Device fabrication and ionic current measurement

Device fabrication has described in detail in previous chapters [1]. In brief, well separated and high quality SWCNT was grown on silicon oxide surface by the chemical vapor deposition (CVD) method using ethanol as carbon source and Cobalt nanoparticles as catalyst [28]. The average outer diameter of SWCNT is about 1.6 nm as determined by atomic force microscope (AFM). After the growth, gold alignment marks were patterned on the substrate to register the location of the CNTs (figure 4.1(b)). Then the substrate was coated with a 800 nm thick poly (methyl methacrylate) (PMMA) layer and the reservoir patterns were generated by electron beam lithography (EBL). An optical image of the device is shown in figure 4.1(c). The SEM image of the barrier area (figure 4.1(d)) shows that only one CNT is buried under the 2 μm wide barrier and bridges the two reservoirs. Oxygen plasma was used to remove the exposed CNT in the reservoirs and open the ends. The intensity of oxygen plasma needs to be carefully controlled to avoid damaging the PMMA surface. Control devices without CNT are always fabricated in the same chip to monitor the leakage current.

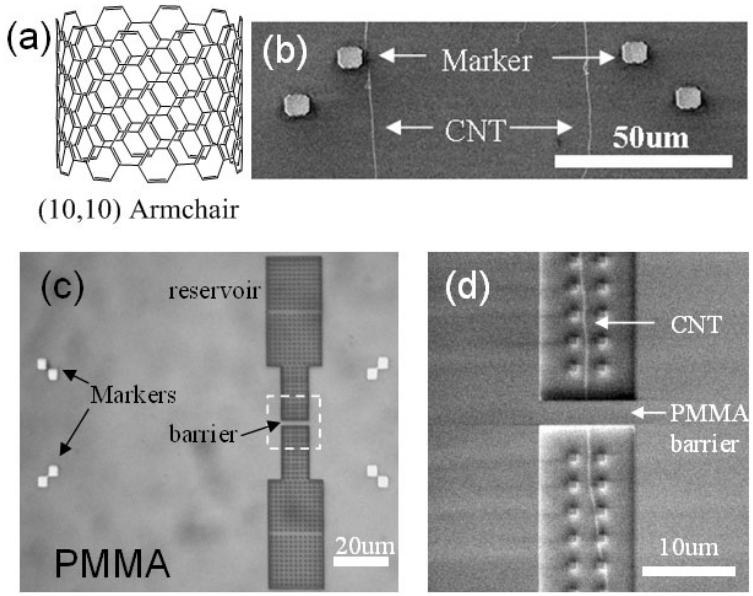

Figure 4.1. (a) The atomic structure of a (10, 10) armchair SWCNT (~1.4 nm in diameter). (b) SEM of SWCNTs on silicon oxide surface. The gold markers are fabricated after SWCNT growth and are used to locate the CNT. (c) Optical image of a fabricated device after EBL step. Gold alignment markers and reservoirs are clearly seen. The white dashed square labeled the barrier area. (d) SEM of the barrier area (~2 μm in width). One SWCNT passes the barrier and bridges two reservoirs. The SWCNT in the reservoirs will disappear after oxygen plasma.

As shown in figure 4.2 (a) and (b), a polydimethylsiloxane (PDMS) stamp with embedded microfluidic channels seals the top surface of the device. Buffered KCl solution (1mM PBS buffer, pH=7) is injected into both reservoirs and reaches the CNT openings. Silver/silver chloride electrodes (BASI MF-2078) are immersed in the salt solution. A voltage is applied between the two reservoirs and the ionic current is recorded (figure 4.2 (b)) using an Axopatch 200B (Molecular Devices, Inc., CA).

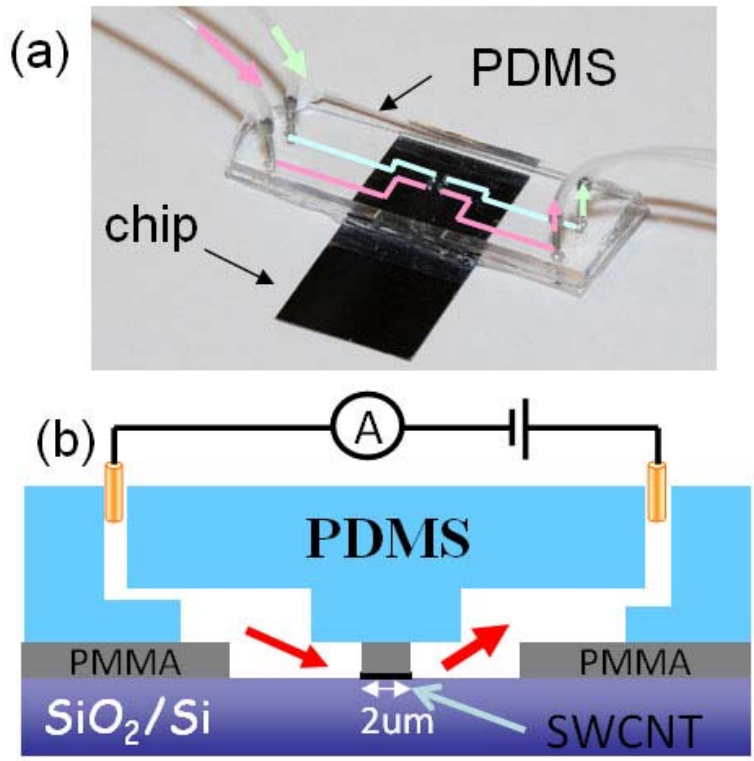

Figure 4.2. (a) Optical image of an assembled device with one pair of silicon tubes for flushing the input channel (green pathway) and a second set for flushing the output channel (pink pathway). (b) Schematics of the cross-section of the assembled device and the ionic current measurement setup.

Each device was accompanied by a control device lacking the bridging CNT to check the quality of the seal to the PDMS cover and the integrity of the PMMA barrier. The fluid reservoirs were filled with 1M KCl, and Ag/AgCl electrodes (BASI MF-2078) were used to measure the conductance across the reservoirs connected by the SWCNT. After measurements, chips were stripped of PMMA so that we could use AFM to measure the diameter of each CNT (Figure 3.2). The current-voltage characteristics are linear (Fig. 4.3A). The measured tube conductance is plotted vs. tube diameter in Figure 4.3B and it is consistent with the expected quadratic dependence (though significant uncertainties in the

diameters mean that we cannot rule out a linear dependence such as that observed in channels with one nanoscale dimension [72]). This correlation between conductance and measured diameter is strong evidence that ion transport is through the tubes and not via a leakage path.

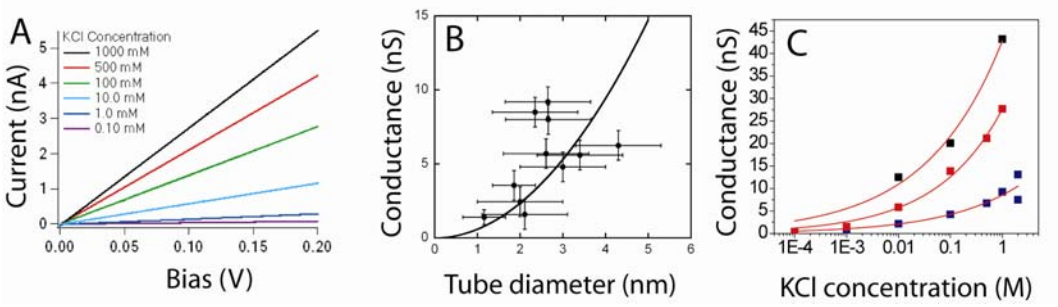

Figure 4.3 Ion transport through SWCNTS: A. Typical current-voltage curves as a function of salt are linear over the entire bias range used. B. Conductance vs. tube diameter. Tube diameters were determined by AFM after stripping off the PMMA resist and are subject to uncertainties caused by residual resist. Uncertainties in conductance represent day-to-day changes in a given tube. C. Conductance vs. log of salt concentration for three tubes. The lines are fits to $G \propto n^{\frac{1}{3}}$.

The large magnitude of the conductance is unexpected. The bulk expression for the ionic conductance of a tube is

$$G = \left(\mu_{K^+} + \mu_{Cl^-}\right) n_{KCl} e \pi D^2 / 4L \qquad (4.1)$$

where μ_{K^+} = 7.62 x 10^{-8} m^2/ V s, μ_{Cl^-} = 7.91 x 10^{-8} m^2/ V s, n_{KCl} is the KCl number concentration per m^3, e the electronic charge, D the tube diameter and L the tube length. With D = 2nm, L = 2μm and 1M salt, equation 4.1 leads to an estimate of $G \approx 0.02$ nS, about 250x lower than the conductances measured here. Possible explanations for this discrepancy are (a) enhanced ion mobility within the tube, (b) enhanced ion concentration in the tube, and (c) an important

influence of the end regions of the tubes in the reservoirs, not described in the simple formula above. Estimating the contributions of these factors to the enhanced conductance requires challenging multiscale simulations. We can, however, address a fourth option, that electrochemical currents owing to reduction and oxidation reactions at the end of the tube contribute a direct electronic component to the observed transport. It might appear that this possibility can be eliminated trivially because such a current would be absent in the subset of tubes that are semiconducting. However, direct measurement of the electronic properties of a semiconducting tube shows that it is turned "on" once its interior is wetted (see Chapter 5). A conducting tube suspended in a potential gradient in an electrolyte acts as a bipolar electrode [73] but enormous fields are required to drive electrochemical processes at the ends of a bipolar carbon nanotube electrode. [74] We made measurements with an electrode contacting the SWCNT directly, finding that electrochemical currents are negligible for the potentials used here.

We have measured the dependence of the current on KCl concentration, and data for three tubes are shown in Figure 4.3C (the horizontal axis is logarithmic). The solid lines are fits to the empirically determined relation $G \propto n^{\frac{1}{3}}$. This result disagrees with the linear dependence predicted by equation 4.1 and also has the opposite shape to the salt dependence observed in conventional nanopores, where surface charges contribute a nearly constant current at low concentrations. [75] A non-linear salt dependence could arise from charge accumulation/depletion at the ends of tubes, such as has been both

observed [76] and predicted [77] for electro-osmotic flow in charged nanochannels. While carbon nanotubes are, in principle, neutral, electro-osmotic flow could arise from the orientated water dipoles on the interior surface of the tube [78].

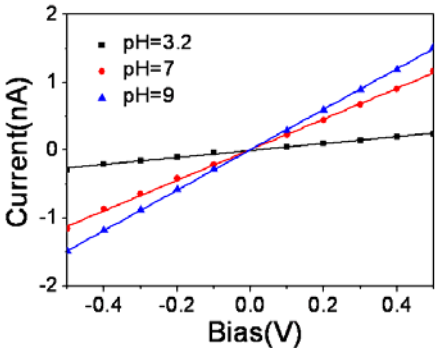

Figure 4.4: Typical current-voltage curves for a SWCNT as a function of the pH of 0.1M KCl with 1mM PBS. The measured conductance is 2.98 nS at pH9 (black squares), 2.25 nS at pH7 (red circles) and 0.51 nS at pH3.2 (blue triangles).

The pH of KCl solutions was adjusted by adding HCl or KOH and conductance measured for a number of tubes. A typical data set is shown in Figure 4.4. Reducing the pH of the KCl solution resulted in a substantial reduction of the current through the tube as shown in Figure 4.4. This presumably reflects protonation of the carboxylic acid residues at the end of the tube (pKa ≈ 4.5 [79]) showing that the charge distribution at the end of the tube plays a significant role in determining the current through the tube.

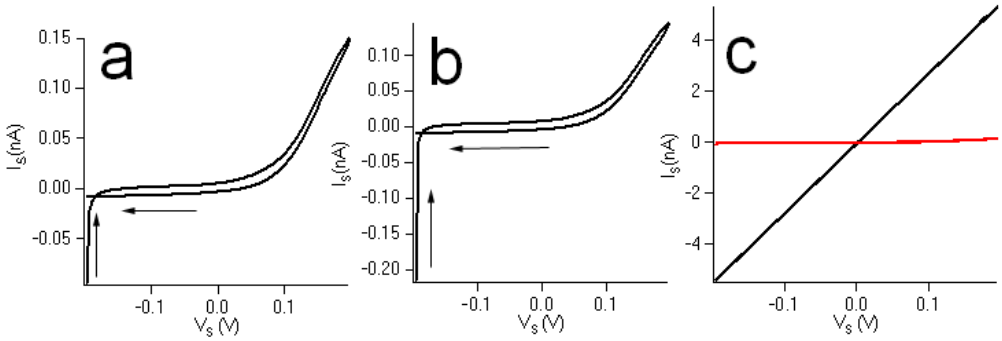

Figure 4.5: (a) Current in 1M KCl between the CNT and input reservoir as a function of bias applied to the Ag/AgCl electrode with the CNT grounded (arrows show sweep direction). (b) Current between the CNT and output reservoir. (c) Ionic current through the tube in 1M KCl plotted as a function of the potential difference applied to the two Ag/AgCl electrodes (black line) with the maximum electrochemical current (plotted as a function of the potential difference between the CNT and one Ag/AgCl electrode) shown on the same scale in red.

A device was fabricated with a 3 μm wide Au electrode (30 nm Au on 3 nm Cr) contacting an SWCNT under a 10 μm wide PMMA barrier. The electrochemical current was measured with the tube grounded and a bias sweep between 0 and ±0.2V with respect to the Ag/AgCl electrodes (which are at a resting potential of 0.22V vs. NHE in 1M KCl). If the potential drop across the floating SWCNT is symmetrical and all concentrated at the ends of the tube, this would correspond to a total applied potential difference of 0.8V, much higher than any of the biases used in this work (even more so if there is any significant potential drop across the tube itself). The results are summarized in Figure 4.5. Electrochemical current through the grounded tube is shown for current into the input reservoir in (a), and into the output reservoir in (b). For the CNT biased > -0.1V with respect to the Ag/AgCl electrode, a reduction current is observed, and the linear rise in

current suggests that it is diffusion limited. The Au-Cr contact will generate a Schottky barrier [80] but the symmetry of the curves suggests that this is not a significant effect. The currents observed here are higher than those reported for a CNT electrode without exposed ends, [81] suggesting that the electrode kinetics are enhanced at the ends of the tube.

These currents represent an upper limit to the electrochemical current because the potential drops in the bipolar configuration will be much smaller. Figure 4.5c shows a plot of the ionic current through the tube as a function of the potential applied between the two Ag/AgCl electrodes plotted together with the electrochemical current plotted as a function of the potential difference between the tube and one Ag/AgCl electrode. This shows that the maximum possible contribution of electrochemical current is minimal. The CNT remains stable after repeated electrochemical cycling as show by SEM examination of the CNT after stripping the PMMA.

We found [1] an enormous range of ion currents through these devices, apparently uncorrelated with SWCNT diameter. We also made field effect transistors (FETs) out of the tubes used for translocation and measured their electronic properties. On doing this, we found that the ion transport fell into two categories. The low current group (where currents correlated well with classical models) was mainly made up by the *semiconducting* tubes. The high current group was mainly composed by the *metallic tubes*. Theoretical multiscale modeling suggests that electro-osmosis dominates over electrophoresis in the metallic tubes that show

large ionic conductivity. We focus on devices made with these tubes in what follows.

4.3. GTP Translocation

Short ssDNA oligomers were chosen for the CNT translocation experiments. Quantitative PCR (Q-PCR) was used to verify DNA translocation. PCR is a fascinating molecular biology technique that a few or even single copies of DNA can be quickly and exponentially amplified to millions of copies. Therefore PCR is an ideal tool to detect trace amount of DNA with known sequence. However, the minimum length of DNA that can be amplified is about 20 nt. We have measured the translocation of 60nt, 120nt and 180nt long oligomers. In all the experiments, large transient increases ("spikes") in ionic current were observed. Those spikes signal the molecular translocation events, as confirmed by Q-PCR for the 60 and 120 nt oligomers. In general, the shorter oligomers show shorter spike width, but these widths are large compared to the translocation times observed with conventional nanopores [82]. This raises the question of whether a *single* nucleoside-triphosphate can generate a measureable signal.

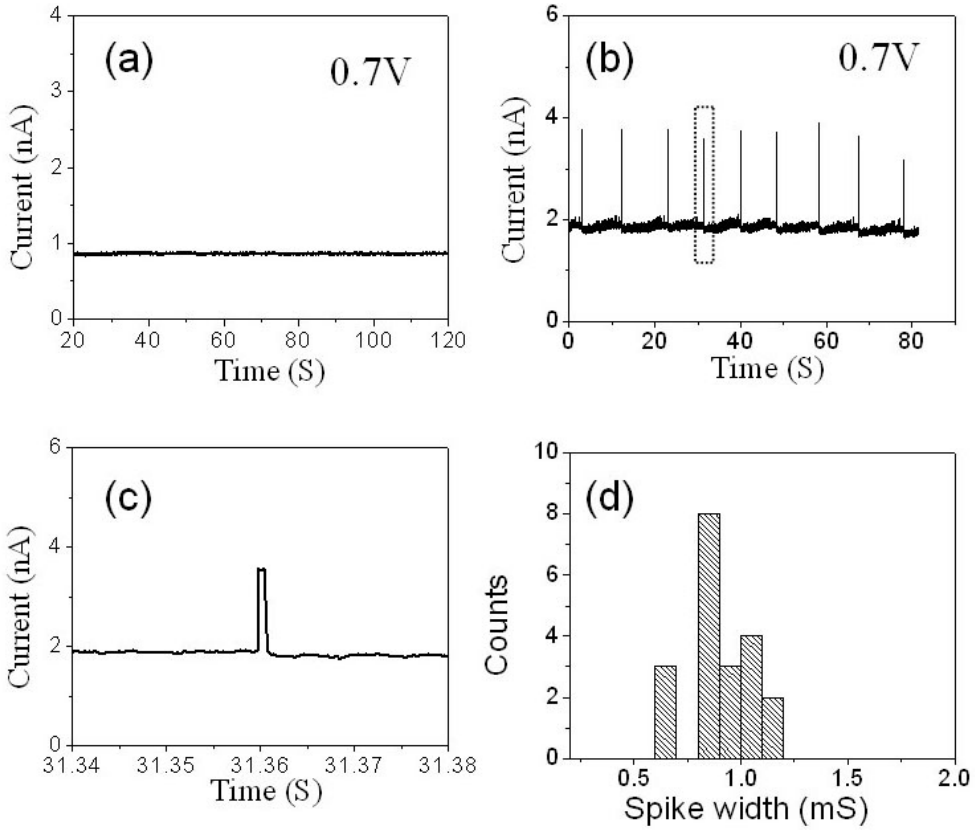

Figure 4.6. (a) An example of ionic current versus time at an applied voltage of 700 mV in 1M buffered KCl solution (1mM PBS, pH 7). (b) Upward spikes appear in the ionic current versus time at an applied voltage of 700 mV after the addition of 5μM guanosine triphosphate (GTP) GTP (1M KCl, 1mM PBS, pH 7) into the input reservoir. (c) A zoom-in of one typical current spike in (b) (inside the dot lines). (d) The histogram of the spike width. The average duration of the spike is 0.86 ± 0.15 ms.

To test for this possibility, we used a guanosine 5'-triphosphate (Sigma Aldrich, HPLC grade) molecule. The device has a SWCNT bridging 2 μm barrier. Two control devices were fabricated on the same chip to test the leakage current. Before the introduction of 5 μM GTP into the input reservoir, the ionic current of the device at 1M buffered KCl (1mM PBS buffer, pH=7) solution was measured

by applying a 700 mV bias at the output reservoir (input reservoir is grounded) for several minutes. An example of the ionic current time trace is shown in figure 4.6 (a). The ionic current was about 1.2 nS. No spikes or other fluctuations were observed in the ionic current. After the introduction a solution of 5 μM GTP in 1M buffered KCl solution, the ionic current gradually increased to 2.9 nS and large transient increases in ionic current were observed at 700 mV. These "spikes" were accompanied by fluctuations in the background current (figure 4.6 (b) and (c)). No spikes were observed, at smaller or negative biases. These spikes must be induced by GTP and are most likely due to the translocation of GTP molecules, although this cannot be tested by PCR. The average spike duration is about 0.86 ± 0.15 ms (figure 4.6 (d)).

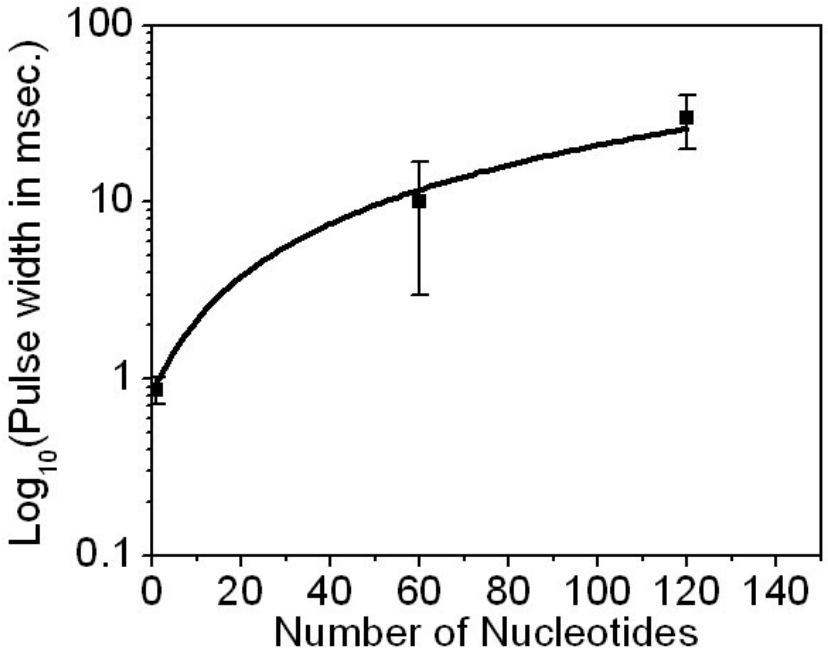

Figure 4.7. Semi-log plot of the average pulse width versus the number of nucleotide in the ssDNA oligomers. The solid line is a non-linear, power-

law fitting (~0.08 $N^{1..2}$) to the experimental data. The bias is 500 mV for oligomers and 700 mV for GTP.

Figure 4.7 shows a plot of the log of the average pulse width for 120 and 60 nt DNA (both at 500 mV). The pulse widths are widely distributed, but plotted together with the datum for GTP (at 700 mV), they suggest a non-linear, power-law relationship (~ 0.08 $N^{1.2}$) between the number of nucleotides and translocation time. For the purposes of this plot, GTP has been shown as N=1. If the backbone charge is the important physical parameter, then the GTP data point should be moved to N=3. The errors in the data are such that this would not alter the important implication of a power-law relationship between pulse width and polymer length. Certainly, this relation needs to be further verified on much longer ssDNA.

4.4 Translocation of small single stranded DNA oligomers

In order to test for DNA translocation, we used 60 nt and 120 nt DNA oligomers with sequences that were predicted to be relatively free of secondary structure, with forward and reverse primers chosen to have high melting temperatures to minimize primer dimers and false priming. Devices were first characterized by measuring current flow with 1 or 2 M KCl alone, and then a DNA solution (1 or 2 M KCl, 1mM phosphate buffer, pH7) was flowed into the input reservoir side. A control aliquot was collected from the output reservoir to test for DNA contamination, and a positive bias then applied to the output side of the device. We first observed a slow increase in the background current (Figures 4.8A and

B). After a time, which depended on DNA concentration in the input reservoir, large transient increases in current were observed. These "spikes" were accompanied by large fluctuations in the background current (Figure 4.8C). The spikes disappeared when the polarity of the bias across the tube was reversed, and re-appeared when the original bias (positive on the output side) was restored. Quantitative polymerase chain reaction (q-PCR) showed that DNA was translocated in devices manifesting these large spikes. These were generally tubes with conductances (prior to DNA addition) of > 2 nS (diameters ≥ 2nm). Some devices that showed similar instabilities in the background but no large current spikes (Figure 4.8F) gave negative PCR results. We also tested for translocation in "failed" control devices (i.e., lacking the CNT) that displayed leakage current. Some, with large leakage current showed evidence of DNA in the output well, but none displayed spikes, regardless of the magnitude of the leakage current. Thus, the spikes signal translocation of DNA through the SWCNTs.

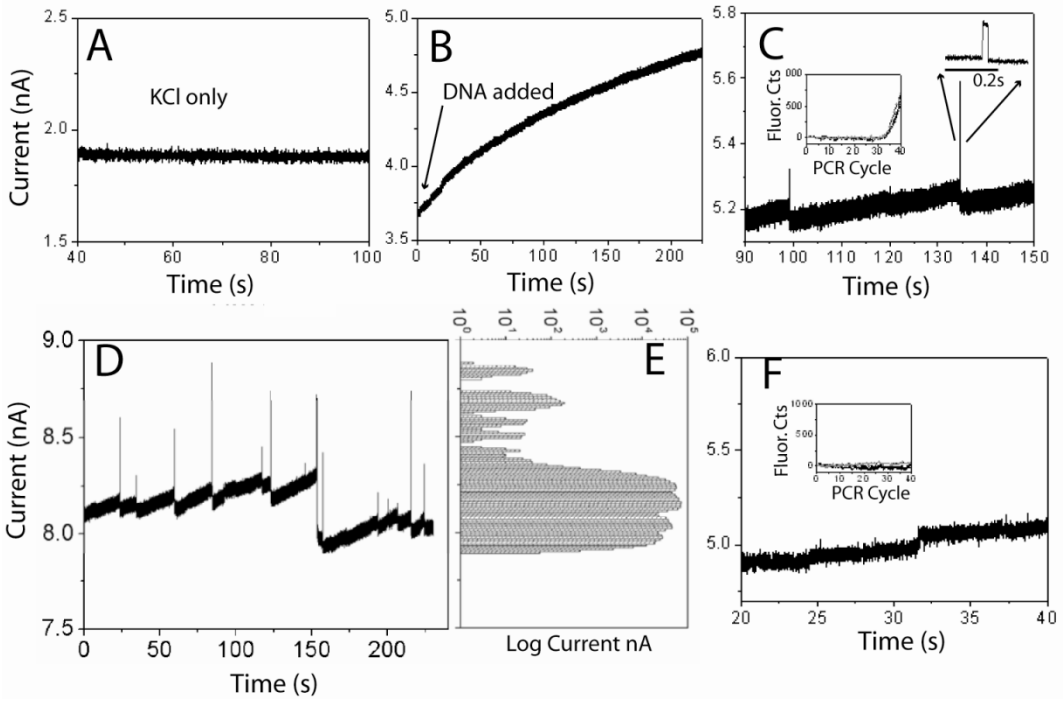

Figure 4.8: Signals of DNA translocation: A. Current (2M KCl, 1mM PBS pH 7) prior to DNA addition. B. After DNA addition, current slowly increases. C. 5 minutes after addition of 0.1 nM 60 nt DNA, large positive current spikes appear. These are followed by a drop in baseline over a period of a second or so, and then by a gradual rise leading to the next spike. D. Representative data from another tube (also 60 nt DNA) with the distribution of currents shown in E. The DNA causes large changes in baseline in addition to the spikes. F. Data from a tube that showed both a current increase on DNA addition and baseline fluctuations but no spikes. No translocation was detected by PCR. The insets in C and F show the fluorescence signal from dsDNA dye labels as a function of the PCR cycle number for samples collected from these particular runs.

Quantitative PCR also provides a measure of the number of molecules collected. We collected small aliquots of fluid from the output reservoir by flushing the system through with water, and concentrating the solution using a Microcon YM-10 centrifugal filter so that we could redilute with PCR buffer. The filter losses were found to be highly variable, more so at low DNA concentrations, and this accounts for much of the stated uncertainty in our results.

We calibrated the PCR reaction with known amounts of DNA and, for one data point, calibrated filter losses by mixing a known amount of a second sequence (with orthogonal primers) and carrying out a PCR analysis of both the target and calibration samples. The final molecule count was corrected for filter losses and dilution during the sample collection. The various errors in these steps tend to *underestimate* the amount of DNA that translocated (but contamination has the opposite effect) so the final results are probably lower limits. PCR was limited to the first use of a device and we rejected samples from chips that showed contamination in the control samples collected. We were able to carry out PCR on samples collected from 11 devices that had a conductance > 2 nS (about 20% of the total working devices). Of these, four had DNA contamination in control samples, leaving the seven tubes listed in Table 4.1. Two of these showed no spikes and yielded no PCR signal. The remaining five all appeared to pass more than one molecule per spike. In particular, tube HL-4-1-36, for which the filter recovery was directly measured with a control sample, passed at least 30 molecules for each spike. If these numbers are lower limits, then it is possible that the tube fills entirely with DNA, the spike signaling the cooperative emptying (or possibly filling) of the tube. The uncertainties in the PCR measurement are too large to reveal any significant difference between the number of molecules per spike for the 60 nt sample (23, 13, 34) and the 120 nt sample (88, 16) though the spike frequency was much lower in the two 120 nt runs, and the spike duration significantly longer.

Tube	Tube Conductance nS (1M KCl)	DNA Sample (nt)	Number of Spikes	Number of Molecules	Molecules per spike
AD1	9.7	60	350±50	8000±2000	22.9±5.7
AD2	9.5	60	30±10	400±200	13.3±6.6
AA New1	19.6	120	64±10	8500±3100	88±48
AA New2	2.7	120	1500±200	24400±5700	16.3±3.8
HL-4-1-36	9.6	60	36±4	1224±774*	34±21.5
HL-4-1-41	4.8	60	0	0	-
HL-4-1-40 O8	2.7	60	0	0	-

Table 4.1 Results of q-PCR for tubes with conductance > 2 nS that gave uncontaminated control signals. Errors in spike count reflect the consequences of different cut-off criteria for selecting spikes. Errors in the molecule count were dominated by uncertainties in the filter recovery efficiency, except for the datum labeled * which was calibrated with a second oligomer.

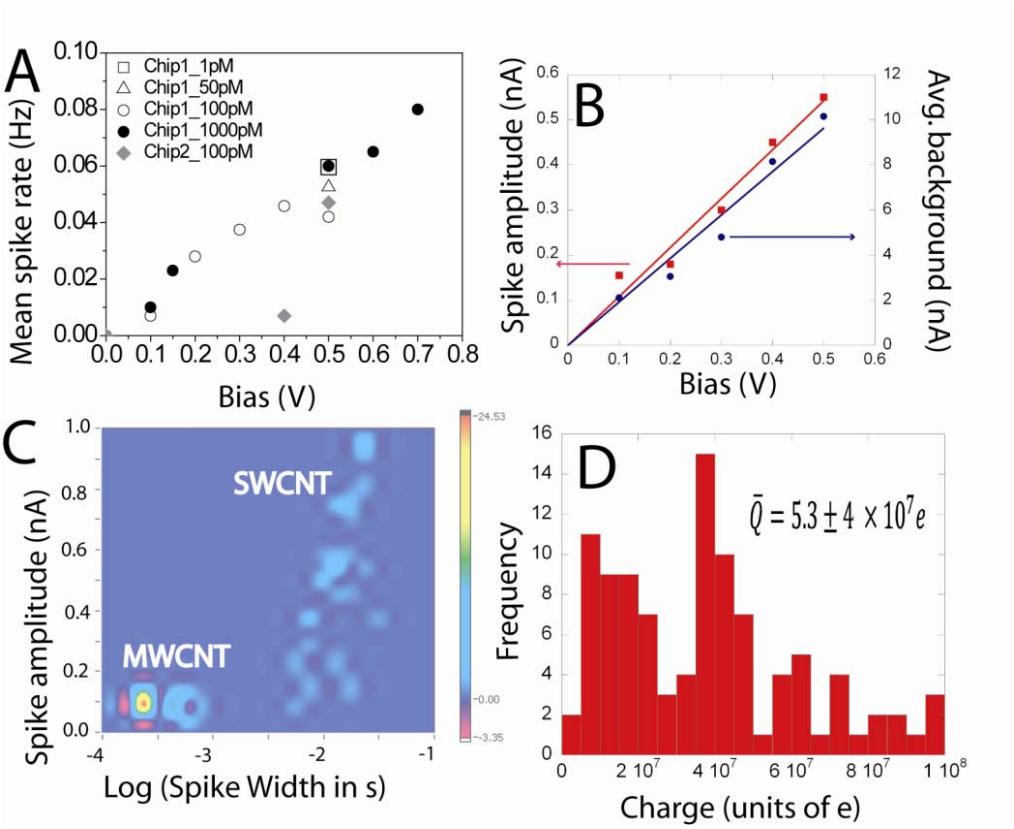

Figure 4.9: Characteristics of the translocation signals for 60 nt DNA: A. Spike rate increases with bias after a threshold that depend upon the particular CNT – the two devices here show spike signals above 0.1 and 0.4 V. The rates were not dependent on the initial DNA concentration, but longer wait

times were required at lower DNA concentrations. B. Spike amplitude (red points) increases linearly with bias, being about 5% of the background current (blue points). C. Histogram of spike events (count is color-scaled) as a function of the log of spike durations and amplitude. Spike duration was around 10ms and spike amplitude varied from 100 pA to 1 nA. For comparison, we also plot amplitude and duration data for negative-going current spikes (current-blockades) observed in a multiwalled tube ("MWCNT"). D. Distribution of the charge in each spike for the SWCNT in units of e. The larger peak corresponds to the spikes shown in Figure 4.8, though a number of devices also showed an additional set of smaller spikes at the highest bias, and these give rise to the smaller charge transfer peak.

Figure 4.9A shows data for the spiking-rate as a function of bias for two different tubes passing 60 nt DNA. The spike rate increased with applied bias, and the two tubes showed different threshold biases for the onset of spikes (and hence translocation). The spike frequency did not depend on DNA concentration, probably because DNA is concentrated at the input side of the tube during the initial application of bias prior to the appearance of spikes (Fig. 4.8B). Evidence for this pre-concentration is found in the wait time (the period for which background current increases prior to the onset of translocation spikes) which increases with decreasing DNA concentration.

For the 60 nt DNA, the spike amplitudes are about 5% of the baseline current (Figure 4.9B) and their duration is between 10 and 20 ms, independent of spike amplitude (Figure 4.9C). The product of the spike duration and amplitude yields the charge contained in each spike (Fig. 4.9D). This is remarkably large, at about a pC or 10^7 electrons. Fan et al. explained positive charge spikes observed in nanochannels as a consequence of additional mobile ions brought into the channel by DNA molecules. [83] If our tubes (2 μm long) were entirely filled

with one hundred (20 nm long) 60 nt DNA oligomers, each carrying 60 mobile charges, the spikes would represent > 1000 fold amplification of the charge carried by the DNA. Even packed solid with ions (the hydrated radius of K^+ and Cl^- is about 0.33 nm) the tube could only hold about 10^{-3} of the charge released in each spike. Two possible explanations for this are (a) that the presence of DNA inside the tube enhances the (already anomalously large) ionic conductance yet further or (b) that the spikes originate in changes in a region of polarization in the reservoirs outside the tube, much as has been observed in junctions between micro- and nano-channels. [84] The observed pH dependence of the ionic current through the tubes shows that surface charges at the entrance to the tube play a role, suggesting that polarization at the ends of the tubes is important. Changes in this polarization as DNA translocates might provide the large charge signals, but multi-scale modeling is required to clarify the origin of these features.

Then we turn to investigate in more detail the timescale associated with DNA accumulation at the input to the SWCNT. The reference electrode in the DNA input reservoir is grounded as shown in figure 4.10 (a). 0.1 nM 60 nt ssDNA is injected into the input reservoir. Both reservoirs contain 1M KCl solution with 1mM PBS buffer (pH 7). Translocation requires that the output reservoir is biased positive with respect to the input reservoir. After the onset of tranlocation signals, we investigated the effects of reversing the polarity applied to the device.

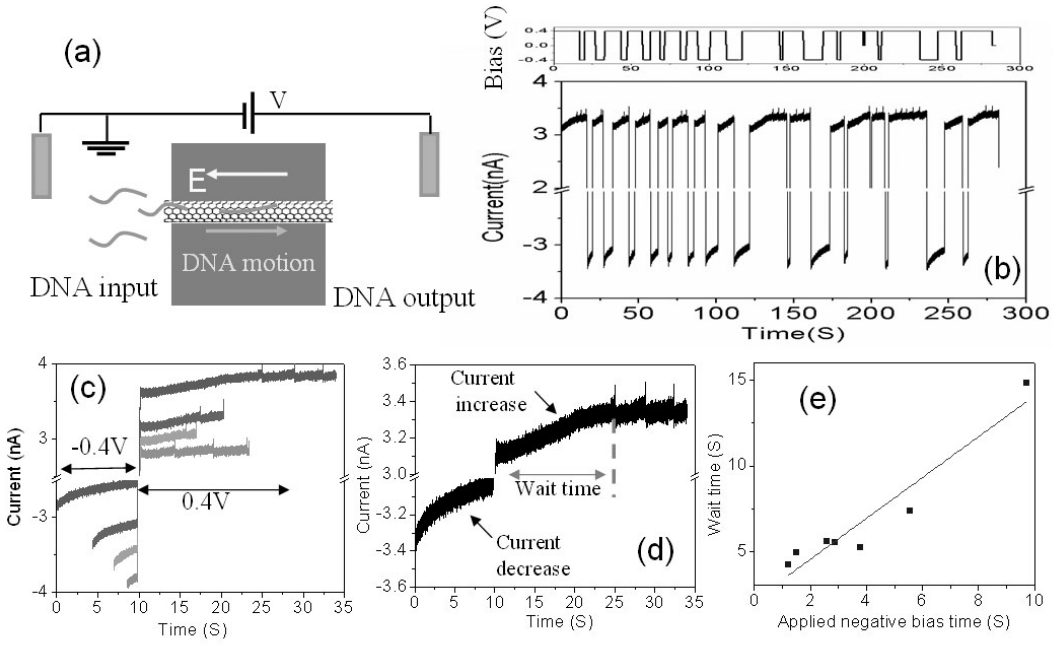

Figure 4.10. (a) The schematic of a DNA translocation measurement setup. The electrode at input reservoir is always grounded. 0.1nM 60 nt DNA is injected in the input reservoir. (b) The time trace of ionic current when switching the polarity of bias at output reservoir. (c) Re-organized ionic current data by aligning ionic current at voltage transition position. (d) The zoom-in of one typical data. The current magnitude always increases at positive bias and decreases at negative bias. Spikes appear after a wait time at positive bias and no spikes at negative bias. (e) The relationship between the wait time and the applied negative bias. The solid line is a linear fit to the experimental data.

We switch the bias between -0.4 V and 0.4 V back and forth frequently and recorded the ionic current through the device. A typical time trace of the current is shown in the lower panel of figure 4.10 (b). The applied voltage versus time is shown in the upper panel of figure 4.10 (b). The ionic current data in figure 4.10 (b) can be reorganized by aligning ionic current at the negative to positive voltage transition position. The re-plotted data is shown in figure 4.10 (c) – lines to the left of 10s (arbitrarily set to the transition time) represent current versus time as

the output reservoir sat at -0.4V (time stopping at 10s), while those to the right represent current versus time as the output reservoir sat at +0.4V (time starting at 10s). Note that translocation spikes are only observed when the output reservoir is positive, as previously reported [1].

One recording through a bias reversal is expanded in Figure 4.10 (d) to show the wait time for the onset of translocation spikes more clearly. The wait time is plotted vs. the period for which bias was reversed in Figure 4.10 (e). Clearly, DNA is swept away from the entrance to the device when the input reservoir is biased positive. The recovery time for the onset of signals is very close (slope = 1.2) to the time for which the bias was reversed. This suggests that the wait time reflects the time needed to acquire an adequate concentration of DNA on the input side of the tube. Such a pre-concentration process has been demonstrated in other microfluidc to nanofluidic interfaces [85, 86]. So the existence of a wait time may suggest that the DNA translocation can only start when the local DNA concentration at the entrance achieves a critical level. This might imply a collective DNA translocation (i.e. more than one molecule translocating at a time), consistent with the measured relationship between the number of translocation spikes and amount of DNA translocated [1].

4.5. Conclusions

In conclusion, we have successfully fabricated individual CNT based nanofluidic devices and demonstrated the translocation of ion and DNA through individual SWCNTs. The device fabrication methods are straightforward and can be

generally applied to SWCNTs, MWCNTs, carbon nanofibers and *etc*. The new data for the translocation times of GTP are suggestive of a power-law relationship between translocation time and polymer length. If this turns out to be a generally valid result, it is important because it predicts a very slow translocation speed of very long DNA through devices. More data is needed on the relationship between translocation time, applied bias, polymer length, tube diameter and tube length. The correct choice of tube dimensions might permit translocation of long DNA while also slowing it to a speed that matches sequence readout. This is a critical missing component of current nanopore devices where translocation is generally much too rapid [42]. Our study of the wait times points to the pre-concentration of DNA at the entrance to the device. This is clearly important because it suggests that very small amounts of DNA could be handled simply by increasing the wait time for translocation.

Individual CNT based nanofluidic devices may open new avenues for fundamental research, such as molecular confinement and mass transport at nanoscale, and practical applications, such as new schemes for DNA sequencing and new type of single molecule sensor. To achieve these goals, significant efforts in experiment and theory are needed. We will continue to improve the device fabrication methods, carried out detailed and systematic experiments, and also use large multi-scale simulations to understand the considerable number of new physical and chemical phenomena appeared in these devices.

Chapter 5

ELECTRONIC SENSITIVITY OF CARBON NANOTUBES TO INTERNAL WATER WETTING

We have constructed devices in which the interior of a single-walled carbon nanotube (SWCNT) field-effect transistor acts as a nanofluidic channel that connects two fluid reservoirs, permitting measurement of the electronic properties of the SWCNT as it is wetted by an analyte. Wetting of the inside of the SWCNT by water turns the transistor on, while wetting of the outside has little effect. These observations are consistent with theoretical simulations that show that internal water both generates a large dipole electric field, causing charge polarization of the tube and metal electrodes, and shifts the valance band of the SWCNT, while external water has little effect. This finding may provide a new method to investigate water behavior at nanoscale. This also opens a new avenue for building sensors in which the SWCNT simultaneously functions as a concentrator, nanopore and extremely sensitive electronic detector, exploiting the enhanced sensitivity of the interior surface.

This chapter is based on the paper *"Electronic sensitivity of carbon nanotubes to internal water wetting"* published in *ACS Nano*, 2011 [25]. I list as the first author and finish 80% of the device fabrication, experiment setup and all kinds of measurements.

5.1 Introduction

The excellent electronic properties, small pore size and large surface to volume ratio of single-walled carbon nanotube, SWCNT, form the basis of a large number of new types of electronic sensors[87-89] in which analytes generate a signal by binding to the outside of a SWCNT. However, the interior of SWCNT is unexplored territory for chemical and biological sensor applications. Here, we address the question of how *internal* water wetting affects the electronic properties of the SWCNT (and the properties of the contacts to it).

Counter intuitively, the hydrophobic interior of SWCNTs is readily wetted because the surface tension of water is much lower than the threshold value.[90, 91] Microscopically the chemical potential of water is lower inside the SWCNT than in the bulk,[47] and water can be transported at many thousand times the speed possible with classical Poiseulle flow.[47, 57, 58, 92] Internal wetting of CNTs has been verified by transmission electron microscopy (TEM)[93] and a number of spectroscopy methods,[94-98] showing that water is ordered inside a CNT. The transport of water, ions and small molecules through CNTs has also been studied experimentally using membranes consisting of billions of carbon nanotubes in parallel.[57, 58, 99] Recently, we reported studies of ion and DNA translocation through individual SWCNTs[1] by making devices in which just one SWCNT connects two fluid reservoirs. Ionic currents were found to be much larger than predicted by a standard electrophoresis model and DNA translocation was accompanied by electrical signals that differed drastically from what is

observed in other inorganic nanopores.[100-102] A very recent study showed yet another (proton dominated) mode of transport in very long SWCNTs.[103]

SWCNT field effect transistors (FETs), show that the electronic properties of SWCNTs are sensitive to their diameter, chirality, defects, doping,[104] adsorbates[105, 106] and environment[88], though these effects can be masked by the dominant role of Schottky barriers at the metal-SWCNT junction.[107, 108] Wetting of the outside of SWCNT-FETs by water changes their hysteresis and shifts their threshold gate voltage (V_{th}).[109-112] The resistivity of SWCNT mats falls when they are wetted (possibly both inside and outside)[96, 113] but these results are difficult to interpret in terms of the response of individual SWCNTs. Thus, we have used our new devices, in which just one SWCNT connects two fluid reservoirs to compare the effects of external and internal wetting on SWCNT FETs.

5.2 Exepriment setup

We first grew well-separated single-walled carbon nanotubes (SWCNTs) on phosphorus-doped silicon wafers (used as a back-gate) with a 1000 nm of thermal oxide. Cobalt nanoparticles were used as catalyst and the carbon source was ethanol vapor. Conditions were chosen to produce high quality SWCNTs with an outside diameter of 1 to 2 nm. Gold markers and large electrical pads were fabricated using optical lithography. SEM images were used to locate the SWCNTs position relative to the markers. After SEM imaging, the chips were heated at 400 ^{O}C in Argon for 1 hour to remove resist residue. Immediately after

cleaning, the Au/Cr metal electrodes for contacting the SWCNTs (normally 5 μm in width and 40nm/5 nm in thickness) were fabricated using electron beam lithography (EBL) and the electrical properties of SWCNT were measured in ambient air. SWCNTs with good electrical properties were selected for the next step. We then spun-on a 900 nm thick layer of polymethylmethacrylate (PMMA, A8) over the entire device structure, and wells were formed along the path of a SWCNT using EBL aligned relative to the markers. The electrical measurements were carried out in a home-built probe station inside a faraday cage. A Keithley SourceMeter 2636A, a Keithley low noise current meter 6514 and a function generator (DS 345, Stanford research system) were used and controlled by custom labview programs.

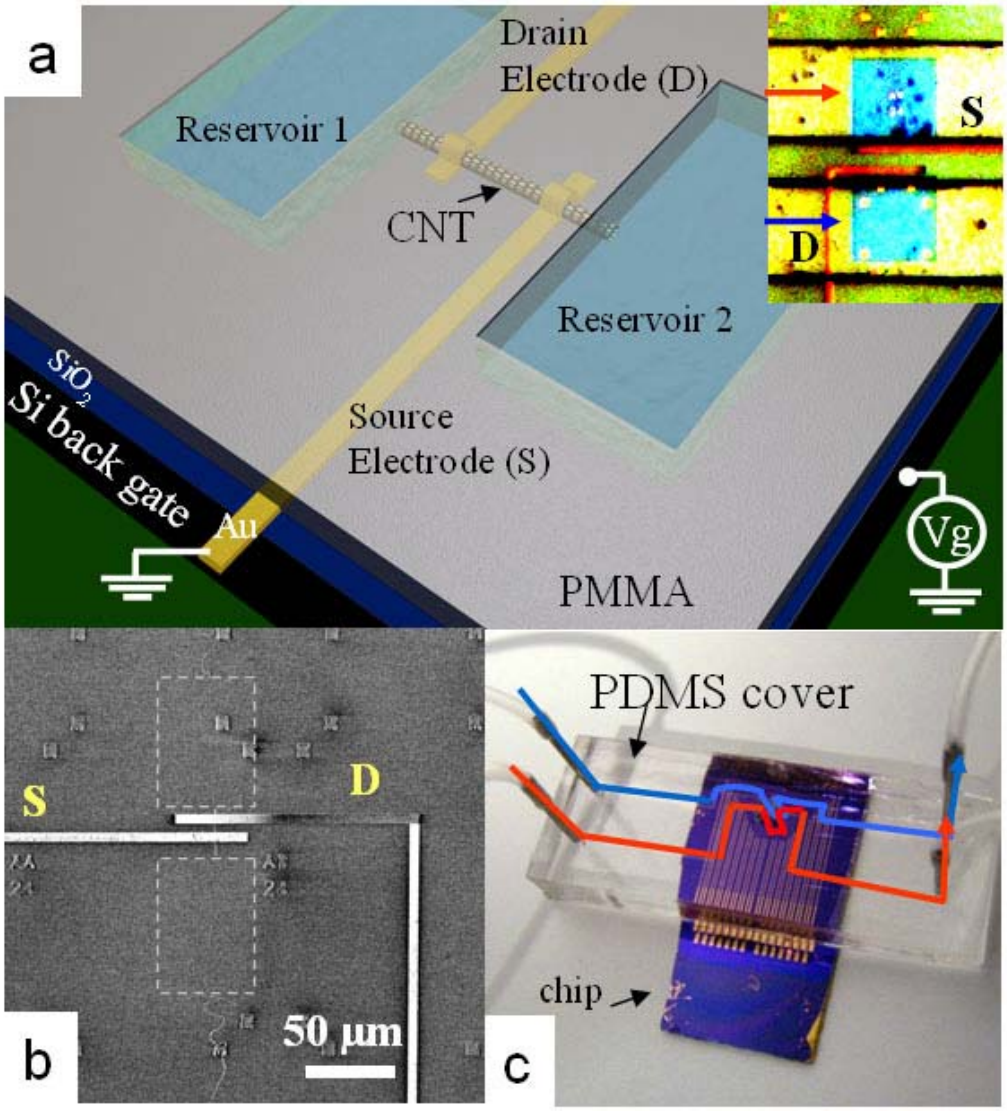

Figure 5.1. Measurement of a SWCNT nanofluidic channel integrated with a SWCNT field effect transistor. (a) Schematic of the device structure and electrical measurement configuration. The inset shows an optical image of a device. The two blue squares (*i.e.*, 60 µm x 60 µm) are the fluid reservoirs cut into the PMMA (yellow). Areas contacted by the PDMS cover are shown in green. Fluid flow in the PDMS channels is indicated by the red and blue arrows. The distance between source (S) and drain (D) electrodes (red) is 15µm. (b) Scanning electron microscopy (SEM) image of a single reservoir device after stripping off the PMMA layer to show the SWCNT lying under the electrodes. The areas labeled by the gray dashed squares indicate the position of the reservoirs. (c) Optical image of a device assembled with a PDMS cover for solution delivery. The read and blue lines show the fluid paths.

The combined nanofluidic-CNT-FET is shown in Figure 5.1. It consists of a single SWCNT that connects two fluid reservoirs formed in a PMMA resist using e-beam lithography. Source and drain electrodes are evaporated onto the SWCNT under the barrier[114, 115] and a heavily doped p-type silicon substrate acts as a backgate. Only the SWCNT under the barrier remains after the exposed SWCNT in the reservoirs has been etched with an oxygen plasma.[1] The fluidic path is completed by attaching a PDMS cover containing microfluidic channels. Further details of the fabrication are given in the methods.

5.3 CNT-FET water wetting phenomenon

We first characterized individual p-type semiconducting CNT-FETs prior to open the SWCNT, both dry and with the exposed SWCNT wetted. We then opened the SWCNTs and recorded FET characteristics with the tube dry and wet. Only internal wetting had a significant effect on the characteristics of the device. Furthermore, vacuum drying of the SWCNT restored the pre-wetting characteristics. For controls, we (a) exposed the SWCNT between source and drain electrodes and wetted the tube externally in this region; (b) Connected an electrode to the fluid reservoir and altered its potential (the extent possible with pure water) (c) Varied the degree of plasma treatment of the reservoirs to alter surface charge in the reservoirs. (See water gate and control parts shown later) None of these controls altered the response of the SWCNT significantly. Thus, we conclude that water on the inside of the tube affects the contacts (and probably the band structure) of the tube in a way that water on the outside of the tube does not.

Representative data for one tube before opening are shown in Figure 5.2a. The source-drain current (I_{DS}) versus backgate voltage (V_{GS}) curves are for the dry tube in air (black curves) and for the tube externally-wetted in the reservoir area (red curves). We observe an increase of hysteresis and a shift of the threshold gate voltage (V_{th}) as reported earlier for external wetting.[109-112] Immediately after a gentle (~30sec, 7.2 W) oxygen plasma treatment to open the SWCNT (Figure 5.2b), we find that I_{DS} decreases a little in the saturation current region and V_{th} shifts slightly (black curve, Figure 5.2b). The characteristics change dramatically a few minutes after injection of water into the reservoir to wet the interior surface of the tubes (red curve, Figure 5.2b). The backgate bias no longer has any effect over the range of bias we can apply without breakdown. The transition is independent of drain-source bias as shown in heat maps (Figure 5.2c,d) of I_{DS} as a function of both V_{DS} and V_{GS}. Transistor action in the dry device (Figure 5.2c) is abolished over the entire range of V_{DS} and V_{GS} when it is wetted internally (Figure 5.2d). Furthermore, the effect is quite reversible: vacuum drying restores the function of the backgate (grey curve). Note that the "on" conductance of the tube does not change dramatically when the tube is internally wetted, the main effect being abolition of the action of the backgate.

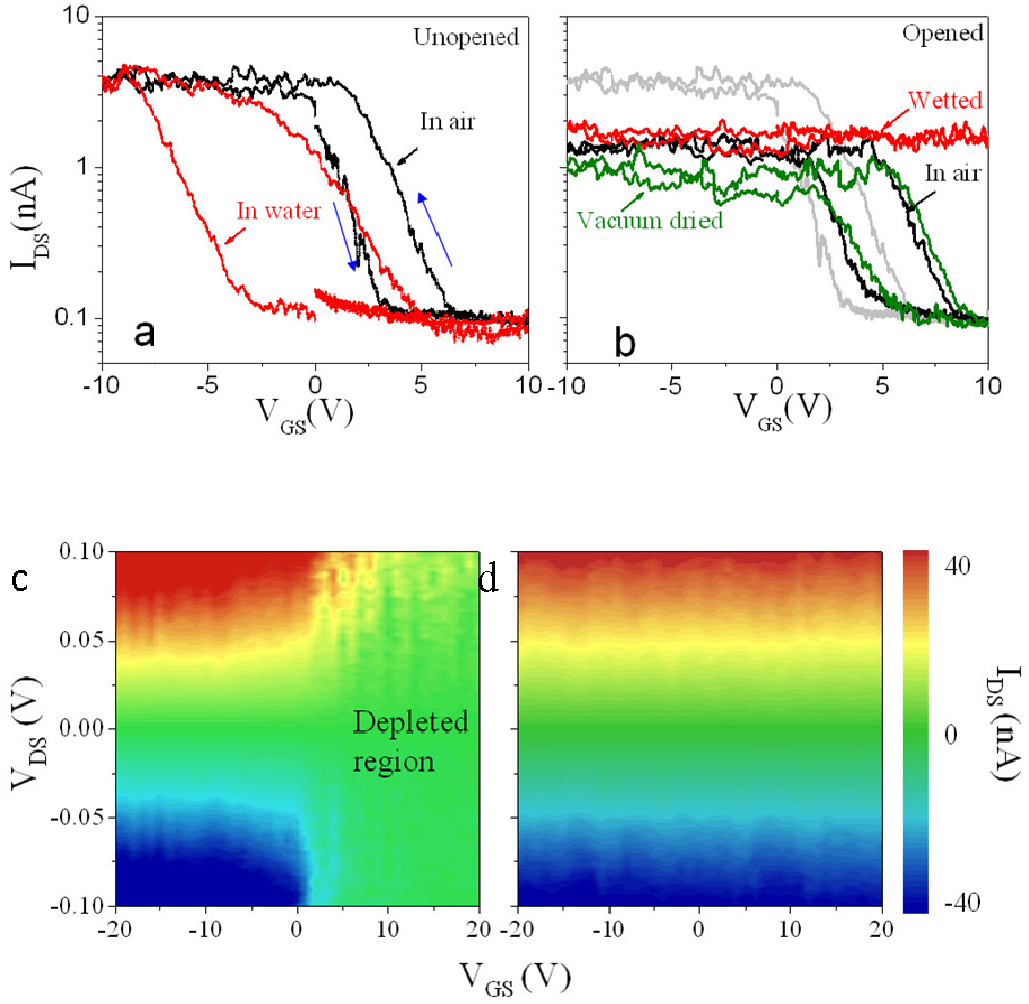

Figure 5.2. Effects of wetting on electronic transport in a SWCNT. (a) External wetting: I_{DS}-V_{GS} semilog curves for an unopened p-type SWCNT device before (black) and after (red) filling the reservoirs with water at V_{DS}=0.5V. The blue arrows indicate the direction of the V_{GS} sweep. (b) Internal wetting: I_{DS}-V_{GS} curves (V_{DS}=0.5V) before opening (grey), after opening with an oxygen plasma (black), after water is added to the reservoirs (red) and after the tube is subsequently dried in vacuum (green). (c) Heat map of I_{DS} (green = zero current) as a function of V_{GS} and V_{DS} for an unopened p-type SWCNT-FET. (d), as in c but internally wetted. The SWCNT is now ohmic over the entire range of V_{GS} and V_{DS}.

When a p-type SWCNT-FET (keeping the electrodes protected) is externally wetted, its threshold moves towards more negative gate bias and hysteresis increases. [109-112] Internal wetting produces exactly the opposite

result (Figure 5.3): the threshold moves to more positive gate bias and the hysteresis decreases.

Transport characteristics of a device measured at different times during water filling process is shown in figure 5.3. I_{ds}-V_{gs} curve usually flatten out quickly after water addition. For some devices, the semi-metallic type transition is slow and transport curves can be recorded as wetting proceeds. An I_{ds}-V_{gs} curve taken right after exposure to water (orange) captures a transient state with the threshold shifted positive and the hysteresis significantly decreased.

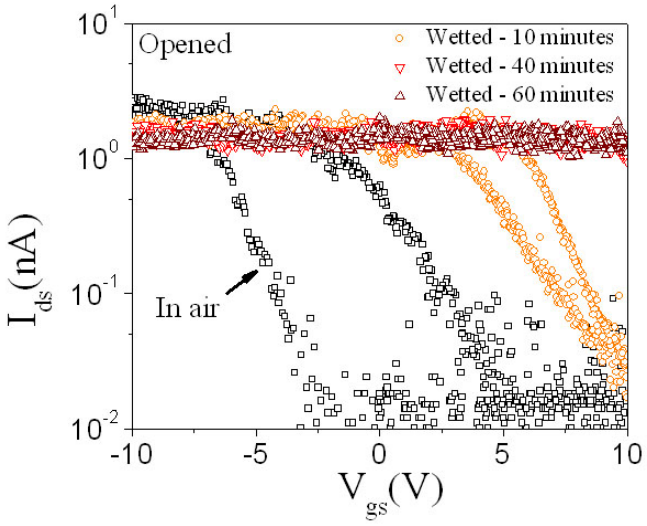

Figure 5.3. I_{ds}-V_{gs} curve of a device (layout of the device is the same as Fig. 5.1a inset) measured at different times during water filling process.

Internal wetting abolished gating reversibly in 11 out of 18 measured semiconducting CNT devices, and diminished it in 3 of the remaining 7 devices (Figure 5.4). Three of the 18 semiconducting devices did not show a full transition to metallic-like behavior on wetting, perhaps because they did not wet

fully. We show representative data here (Fig. 5.4). These devices still showed some hysteresis and a small amount of gating after wetting internally.

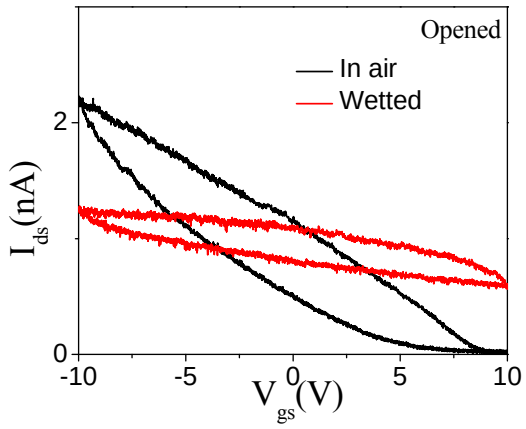

Figure 5.4. An example of I_{ds}-V_{gs} curves for a (black) dry and (red) internally wetted CNT-FET which did not show a full transition to metallic behavior. In this case only one end of the tube was opened so the partial transition may reflect partial wetting.

Thus, the observation is not a result for a specific chirality or diameter, but a rather general property of single-walled semiconducting carbon nanotubes. We also measured 3 metallic CNT devices and all showed *decreased* conductance after water filling (Figure 5.5). Typical results for a metallic tube are shown in Fig. 5.5. Before opening the tube by oxygen plasma, the device showed negligible response to water (Fig. 5.5a). After the tube ends were opened by oxygen plasma, I_{ds} decreased. I_{ds} decreased further after water was added to the reservoirs and recovered after vacuum dried as shown in Fig. 5.5b. The decrease of conductance during filling is shown in Fig. 5.5c.

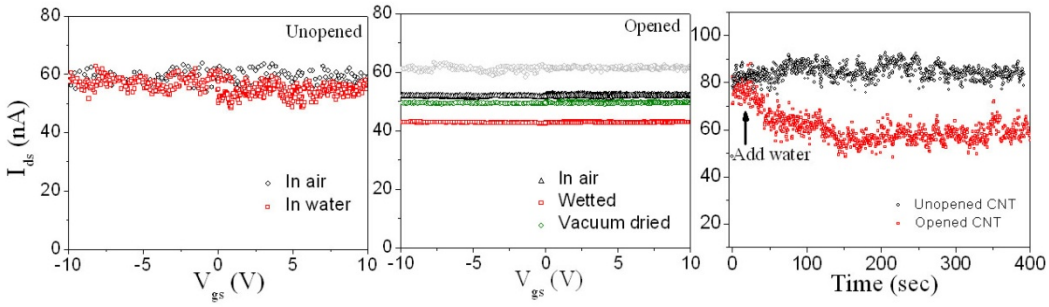

Figure 5.5. a. I_{ds}-V_{gs} curves of a device with unopened metallic SWCNT before (black) and after adding water (red) into the reservoirs. b. The same device was measured after opening with an oxygen plasma (black), after water was added to the reservoirs (red) and after the tube was subsequently dried in vacuum (green). Unopened CNT data (gray) measured in air are shown here as reference. V_{ds} = 0.8V for both (a) and (b). c. I_{ds} time traces during adding water into the reservoirs for both unopened and opened tubes at V_{ds} = 0.8 V and V_{gs} = 10 V.

5.4 Results discussion and water gating test

We have ruled out some trivial causes for this effect. It is not a consequence of a short circuit between drain and source caused by external wetting. No amount of exposure to water alters the p-type FET response unless the SWCNTs are opened. We can also rule out the possibility that oxygen plasma treatment alters the tube in some way. Freshly opened tubes that are not exposed to water show p-type transistor action with characteristics only a little different from those measured prior to opening the tubes (black curves, Figure 5.2b). Another possibility is that the surface charges in the water reservoirs generated by oxygen plasma treatment may "pin" the potential of the CNT (through the poorly conducting medium of the water) out of the range of the backgate potential. We therefore measured the effect of sweeping the potential of a quasi-reference electrode (Pt wire) in contact with the water (water-gate, "V_{wg}" in Figure 5.6). This reference electrode plays

the role of introducing a strongly-charged surface into the reservoir. The electronic transport characteristics of the CNT-FET device (with both unopened and opened CNT) were not sensitive (Figure 5.6) to the potential applied to the "water-gate" potential over a range of three volts, a potential change much larger than could be produced by any reasonable change in surface charge. Thus we can conclude that surface charges in contact with the water reservoir do not play an important role in our device. The most likely explanation for this is the high resistivity of (reasonably) pure water. Thus the potential of water inside the tube will be dictated by interactions with the tube, unless salt is added to the reservoirs.[116]

We have used a reference electrode to "gate" the water potential in the reservoirs. The experiment setup is illustrated in Figure 5.6a. A hydrogen-flame cleaned platinum wire was used as qausi-reference electrode, which controls the water potential to the extent that it influences the concentration of the small number of ions in DI water. A true reference electrode cannot be used because, as we point out before, the presence of salt in the solution washes out the water gating.

We measured the effect of sweeping the potential of the reference electrode ("V_{wg}" in Figure 5.6a) in contact with the water. The range of water gate bias is set to avoid the onset of large electrochemical current (EC current in figure 5.6c). Two devices with both unopened and opened CNT were measured. The results are shown in Figure 5.6b-d. Transistor action of the CNT device was not

sensitive to the potential applied to the "water gate". Only a slight decrease in I_{ds} was observed at positive V_{wg}.

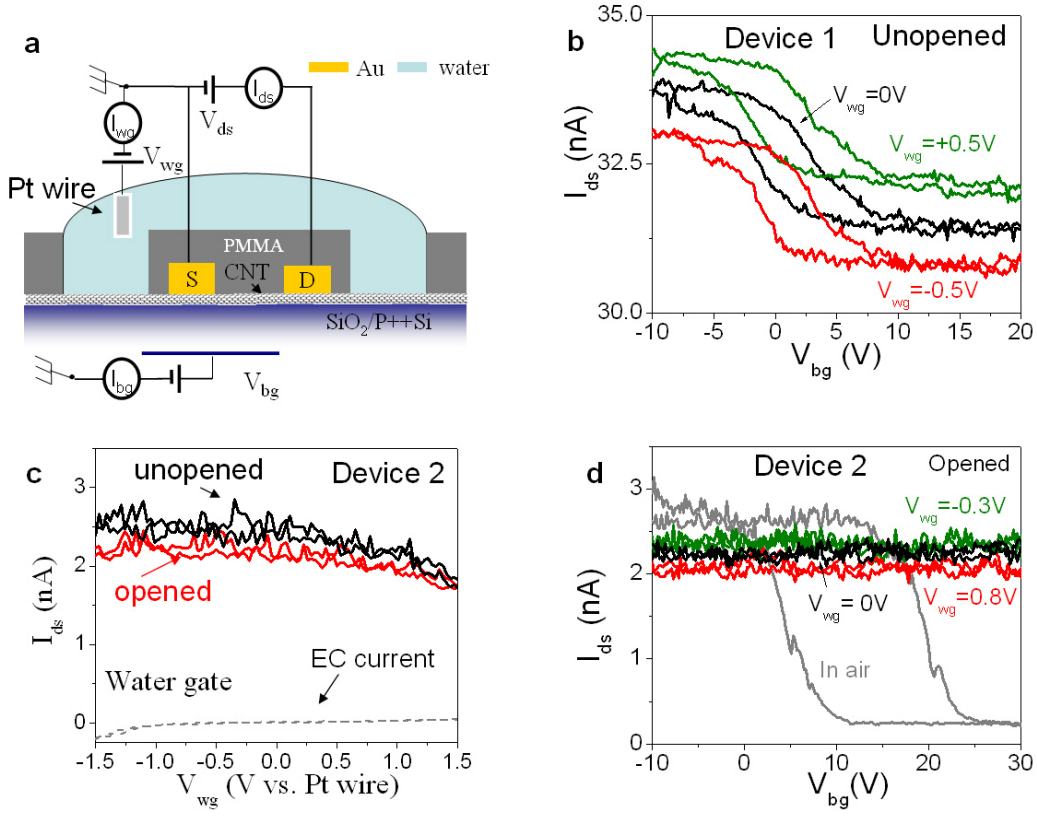

Figure 5.6. a. The illustration of the water gating experiment for an unopened CNT. Pt wire is used as the water gate electrode. Pure water filled the reservoirs. Both water gate bias (V_{wg}) and back gate bias (V_{bg}) are applied to gate the CNT FET device in the measurements. b. The source drain current (I_{ds}) of device 1 with unopened CNT as a function of V_{bg} at different V_{wg}. The V_{ds}=0.1V. c. The I_{ds} as a function of V_{wg} of device 2 both for unopened CNT (black) and opened CNT (red). The V_{ds}=1V. The electrochemical (EC) current between Pt wire and the source electrode was measured and the value was negligibly small. d. The I_{ds} as a function of V_{bg} for device 2 with opened CNT. The p-type transistor behavior was observed in air (gray) but disappeared after been wetted. There different V_{wg} were applied to the device but they could not restore the p-type transistor.

5.5 External wetting for control experiment

Studies of external wetting[109-112] have been carried out using a window opened in dielectric material that covers the metallic contacts (Figure 5.7). The difference between internal and external wetting may just reflect the fact that the tube is not wetted all the way up to the contact in the external wetting process. To check for this, we opened a window that exposed the electrodes as well, having first established that current flow through the water in contact with the electrodes is negligible (Figure 5.8a). External wetting of the tube all the way up to the contacts did move the threshold to more positive gate bias but did not result in abolition of gating (Figure 5.8b). So this difference between external and internal wetting does not account for the effects of internal wetting.

Effects of external wetting are shown below. Data from two devices are plotted here to illustrate device-to-device variation on external wetting. The structures of the two devices are illustrated in the insets of Fig. 5.7a and c respectively: only a short section of the SWCNT between the two electrodes is exposed to water. The source (S) and drain (D) electrodes are protected by a PMMA layer. In both devices hysteresis increases and the device remains p-type. A trace of I_{ds} vs. time is shown in Fig. 5.7c. No change was observed after adding water into the reservoir, opposite to the result shown in Fig. 5.3 for internal wetting.

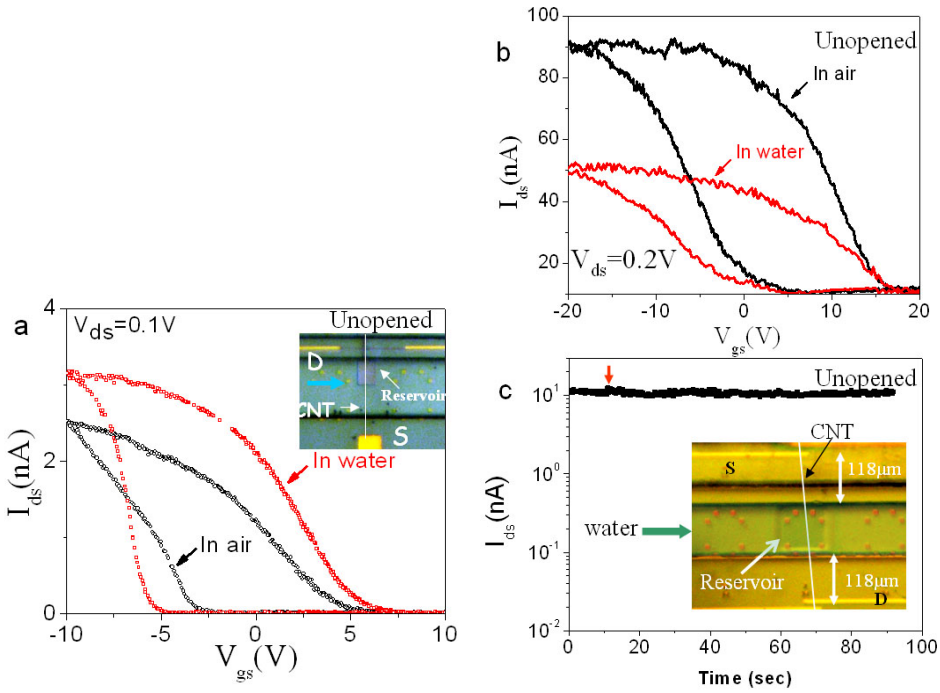

Figure 5.7. External wetting: a. I_{ds}-V_{gs} curves for one control device with a section of CNT between source and drain electrodes in air (black curve) or in water (red curve). As shown in the inset, the reservoir opened along the CNT path is about 60 μm in length and the distance between D and S is about 140 μm. b. I_{ds}-V_{gs} curves of another control device. c. I_{ds} time trace of the same device as (b) when exposing the outside of CNT to a water bath at V_{gs} = 20V and V_{ds} = 0.5V. The optical image of the device structure was shown in the inset.

The results of External wetting with exposed electrodes are presented here. The device structure is shown in the inset of Fig. 5.8a. The reservoir size is 60 μm x 60 μm, the Au electrodes are 5 μm in width and the distance between the two Au electrodes (edge to edge) is 5 μm. We first checked the leakage current between two gold electrodes. When the electrodes are completely covered with PMMA, the current between two electrodes is negligibly small. When the electrodes are exposed to air, some leakage current appears. After adding water to the reservoir, the leakage current increased only slightly.

We then measured the device with a SWCNT between two electrodes. After adding water, the transistor action still remains. However, the threshold voltage V_{th} shifted significantly to the positive direction and the current at subthreshold region increased. (Fig. 5.8b) These changes may due to the modification of gold work function and the Schottky barrier at contacts during external wetting.

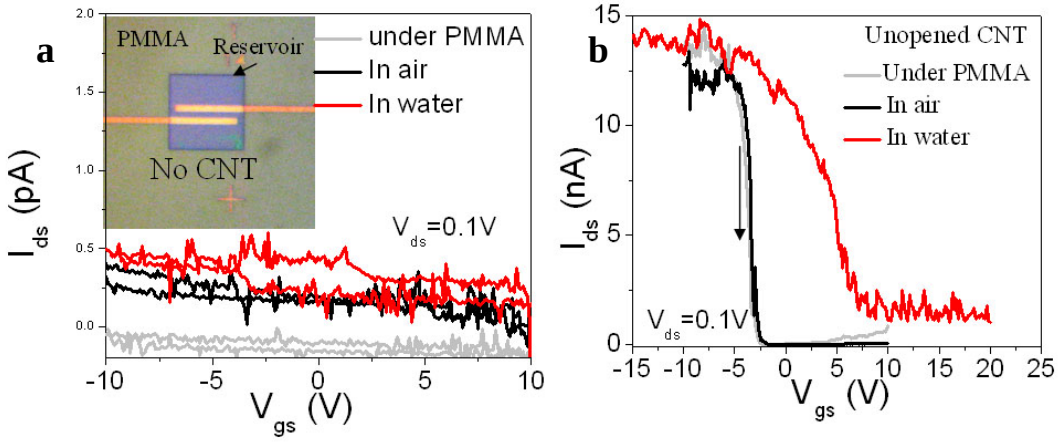

Figure 5.8. I_{ds}-V_{gs} curves of control devices without (a) and with (b) a CNT. The devices were measured before opening reservoir (gray), before (black) and after (red) exposing the metal electrodes to water. For both devices, the reservoir size is 60µm x 60µm and the Au electrode is 5 µm in width and 45 nm in thickness (as shown in the inset of (a)).

Finally, we considered the possibility that the gate field is modified by the dielectric properties of confined water[117] which will alter the capacitance of the tube, and hence its potential at a given gate bias, but estimates of this effect show that it is very small. Thus, we conclude that internal wetting must alter the electronic properties of the SWCNT and/or the Schottky barriers[108] at the contacts in a way that external wetting does not.

5.6 Water wetting theory and principle discussion

In order to investigate these effects further, we carried out molecular dynamics and electronic structure calculations for water confined inside a SWCNT. Turning first to water structures inside the tube, we filled a 2.84 nm long semiconducting (10, 0) tube (0.78 nm diameter) with water and equilibrated the structure (see the theory for details). The resulting water structure is a single-file hydrogen-bonded "wire" (Figure 5.9). The dipole orientation of such water structure and the importance of the dipole orientation to the water transport through CNT have been studied before.[118, 119] According to our estimates, the dipole field of this water structure is in magnitude competitive or even stronger than the electrical field of the backgate in both axial and radial components. This dipole field causes redistribution of the charges at the CNT and contact electrodes which cancel the dipole field but also influences the electronic characteristics of the tube, including Schottky barriers. The water dipole will flip frequently[120] but the flipping can be suppressed by the drain-source field. In contrast, external water generates essentially no dipole field. Thus internal water may generate an electric field and polarizes the tube and metal electrodes that modify the Schottky barrier at the contacts. These effects are not seen at external wetting.

Secondly, internal water may also modify the electronic structure of CNT, as suggested by the IR spectroscopy.[97] We have carried out DFT electronic structure calculations using the same CNT (10,0) tube. The CNT was filled with optimized and thermally equilibrated (300K) water structure (Figure 5.13), using molecular dynamics simulations as discussed in the previous paragraph. A

decrease in the bandgap was observed when water molecules fully fill the CNT (red curve in Figure 5.13c). The CNT bandgap decreases with the number of water molecules (Figure 5.14). The bandgap is also reduced when water molecules are placed outside the tube. However, the decrease is much smaller (~15%) even when a large number (115) of external water molecules were used. The reduction in the bandgap of CNT originated from the enhanced interaction between ordered structure of water molecules and the carbon atoms. Significantly stronger interaction is observed when water molecules are confined inside the tube (insets in Fig. 5.13c), leading to a penetration of the occupied levels of oxygen into the CNT band gap. No shift in the CNT Fermi level was observed and there was no charge transfer between internal water molecules and carbons. The CNT bandgap reduction will lower the Schottky barriers and push V_{th} to a larger positive value.

Theory details

To understand the change of the electronic structure of a semiconducting SWCNT upon filling it with water, we have performed the Density Functional Theory (DFT) calculations on a number of various configurations of a semiconducting nanotube with water, with Molecular Dynamics (MD) simulations used to optimize the distribution of water molecules. The hydration geometries for the DFT calculations of the water-filling for nanotubes was obtained by MD simulation, connecting two reservoirs by the CNT, of which one was filled with water, and recording the system state after approximately filling of 1/4, ½, ¾, and the full tube length. This resulted in a partially ordered "chain"

structure of the water molecules,[121] oriented around the tube axis, as shown in Fig. 5.9.

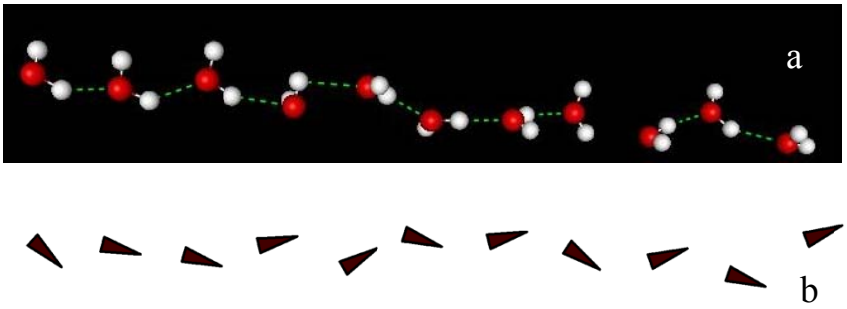

Figure 5.9 a) Partially ordered nanosutructure of the waters, filling the narrow CNT, connecting with H-bonds b) Ordering of the water dipoles; an arrow tip in the direction of a dipole, which is by convention from negative toward positive charge.

Prior to the DFT calculation, we have also calculated the potential surface induced by the water dipole field at the virtual surface overlapping with the CNT surface, as shown in Figure 5.10. The structure of ordered water inside CNT of Fig. 5.9(a) is shown in the inset. The average potential difference between opposite ends of the surface in z-direction is 0.9V on the 2.84 nm CNT, that corresponds to the electric field of 0.32 V/nm The dispersion in potential corresponds to various positions around the circumference of the CNT (at a fixed z) and is due to the angular/radial (deviations from axis) fluctuations of the organized water structure. This causes spatial irregularities of the field, but is close or even higher in magnitude than the back gate field. We note that the CNT used in previous experiments was of larger diameter (1.3 nm), and, as shown by Kolesnikov[121], besides the ordered structure close to the axis, the water filling in this case also creates a water cylinder, the coaxial structure. We were able to

reproduce such structure by filling a 1.3 nm CNT with water. However, the distorted dipole-like electric field from the axial ordered structure was not completely screened by the water cylinder. Therefore, as long as the CNT diameter is small enough the in-filling water organization certainly increases the coupling of the waters with the CNT, as reflected in the DFT calculation.

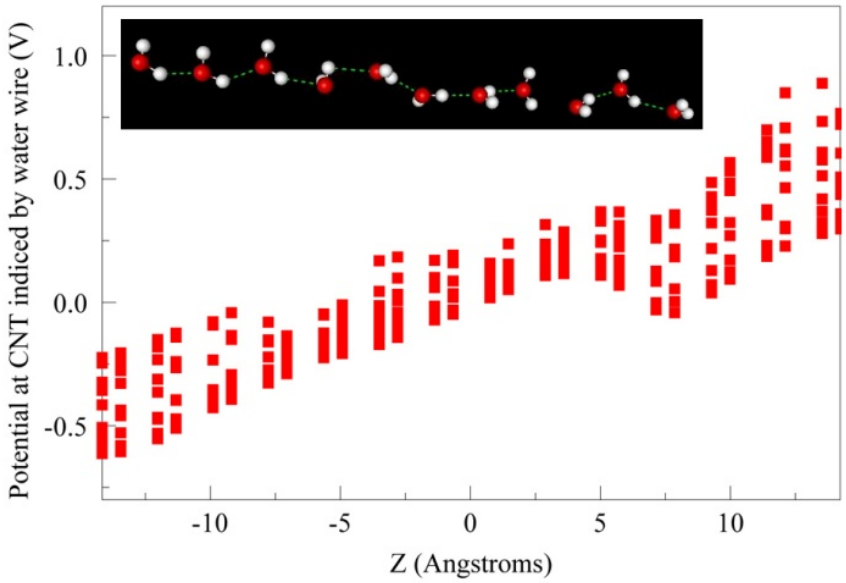

Figure 5.10 The potential distribution of CNT induced by water wire. The structure of water wire (including 11 water molecules) inside a (10, 0) SWCNT of length 2.84 nm is obtained by MD and showed in the inset and in Fig. 5.9.

Prior the DFT calculation, the ends of the CNT in Fig. 5.12(a) were terminated with 30 hydrogen atoms each (not shown in figures), whose positions were optimized prior the water filling. The electronic structure calculation was done with such a terminated "empty" CNT as well as partially (Illustrated in Fig. 5.11, for the half-filling), and fully filled. As the end effects, the terminal layers of CNT with terminating hydrogen were charged upon DFT calculation, in both

cases of “empty” CNT and water filling, and these end charges were almost completely neutralized by the opposite charges induced in terminating hydrogens. To see the possible effect of the CNT charging under influence of the water filling, we have subtracted, upon the converged DFT calculations explained above, the Lowden charges at the CNT of the water filled and “empty” CNT. This, would represent the charging of CNT dues to the dipole filed of the ordered water-filling structure. In Fig. 5.12 we show the integral over the CNT axis of the so obtained charge distribution. It is not zero, but is asymmetric to the CNT center, negative at the side of the CNT where is the positive “end” of the water dipoles (see figure 5.9). Thus, one can expect that the induced charges at the DFT position itself to completely cancel the external water dipole filed. In the process of the water filling the carriers in the CNT redistribute until the water field is cancelled.

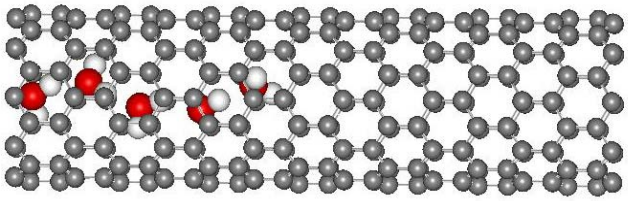

Figure 5.11 A snapshot of the water-filling process: A half-filled CNT.

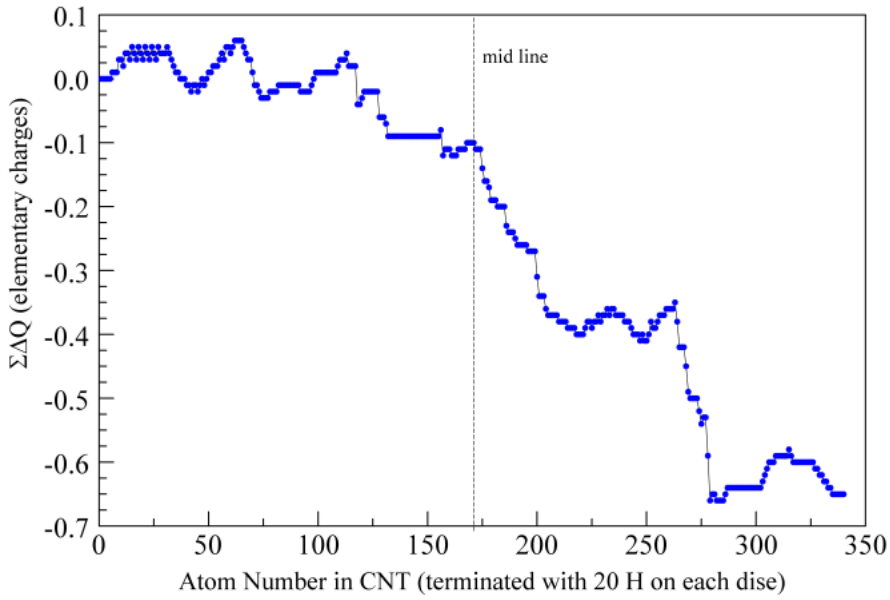

Figure 5.12 The integral of the distribution of charges displaced by the electric field from water potential in (a). The right half of the tube is charged negatively (with excess of about 0.5 e) to null the dipole electric field in axial direction.

The density of states (DOS) of the dry CNT, as well as the full filled systems are shown in Fig. 5.13c, showing a drop of the HOMO-LUMO gap. The DOS was projected at the middle section of the tube. Identical results were obtained by studying the energy of the molecular orbitals of the CNT-water system as function of the electron occupancy, in the vicinity of the Fermi energy, as shown in Figure 5.10a, illustrating also changes in the gap due to the partial water fillings. Interestingly, the Fermi energy is not changing with the water filling and stays about 3 eV in all cases. Since the DFT smearing, needed for convergence of "empty" CNT and internally wetted DFT was 0.13 eV, the density of states of both of these cases is consistently shown for this smearing. However, the smearing needed for externally wetted CNT was 0.54 eV, and the

corresponding density of states was shown here for comparison, though not fully compatible with the shown "empty" CNT calculation.

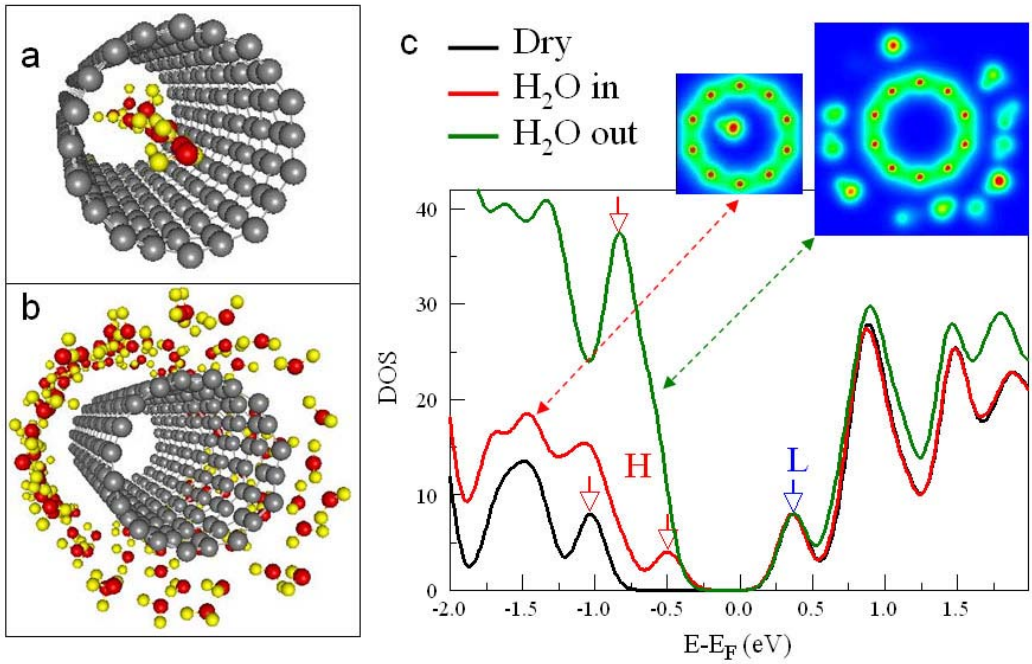

Figure 5.13 Calculated HOMO-LUMO gap for wetted SWCNT: a. Structure of a (10, 0) SWCNT of length 2.84 nm, filled with 11 water molecules (0.13 eV smearing). b. Structure of a (10, 0) SWCNT with 115 water molecules surrounding at the outside of the CNT (0.54 eV smearing). c. Density of States (DOS) for the pristine (black), fully water-filled (red) and externally wetted CNT (green). The arrows indicate the HOMO (H) and LUMO (L).The insets are the cut-plane visualization of the electron density of occupied states at the middle length region of the CNT.

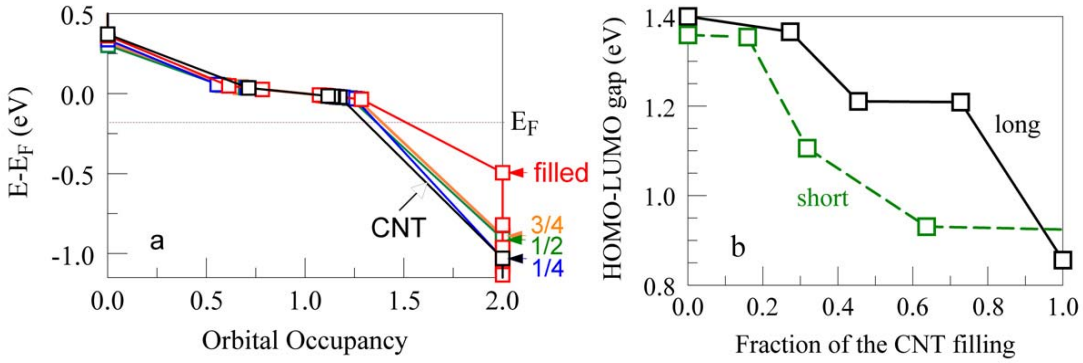

Figure 5.14 a. Energy of the CNT-water molecular orbitals as function of the orbital occupancy. The orbitals in the gap, around the Fermi energy (shifted to 0) are localized at the end of the CNT and are consequence of

the finite-cluster calculation. b. The HOMO-LUMO gap of the CNT-water system in function of the fraction of the water filling (longer tube, solid line). The gap in the shorter (10,0) CNT (length of 15.62 Å), with ordered water molecules

The dependence of the HOMO-LUMO gap in function of the water filling of the The HOMO-LUMO gap as function of the water filling of the tube is shown in Fig. 5.14b for both long (28.4 Å) and short (10, 0) CNT (15.62 Å). In the latter case, the water molecules were ordered parallel to each other, and that ordering as well as the length effects of the tubes caused difference in the curve shapes on the filling fractions at Fig. 5.14b. As seen in Fig. 5.14b, the longer tube showed slightly bigger reduction in HOMO-LUMO gap when fully filled. The effect is expected to be stronger with increase of the CNT length and its diameter, to the dimensions used in the present experiments.[122] It is also interesting that for the longer tube, the significant change of the HOMO-LUMO gap happens only when filling almost half of the tube with water. Finally, the gap was changing dominantly by shifting up the top of the valence band Figs. 5.13c and 5.14a): The bottom of the conduction band was almost unchanged.

We have also studied change of the HOMO-LUMO gap in cases of the external wetting of the (10,0) CNT tube. The obtained results were almost identical for longer and shorter CNT's. Although the number of the water molecules included in the external wetting was 115, obtained by MD simulation (see Fig. 5.13b), the change of the gap was significantly smaller than in the case of internal wetting. As can be seen in Fig. 5.15b, the gap was decreased to ~1.2 eV (from 1.4 eV of the CNT), which is less than 15% change. However, in case of

external wetting this small reduction of the gap is happening in combination of the shift down of the bottom of the conductive band and a slight shift up of the top of the valence band (red curve, Fig. 5.15b). Since the convergence of the calculations with external wetting was reached with the DFT smearing of 0.54 eV, for consistency we have also solved the electronic structure problem and density of states for the "empty" CNT (Fig. 5.15b). We also studied the cases of both internal filling and external wetting of the tube (also with 0.54 eV smearing). The geometry was obtained by MD simulation (Fig. 5.15a). As shown in Fig. 5.15b, the HOMO-LUMO gap is almost identical to the external wetting result, the main difference being in absence of the shift of the conducting band.

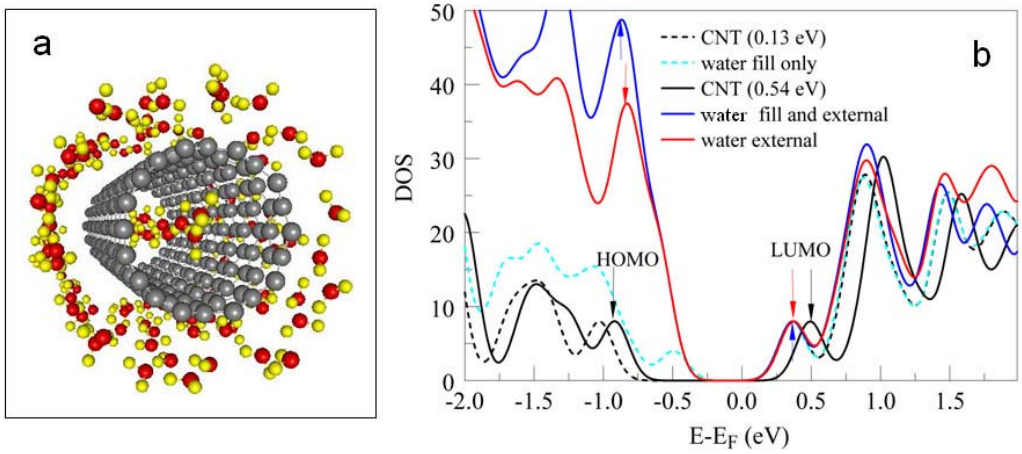

Figure 5.15 a Structure of a (10, 0) SWCNT of length 2.84 nm, filled with 11 water molecules and surrounded by 115 water molecules at the outside of the CNT. b. DOS of externally wetted (red solid line), both externally wetted and internally water filled (blue solid line), comparing with the case of only internal water filling (dashed cyan line). The DOS of dry CNT was shown here as reference, for two DFT Gaussian smearing.

5.7 Water wetting time dependence investigation

Based on these simulations, it is clear that internal wetting can modify the electronic property of device either through dipole electric-field and induced polarizations mediated modification of the Schottky barriers and/or *via* the shift of the valence band owing to the bandgap reduction. We devised an experiment to separate the effects of internal wetting on the contacts from the effects on the electronic properties of the tube itself. To do this, we opened the SWCNT at one end only, so that the internal wetting would proceed slowly, passing first one contact, then the interior of the device, and finally the second contact, measuring the current through the device as the wetting proceeded. Figure 5.16a shows a typical current vs. time trace for a device gated partially "on" initially. Interestingly, the current first *drops* and then rises to the saturated "on" value (note the current scale is logarithmic). Since, as revealed by Figure 5.14a and quantum calculations, the internal wetting has a minimal effect to the valence band when the wetting is less than 25 % of one side, and becomes really significant at more than 75% of the tube filling, this result implies that wetting *increases* the Schottky barrier at the first contact, an effect that is eventually counteracted by the upward movement of the valence band. It was shown previously that asymmetric Schottky barriers (generated by different metal contacts,[123] or an extra gate near one contact[124]) will produce rectifying behavior. We slowed down the wetting process by using a tube with a 100 μm separation between the source and drain electrodes so that we could record I_{DS} as a function of V_{DS} as wetting proceeded (the backgate was set to turn the device

"on" initially). Initially (1 in Figure 5.16b) the I_{DS}-V_{DS} curve was symmetric. However, at intermediate times (2, and 3 in Figure 5.16b) the device showed rectification, returning to a symmetric response (4 in Figure 5.16b) as both contacts became wetted.

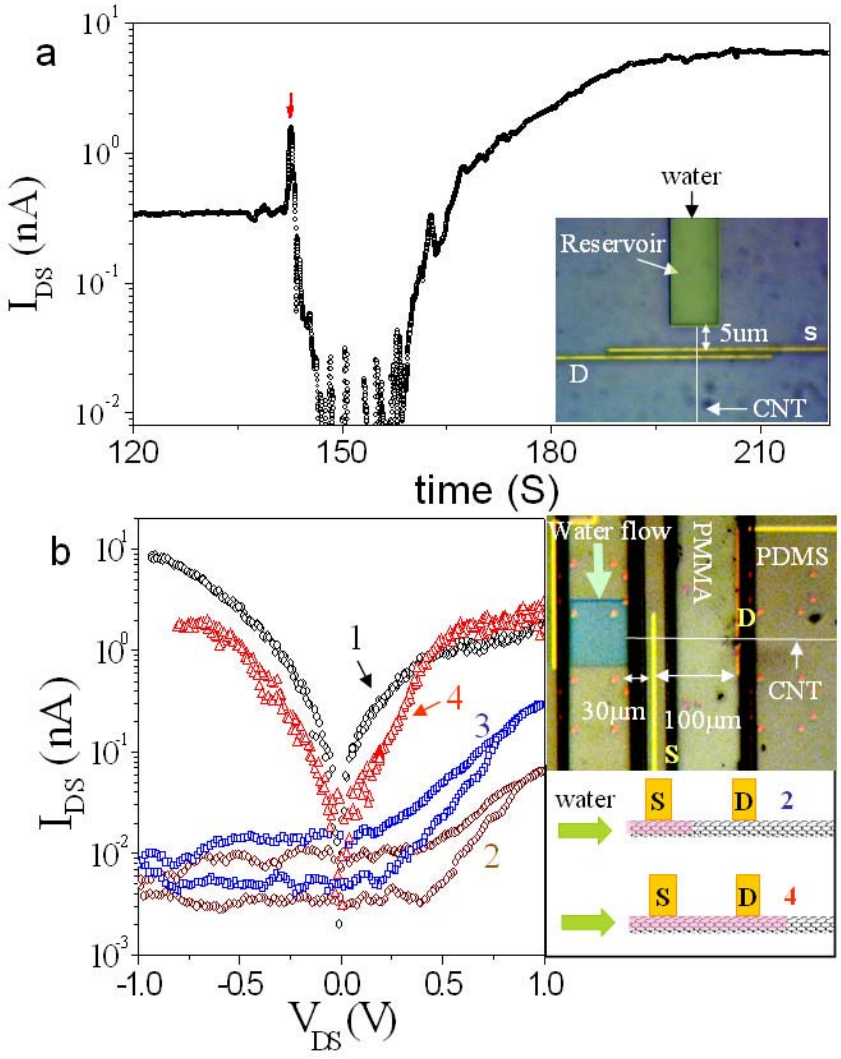

Figure 5.16. Change of electronic properties during wetting. (a) I_{DS} vs. time for V_{GS} = 20V and V_{DS} = 2V. The red arrow marks the point of water addition, with current initially falling before rising to the equilibrium value. The optical microscopy image of the single reservoir device used for this measurement is shown in the inset. (b) I_{DS}-V_{DS} curves (V_{GS}=0 V) for a slow-filling device (inset top right) showing a transition from symmetric behavior (1) to rectification (2,3) and back to symmetric

behavior (4) as the internal water propagates into the structure (inset down right).

We can qualitatively account for our observations by assuming (a) that the Schottky barriers is first increased due to the water dipole induced polarizations of the CNT and metal electrodes in particular, as predicted by the molecular dynamics simulations and (b) that the valence band is then shifted upward (narrowing the Schottky barriers) as predicted by the DFT calculations. Figure 5.17a shows the device switched "on" (blue dashed lines) at V_{GS}=0 and "off" (orange dashed lines) at V_{GS}>0 when the tube is dry. When water wets the inside of the CNT under the first contact, an increase of the Schottky barrier height (Figure 5.17b) leads to a current (I_{DS}) drop. With the further wetting of the CNT interior, the upward shift of valence band (E_V) (Figure 5.17c), lowers the Schottky barrier height, turning the device on. A significant shift in E_V and /or a large local polarization field at contacts (due to the induced image charges at electrodes from the polarized CNT) will overcome the ability of the backgate to modulate the conductance (indicated schematically by the smaller difference between the dashed orange and blue lines in Figure 5.17c and also turns the device "on" at V_{GS}>0. We often observed a similar or slightly smaller "on" conductance of the devices after water wetting, which implies a similar SB, or a large metal-CNT contact resistance.

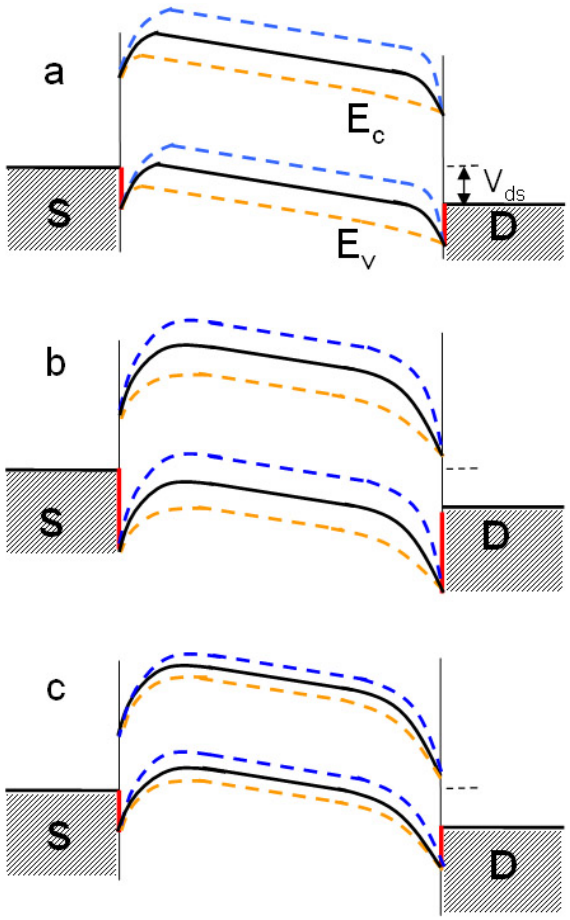

Figure 5.17 Sequential change of the energy band diagrams of a CNT-FET device during water wetting process at a fixed positive V_{DS} and different V_{GS} (orange-positive, black-zero, and blue-negative). (a) The initial diagram before wetting. (b) The increase of SB at contacts. (c) The up shift of valence band (E_V) while the CNT Fermi level is fixed. The red lines indicate the heights of Schottky barriers. S and D are source and drain electrodes respectively. In the diagrams, the contact resistance is neglected and the Fermi level between metal contact and CNT is always in alignment.

5.8 Further discussion and Methods

Internal wetting with a salt solutions (0.1 mM KCl) immediately restored p-type transistor action in tubes that had been rendered insensitive to gating by pure water (Figure 5.18). The change may be due to the disruption of the ordered water structure and the water-CNT interaction inside the CNT by the hydrated salt

ions. At 0.1 mM salt, a 15 μm long SWCNT contains approximately 3 K^+ and 3 Cl^- ions and 10^6 water molecules, so water ordering would have to be extremely sensitive to the presence of just a few ions. A second possibility is that the carbon nanotube potential needs to float with respect to the reservoirs for the abolition of gating to be observed. The addition of salt will add the capacitance of all of the electrolyte in the reservoir to that of the tube, effectively pinning the tube potential.

The effect of salt addition is shown in Figure 5.18. We studied the effect of electrolytes using tubes that had previously shown a semiconducting-to-metallic transition on wetting. When 0.1 mM KCl solution was injected into the reservoir, p-type transistor characteristics were restored with increased hysteresis. Subsequent rinsing with distilled water restored the semiconducting-to-metallic transition immediately

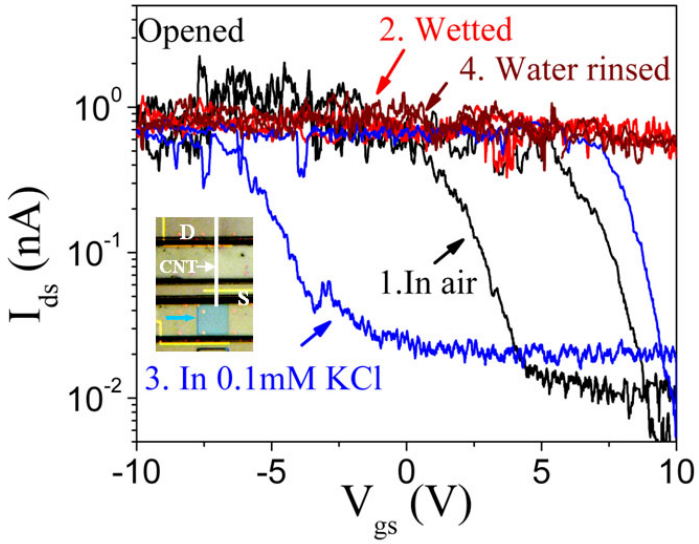

Figure 5.18. I_{ds}-V_{ds} curves of a device before (black) and after adding water (red) and 0.1 mM KCl (blue), and after flushing with water (wine).

In summary, we have studied electronic transport in individual SWCNTs as they are filled by water. The tubes are extremely sensitive to internal wetting, which affects the CNT potential and bandgap structure, owing to the nanoconfinement of water. Thus this work provides a new method to investigate water at nanoscale. Furthermore, SWCNTs are likely to be even more sensitive to internal analytes than they are to external analytes. Using the inside of the tube as the sensing surface will also permit the SWCNT to be used as a nanopore (for analyzing single molecules[1]) and as a nanoscale sample concentrator because of the ion-selectivity of SWCNTs [125, 126] and the enhanced water flow inside them.[57, 58] Analytes dissolved in water that enter the CNT slowly will accumulate owing to the several-thousand fold enhancement of water flux through the tube.

METHODS

Device fabrication. We first grew well-separated single-walled carbon nanotubes (SWCNTs) on boron-doped silicon wafers (used as a back-gate) with a 1000 nm of thermal oxide. Cobalt nanoparticles were used as catalyst and the carbon source was ethanol vapor. Conditions were chosen to produce high quality SWCNTs with an outside diameter of 1 to 2 nm.[1] Gold markers and large electrical pads were fabricated using optical lithography. SEM images were used to locate the SWCNTs position relative to the markers. After SEM imaging, the chips were heated at 400 ^{O}C in air for 1 hour to remove resist residue. Immediately after cleaning, the Au/Cr metal electrodes for contacting the SWCNTs (normally 5 μm in width and 40nm/5 nm in thickness) were fabricated

using electron beam lithography (EBL) and the electrical properties of SWCNT were measured in ambient air. SWCNTs with good electrical properties were selected for the next step. We then spun-on a 900 nm thick layer of polymethylmethacrylate (PMMA, A8) over the entire device structure, and wells were formed along the path of a SWCNT using EBL aligned relative to the markers.

Electrical measurements. The electrical measurements were carried out in a home-built probe station inside a faraday cage. A Keithley SourceMeter 2636A, a low noise current meter 6514 and a function generator (DS 345, Stanford research system) were used and controlled by custom labview programs.

Theory. The Density Functional Theory (DFT) calculations were performed with the Computational chemistry package NWChem[127] using 12000 processors at the Cray XT5 computer (Jaguar) of the National Center of Computer Sciences (NCCS), ORNL. The molecule dynamics (MD) calculations were performed at the Cray XT5 computer (Kraken) of National Institute of Computational Sciences (NICS), UT Knoxville, using computer package GROMACS.[128] Hydration geometries were determined using MD simulations on a (10, 0) carbon nanotube of various lengths (2.84 nm, 280 C-atoms, and 1.56 nm, 160 atoms), of 7.8 Å diameter, partially and fully filled with water, as well as wetted outside. Eleven water molecules filled the longer nanotube, forming a chain, while 115 water atoms wetted the CNT externally. We performed the all-electron calculations, using the 3-21g (3s2p) basis, and the GGA, nonlocal hybrid DFT exchange-correlation functional, with Gaussian smearing of 0.13 eV in case of the water

filling and of 0.54 eV for the external wetting. Full details are given in the water wetting theory section.

Chapter 6

ELECTRICAL SENSITIVITY OF SINGLE-WALLED CARBON NANOTUBE INNER SURFACE TO IONIC SOLUTIONS

Carbon nanotube (CNT) is well-known as a superb nanoelectronics material and show great potential to be used as the sensing element in chemical and biological sensors. Recently, the CNT has been demonstrated as an effective fluid conduit and the transport of substances through small diameter CNTs is intrinsically fast, selective and at single molecule level. It has been shown that the transport characteristics of semiconducting single-walled CNT (SWCNT) field effect transistor (FET) are sensitive to the internal water wetting. We report here that the characteristics of semiconducting SWCNT FET are also sensitive to the concentration, pH and ion type of ionic solution when the electrolytes are inside the CNT. Such sensitivity is not observed at the outside surface of a semiconducting SWCNT. This opens a new avenue for building new type of CNT sensor devices in which the SWCNT concurrently functions as a nanochannel and an electronic detector.

This chapter is based on paper *"Electronic sensitivity of single-walled carbon nanotube to internal electrolyte"* which is ready to submit to *Nanotechnology*. I list as the first author and finish most of the work independently.

6.1 Introduction and experiment setup

CNTs are excellent one-dimensional electronic materials with a large surface-to-volume ratio. It has been demonstrated that the electronic properties of

SWCNTs and the Schottky barriers between SWCNTs and metal contacts are very sensitive to adsorbates[129, 130] and environment,[116, 131, 132] which is the basis of many CNT field effect transistor (FET) chemical and biological sensors. In recent years, carbon nanotubes (CNT) have also been employed as nanopores or nanochannels to rapidly transport a variety of ions and molecules, both in gas and liquid phases.[1, 2, 57, 58, 103] [133] It is appealing to integrate the nanoelectronic and nanofluidic advantages of SWCNT into one device. Such integration will enable electrical probing of the activities confined in extremely samll space *in situ* and in real time. The high electronic sensitivity of CNT to charged ions and molecules in proximity can be readily utilized to study the dynamics of ion and molecule translocation process in sub 2nm channels, which has not been studied experimentally. In addition, this investigation may lead to a new type of CNT sensor with ultrasensitivity. We have built a combined CNT-nanopore- FET device. The internal wetting of the semiconducting SWCNT by pure water significantly modifies the FET characteristics.[1, 25] In contrast, the external wetting has little effect. Theoretical simulations revealed that internal water both generates a large dipole electric field, causing charge polarization of the tube and contacting metal electrodes, and shifts the valance band of the SWCNT. External water has little effect because external water molecules are random oriented and the interactions between external water molecules and CNT outside surface are weaker. Recent experimental work has used such sensitivity to probe the average speed of water molecules when moving inside a semiconducting SWCNT.[133] In this report, we examined the electrical response

of SWCNT when its interior was exposed to aqueous solution with various ion concentrations, pH and ion species. High sensitivity was observed for semiconducting SWCNT FET only when the internal surface of SWCNT was exposed to electrolytes. This is a continuation of previous water wetting work and one step closer to the goal of a functional nano-electrofluidic device. There is a recent trend to develop conductive synthetic nanopores, which are capable in controlling the electrostatic environment of the pore for biomolecule manipulation and enriching electrical sensing methods.[134] The conductive nanopores have been made by either metallization of insulating pore[135, 136] or directly using conductive materials, such as graphene.[137-139] The current work on conductive CNT nanopore will contribute significantly to the research in this area.

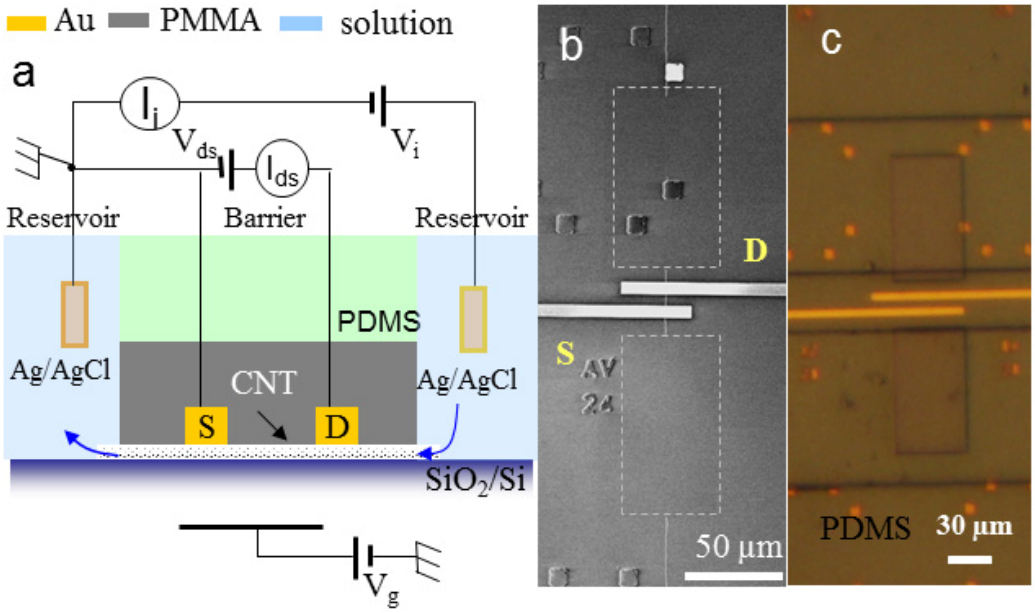

Figure 6.1. (a) Schematic of the device structure of a combined SWCNT field effect transistor and nanopore device. The electrical measurement configuration for both electronic current and ionic current measurement is also shown. The distances between source (S) and drain (D) electrodes is 15µm and the barrier width is 30µm. (b) Scanning electron microscope (SEM) image of a used device after stripping off the covered PMMA layer. The two rectangles enclosed by white dash lines indicate the

location of reservoirs. In the barrier region, one SWCNT bridges two reservoirs and is also contacted by both the source and drain electrodes. (c) Optical microscope image of a working device during measurement. The device is covered by a PDMS stamp with microfluidic channels and aqueous solution fills the reservoirs.

The device structure and experiment setup are illustrated in Figure 6.1. The device fabrication has been described in details in previous chapters.[1, 25] Briefly, long SWCNTs with average outer diameter of 1.7nm were grown by chemical vapor deposition method on a highly doped silicon substrate with 1μm thick SiO_2 top layer. Source and drain electrodes (gold) were fabricated by electron-beam lithography (EBL) to directly contact one SWCNT under the PMMA barrier (20-40μm in width) and the heavily doped silicon substrate acting as a back gate. SWCNTs were determined as semiconducting or metallic based on measurements of source-drain current (I_{ds}) versus backgate voltage (V_{gs}), which were measured by a Keithley 2636A (Keithley Instruments, Inc., Ohio). A clean PDMS stamp with imbedded microfluidic channels sealed the surface of the CNT chip to deliver electrolytes (Figure 6.1a and c) into CNT. An Axon 200B (Molecular Devices, Inc., CA) in voltage clamp mode was used to measure the ionic current between two reservoirs (bridging by only one SWCNT) using Ag/AgCl electrodes (MF-2078, BAS, 2M KCl). All the electrical measurements were carried out on a home-built probe station inside a Faraday cage.

6.2 The KCl concentration dependence of electronic and ionic current

We have fabricated 11 functional devices, in which 8 have semiconducting SWCNTs and 3 have metallic SWCNTs. All the devices made

from metallic SWCNTs display negligible changes in I_{ds}-V_{gs} curves compared with the devices with semiconducting SWCNT (see section 6.5). For controls, we always examine the working devices prior to open the CNT by oxygen plasma; we also prepare control devices with a section of SWCNT between source and drain electrodes exposing to various electrolytes (Figure 6.8&6.9). None of these controls alter the transport characteristics of the SWCNT FET significantly. After removing the exposed CNT in the reservoirs (see Figure 6.1b) and opening the ends of CNT by oxygen plasma, 6 devices made with semiconducting SWCNTs showed the same trend of variation in $I_{ds}V_{gs}$ curves when exposing to electrolytes with various concentration, pH and ion species. In the following paragraphs, we mainly discuss the results from these devices.

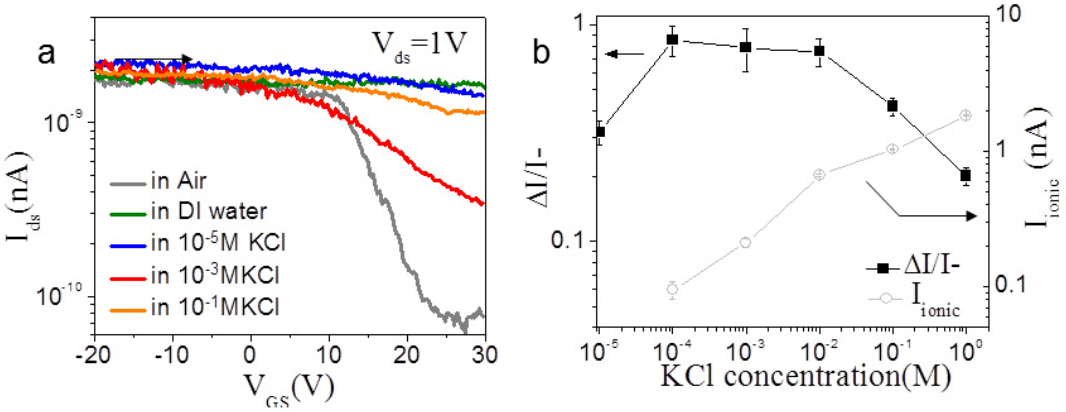

Figure 6.2. The dependence of electronic and ionic current on KCl concentration. (a) Typical I_{ds}-V_{gs} semilog curves of a working device with opened semiconducting-SWCNT before (gray) and after adding DI water (green), $1x10^{-5}$ M KCl (blue), $1x10^{-3}$M KCl (red) and 0.1M KCl (orange).The V_{ds} is 1V. (b) Gate efficiency ΔI/I- vs. KCl concentration (black). The ionic current (gray) at V_{ionic}=0.5V and at different KCl concentration is also shown here for comparison.

We first measured $I_{ds}V_{gs}$ curves of SWCNT FET devices in KCl solution with different concentrations and typical results are shown in Figure 6.2a. The

curves have hysteresis and only sweep down curves are shown. The electronic transport measurement in air (grey curve) suggested the FET was p-type, which is "on" at negative gate voltage and "off" at positive gate voltage. After adding DI-water, gating is almost abolished and SWCNT becomes insensitive to the back gate, keeping constant for the entire range of V_{gs} (green curve also see chapter 5).[25] We then studied the response of the SWCNT FET when KCl solutions with different concentrations were injected into the reservoirs sequentially in an order from low to high concentration. The $I_{ds}V_{gs}$ curves changed correspondingly with KCl concentration but the change was not monotonic. With the increase of KCl concentration from $1x10^{-5}$M to 1M, the I_{ds} at positive gate bias (e.g., at 10V) initially decreases, restoring the p-type behavior, and then increases again. The current at negative gate bias (saturation current) didn't change much for all the KCl solutions. To better display the results, we defined gating efficiency, which is $\Delta I/I$.. Here, $\Delta I = I_+ - I-$, where I_+ is the maximum current at positive gate voltage and I- is the maximum current at negative gate voltage. The plot of $\Delta I/I-$ vs. KCl concentration is shown in Figure 6.2b. The gating efficiency ratio is the biggest at around 0.1mM. However, the "off" current is still higher than the data in air at this point. When the KCl concentration is further increased, the gating efficiency decreases. Corresponding controls did not show this level of sensitivity. These results confirmed that the inner surface of semiconducting-SWCNT is electrically sensitive to ions. At low salt concentration, the presence of ions likely disrupted the ordered structure of water inside the CNT and suppressed the interaction between water and the inner surface of SWCNT. So we observed the increase of

gating efficiency until reaching a higher ionic concentration, such as10^{-4}M. At high salt concentration, the gate voltage possibly was strongly screened by the ionic solution inside the CNT and thus the gating efficiency was significantly reduced.

6.3 The pH dependence of electronic and ionic current

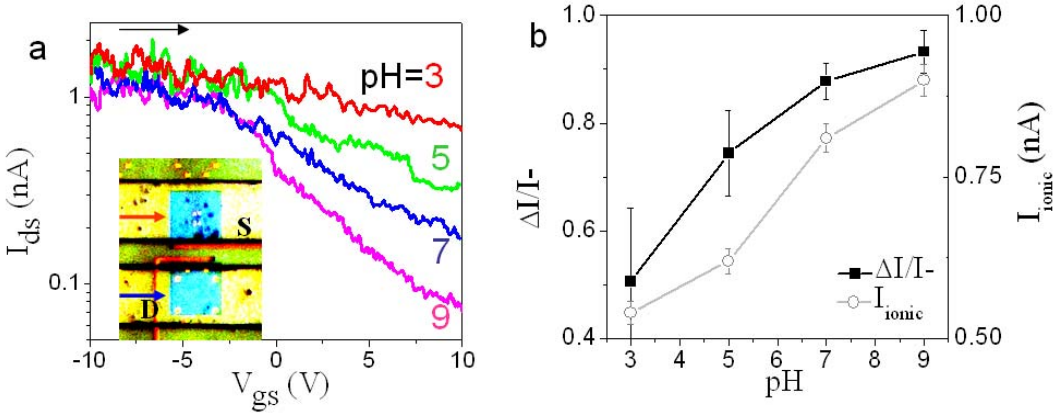

Figure 6.3. pH dependence of the working device containing open ends semiconducting-SWCNT. (a) Typical I_{ds}-V_{gs} semilog curves for a device filling sequentially with pH=3 (red), pH=5 (green), pH=7 (blue) and pH=9 (magenta) 1mM KCl solution at Vds=0.5V. The inset shows an optical image of a device sealed with a PDMS cover with microfluidc channels (green). The two blue squares (i.e., 60 μm x 60 μm) are the fluid reservoirs cut into the PMMA (yellow). (b) Gate efficiency ΔI/I- for different pH (black solid squares). The measured ionic current at different pH was shown (gray open circles). The concentration of the KCl solution is 1mM and V_{ionic}= 0.5V.

We further studied the response of the electrical transport characteristics of the SWCNT FET when exposing to ionic solutions with different pH values. Figure 6.3a shows $I_{ds}V_{gs}$ curves for a semiconducting SWCNT FET when the reservoirs were filled with 1mM KCl solutions at various pH values from 3 to 9. The I_{ds} at positive gate voltage (i.e., 10V) increases significantly at low pH while the I_{ds} at negative gate voltage is relatively constant. KCl solution at higher

concentration such as 1M was also tested and the pH sensitivity was much lower. The pH dependence of the electrical transport characteristics is also reflected in the gating efficiency ΔI/I- vs. pH plots (Figure 6.3b). The biggest gating efficiency appears at pH 9, where I_{ds+} is the lowest. No conclusive conclusions are drawn in literatures for the pH sensitivity of CNT exterior surface, implying the pH response is sensitive to the variation of CNT, device geometry and environment. Recent studies report an obvious sensitivity to solution pH with the SWCNT conductance increasing steadily with pH (when pH>7) using a liquid-gated FET configuration.[140, 141] This response is opposite to that of the opened SWCNT FET, suggesting different mechanisms for pH sensitivity between opened and unopened SWCNT FET. The pH sensitivity for unopened SWCNT is attributed to the adsorption of hydroxyl groups to the external surface of SWCNT or the ionization of silanol groups on SiO_2 surface near the SWCNT. In our control experiments (section 6.5), the exterior surface of CNT didn't show any sensitivity, differing significantly from the opened CNT. In order to better understand the pH sensitivity of opened SWCNT, we also measured the ionic current through CNT in 1mM KCl solution at different pH (Figure 6.3b). The ionic current increases with the increase of pH, which is consistent with previous results and is attributed to the ion selection of carboxyl groups at CNT ends.[1] Considering both the I_{ds} and ionic conductance data, we propose one possible explanation. At low KCl concentration, proton and potassium ions are the major ions inside the CNT at pH 3 and 9 respectively. At pH 3, proton conduction can happen following a "hop-and-turn" Grottuss mechanism along the well-ordered

water chain inside CNT. In this scenario, the FET gating efficiency is suppressed by internal water chain due to water-CNT interior interaction.[25] At pH 9, the excess potassium ions likely disrupt the water-CNT interaction more frequently and restore the gating efficiency. This hypothesis is supported by the fact that the pH sensitivity almost disappeared at high KCl concentration (e.g., 1M Figure 6.4), prohibiting proton conduction. It is also worth to note that the opposite trend between I_{ds} and ionic current excludes the possibilities of a short circuit between drain and source electrodes caused by interior conductive ionic solution.

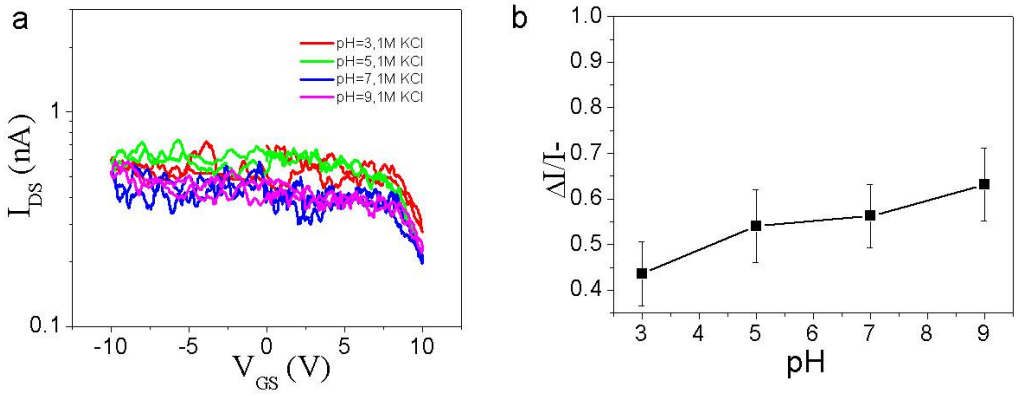

Figure 6.4. (a) pH chage at high KCl concentration (1M), Typical I_{ds}-V_{gs} semilog curves for a device filling sequentially with pH=3 (red), pH=5 (green), pH=7 (blue) and pH=9 (magenta), the sensitivity is lower, the structure is the same as main text (b) Gate efficiency ΔI/I- for different pH (black solid squares). The concentration of the KCl solution is 1M and V_{ds}= 0.1V.

Previously we demonstrated the change of I_{ds}-V_{gs} by pH at low KCl concentration (0.1mM KCl). The changes at high KCl concentration were also measured. From Fig. 6.4 we can see almost the same trend, but much lower sensitivity. This is combined responds of pH with KCl concentration curve. At

high concentration, the Gate efficiency is much lower. This is also exhibited in the pH measurement.

6.4 Dependence of electronic and ionic current on cation

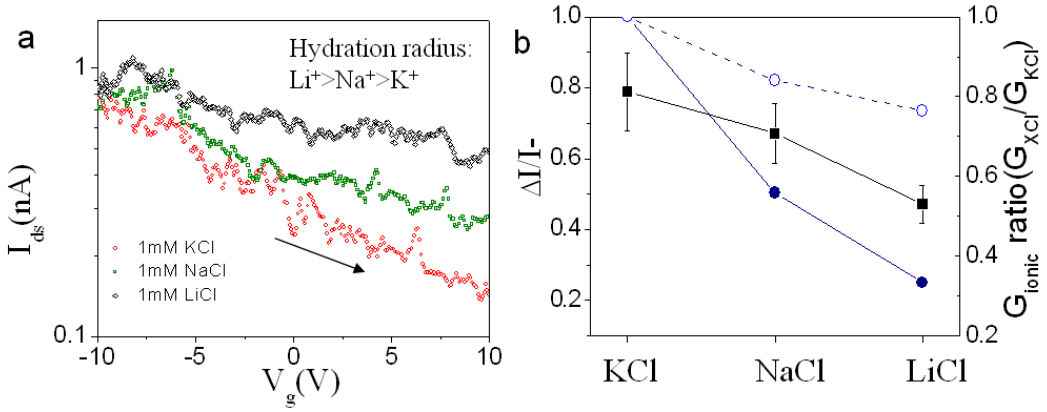

Figure 6.5. The electrical response of open ends semiconducting-SWCNT to different cations. (a) Typical I_{ds} vs. V_{gs} curves when the opened SWCNT was exposed to 1mM KCl (red), NaCl (green) and LiCl (black) solutions respectively at V_{gs}=1V. (b) Gate efficiency ΔI/I- (black square) and ionic conductance ratio (normalized with G_{KCl}) (blue solid circle) in three different 1mM ionic solutions for the same SWCNT device are shown. The ionic conductance ratios in PDMS micron size channels are also displayed for comparison (blue open circles).

We also studied the electrical sensitivity of the opened semiconducting-SWCNT to chloride electrolytes with three different cations, K^+, Na^+ and Li^+. The typical concentration of the solution is 1mM for better sensitivity. The electrolytes are freshly prepared and no buffer is added to make the electrolytes as simple as possible. As shown in Figure 6.5a, the highest I_{ds+} is observed for the electrolyte containing K^+, which has the largest atomic size but the smallest hydration shell out of the three cations. The gating efficiencies ΔI /I- in various 1mM chloride electrolytes are also illustrated in Figure 6.5b. The biggest gating efficiency is in KCl solution. These results may confirm that the interaction between water

molecules and CNT inner surface is more critical in determining I_{ds+}. Potassium ion likely has bigger impact on disturbing the water-CNT interaction due to bigger atomic size. We also measured the ionic current through the opened SWCNT. For comparison, the ionic current only through the PDMS microfluidic channels (minimum width > 10μm) was measured and the conductance values were close to the bulk solution data. As shown in Figure 6.5b, the ionic conductance in both SWCNT nano channel and PDMS micron channel varied in the sequence $G_{KCl}>G_{NaCl}>G_{LiCl}$. However, the ionic conductance of LiCl solution is about 0.8 of KCl solution in micro channels and drops to about 0.3 in SWCNT nano channels. The difference suggests the potassium ions are more readily translocated through the SWCNT, attributing to its smaller hydration size. The ratio of G_{LiCl}/G_{KCl} varied from 0.3 to 0.6 for different SWCNT devices. The variation presumably rises from the fluctuation of SWCNT diameters. Our results are also consistent with the observation of substantial ion selection in sub 2nm CNT.[60] The origin of ion selection has been confirmed as the steric exclusion by the small CNT diameter and the electrostatic rejection by the carboxyl groups at CNT ends.[60]

6.5 Metallic CNT, time dependence and control experiment

The electrical response of metallic SWCNT to electrolytes is shown in Fig. 6.6. The experiment structure and the procedure is the same as the semiconducting CNT, change for KCl concentration and pH, almost no change of I_{ds}-V_{gs} was detected (the source-drain conductance (gray) in Fig. 6.6 b and d). There are some small changes based on solutions but no larger than 2%.

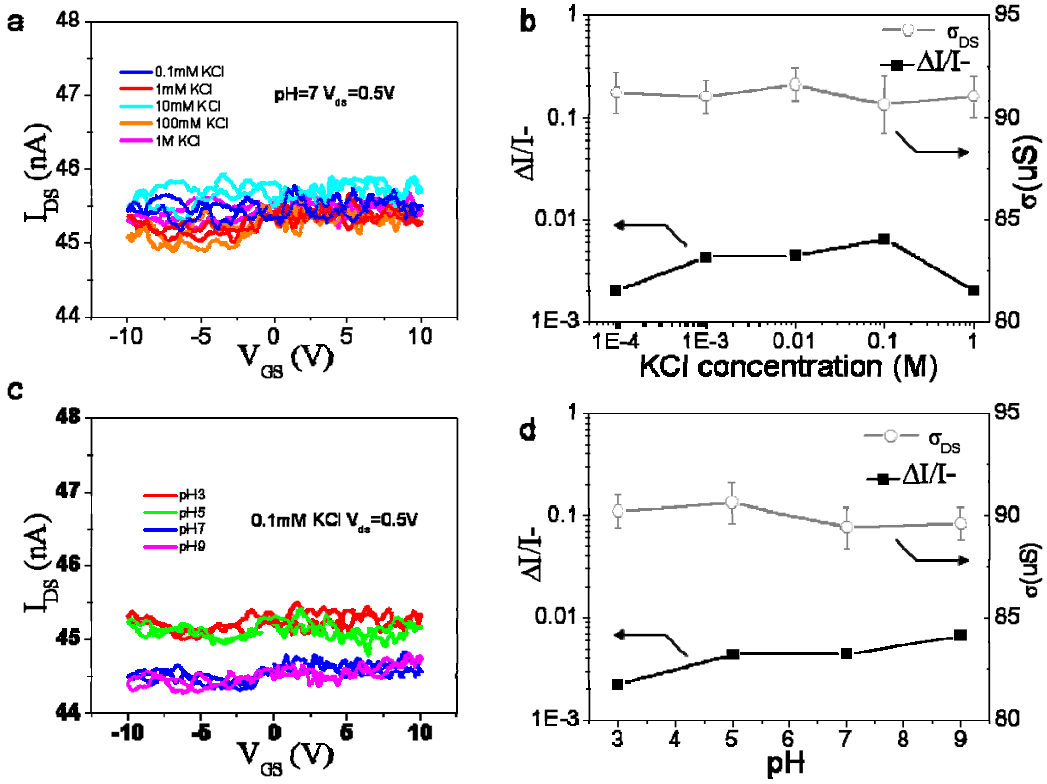

Figure 6.6. KCl concentration and pH dependence of the device containing opened metallic-SWCNT. (a) Typical I_{ds}-V_{gs} curves with metallic CNT device for 0.1mM KCl (blue), 1mM KCl (red), 10mM KCl (cyan), 0.1M KCl (orange), and 1M KCl (magenta). (b) Gate efficiency ΔI/I- vs. KCl concentration semilog curve (black). The source-drain conductance (gray), G(V_{gs} =5V) vs. KCl concentration semilog curve is also shown here for comparison (c) Typical I_{ds}-V_{gs} curves with metallic CNT device for with pH=3 (red), pH=5 (green), pH=7 (blue) and pH=9 (magenta) 0.1mMKCl solution (d) Gate efficiency ΔI/I- vs. pH semilog curve (black). The source-drain conductance (gray), G(V_{gs} =5V) vs. pH semilog curve is also shown here for comparison, the structure is the same as main text, all V_{ds}=0.5V

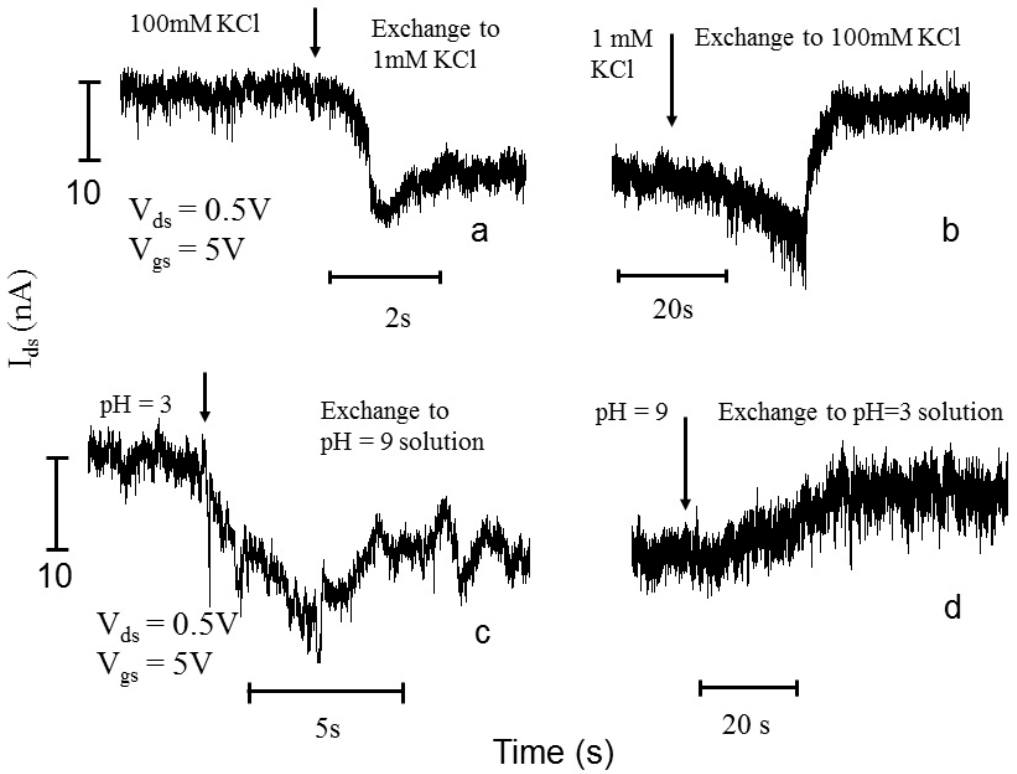

Figure 6.7. The electrical response of an open ends semiconducting-SWCNT to different concentration and pH KCl solutions. (a) and (b) I_{ds} *vs.* t traces when the opened SWCNT was exposed to 100 mM and 1mM KCl solutions sequentially at V_{ds}=0.5V and V_{gs}=5V. The pH is always 7. (c) and (d) I_{ds} vs. t traces when the opened SWCNT was exposed to pH=3 and pH=9 solutions sequentially at V_{ds}=0.5V and V_{gs}=5V. The KCl concentration is fixed at 100mM. The arrows indicate the starting points of solution exchange by syringes.

Finally, we studied the electrical response with time. As shown in Figure 6.7, the device can response to the *in situ* exchange of concentration (Fig. 6.7 a and b) and pH (Fig.6.7 c and d) of the KCl solutions in the reservoirs. The response is reversible. Due to the microfluidic channel design, it normally takes several seconds to exchange the solution in the reservoirs. During the solution exchange, the electrical current I_{ds} is often affected by mechanical vibrations. Therefore, we cannot acquire the accurate response time of the device. However,

we consistently observe that the device responses quicker when the conductivity of SWCNT is changed from high to low, for both concentration and pH.

The control device structure is shown in the optical image. The first reservoir is opened as the structure in the main text that takes measurement (Fig 6.8). The second reservoir is opened between source and drain electrodes, and the heart part of SWCNT-FET is exposed to electrolytes (Fig 6.9). The device is not treated with oxygen plasma, so CNT between source-drain is unopened. After adding different KCl concentration, pH, different cation solution, none of them change the electrical response of CNT-FET, compared to the results of opened CNT.

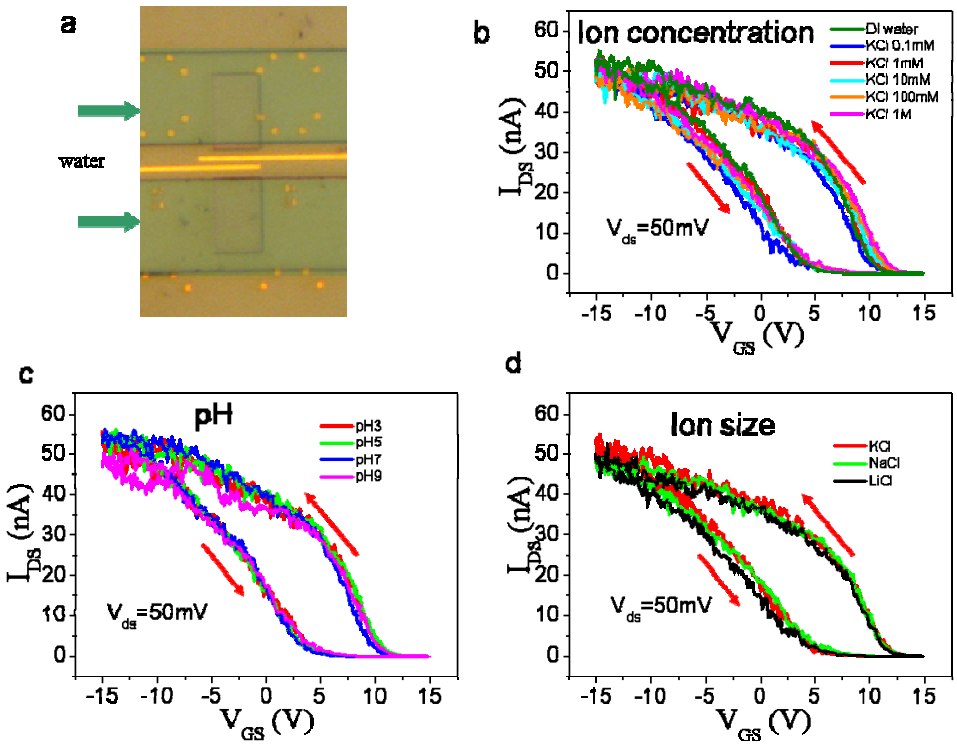

Figure 6.8. (a) Optical images for control experiment, the structure is the same as main text (b) KCl concentration for unopened CNT, typical I_{ds}-V_{ds} curves of a device for after adding DI water (green), 0.1mM KCl (blue), 1mM

KCl (red), 10mM KCl (cyan), 0.1M KCl (orange), and 1M KCl (magenta). (c) pH for unopened CNT, Typical I_{ds}-V_{gs} curves for a device adding sequentially with pH=3 (red), pH=5 (green), pH=7 (blue) and pH=9 (magenta) 0.1mMKCl solution (d) Typical I_{ds} vs. V_{gs} curves when adding 1mM KCl (red), NaCl (green) and LiCl (black), all the V_{ds} is 50mV, no obvious changes detected for the control.

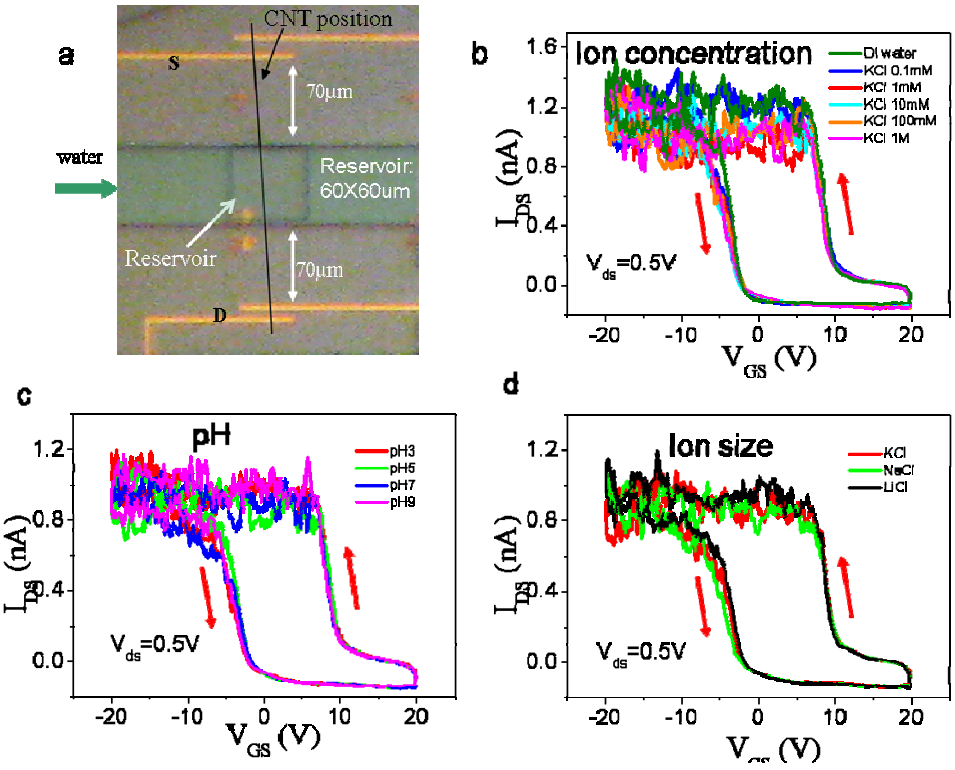

Figure 6.9. (a) Optical images for control experiment, structure is reservoir opened between electrodes (b) KCl concentration for unopened CNT, typical I_{ds}-V_{gs} curves of a device for after adding DI water (green), 0.1mM KCl (blue), 1mM KCl (red), 10mM KCl (cyan), 0.1M KCl (orange), and 1M KCl (magenta). (c) pH for unopened CNT, Typical I_{ds}-V_{gs} curves for a device adding sequentially with pH=3 (red), pH=5 (green), pH=7 (blue) and pH=9 (magenta) 0.1mMKCl solution (d) Typical I_{ds} vs. V_{gs} curves when adding 1mM KCl (red), NaCl (green) and LiCl (black), all the V_{ds} is 0.5V, no obvious changes detected for the control.

Our experiments demonstrated that the electronic properties of semiconducting SWCNTs are highly sensitive to the variations of ionic flow

inside the SWCNT. This will be important for developing a fundamental understand of the dynamics of ion and molecule tansport through sub-2nm conductive nanopore and nanochannel and the induced polarization effect inside the conductive nanopore. In addition, the results reported here is one step further towards building new type of nano-electrofluidic devices and platforms for biomolecule manipulation and detection. Using the same device structure, the electronic sensitivity to small charged (bio) molecules will be studied in the next step. Single molecule sensitivity is expected.

6.6 The detail of fabrication and device structure

The single-walled carbon nanotube (SWCNT) field effect transistor (FET) was fabricated on the heavily doped p-type silicon substrate with 1000nm of thermal oxide. SWCNT were grown by chemical vapor deposition method with cobalt nanoparticles as catalyst; then 10:1 argon to hydrogen gases bubbled from ethanol bring vapor though the furnace. The temperature of the furnace is 950°C~1000°C adjust result to long SWCNTs with outside diameter around 1.7nm. Gold markers and large pads were fabricated by photolithograph to locate a single SWCNT and SEM images show the actual position. Then chip was cleaned in the furnace 400°C with argon for around 1 hour. Source-drain electrodes (5nm Cr and then 40nm Au with width 2~5um) were fabricated by electron beam lithography (EBL) directly contacts the SWCNT. The back gate electrode was added to the silicon substrate and the FET electrical properties were measured. Then a 900 nm thick layer of polymethylmethacrylate (PMMA, A8)

was span on the chip and 2 reservoirs were opened on the located CNT using EBL with alignment, leaving source drain electrode between them. The electrolyte is diluted from standard solution which is 1M KCl with 1mM PBS buffer, so 0.1M solution is 1:9 volume ratio of standard solution to water, etc. The measurement was performed in faraday cage. A Keithley SourceMeter 2636A, a Keithley low noise current meter 6514 and self-brought software are used to collect the electrical current. The ionic current was measured by Ag/AgCl electrodes in the solution. Data was collected by Axon CNS Axopatch 200B with noise filter Digidata 1440A.

Chapter 7

SNS QUANTUM RIBBON FIELD-EFFECT TRANSISTORS

From Chapter 2 to Chapter 6, we discuss the measurement based on carbon nanotube devices. In this chapter, I present other nanostructures. Quantum ribbon project is to construct FET with tin sulfide (SnS) quantum ribbon. Properties of this new semiconducting material are measured. This project is collaborating with Hao Yan's group in Biodesign Institute.

In this part we report orthorhombic single crystalline SnS nanoribbons grown from zinc-blende SnS nanospheres, achieved by nanoscale control of the metastable-to-stable phase transition. Novel, dual phase SnS intermediate heterostructures with nanosphere-heads and nanoribbon-tails were observed. Field-effect transistors (FET) fabricated using the SnS nanoribbons exhibit a typical p-type semiconductor behavior. This work demonstrates a new approach to control the growth of single crystalline nanostructures.

This chapter is based on the paper *"Colloidal IV-VI SnS Nanoribbons Formed via Phase Transitions and Exchanged with Inorganic Ligands to Improve the Performance of Single Nanoribbon Based Field Effect Transistors"* which is submitted to *Angewandte Chemie-International Edition*. I list as the coauthor and finish field-effect transistor fabrication and electrical properties related measurements and calculations.

7.1 Synthesis of SnS nanoribbons

Main-group IV-VI (IV = Ge, Sn, Pb; VI = S, Se, Te) nanomaterial compounds have received significant attention recently due to their narrow band gap, strong quantum size effects, and rich electronic, optical, and photonic properties.[142-144] Among these, tin sulfide (SnS) is inexpensive, naturally abundant, environmentally-benign, and heavy-metal-free (i.e., free from Cd, Pb, and Hg). Bulk orthorhombic-phase SnS crystals have been reported to have a narrow bandgap in the near infrared region.[145-147] Theoretical calculations indicate that SnS possesses all the qualities required for efficient absorption of solar energy, suitable for incorporation into clean energy conversion cells and a variety of other optoelectronic devices.[145, 148] Their useful properties, e.g., photovoltaic, photoconducting, photocatalytic and Peltier effect, make them promising candidates for diverse applications such as solar energy conversion, thermoelectric cooling, thermoelectric power generation, and near-infrared photo-electronics.[146]

Transitions from the metastable to stable phase are important in the field of crystal growth and engineering, which encourages the discovery of novel and practical reactions to synthesize new semiconductor materials.[149, 150] Recently, synthesis of either metastable[145] zinc-blende phase or stable[151-153] orthorhombic SnS nanostructures has been performed. However, the exact mechanism of the zinc-blende phase to orthorhombic phase transition is still largely unknown. As a result, the development of novel phase-transition based

techniques to control the growth of single crystalline nanostructures has been hampered.

Herein, we demonstrate that by tuning the metastable-to-stable phase transition process, orthorhombic single crystalline SnS nanoribbons can be synthesized from zinc-blende SnS nanospheres. Novel, dual phase intermediate SnS heterostructures with nanosphere-heads and nanoribbon-tails were observed and thoroughly characterized. The first field-effect transistors (FET) based on individual single crystalline SnS nanoribbons were fabricated by taking advantage of the highly-controlled large scale synthesis of one-dimensional nanoribbon structures, which are relatively easy to access, control, and process.

The synthetic scheme employed here is based on our previously reported phosphine-free colloidal method for synthesizing II-VI quantum rods and wires.[154] The resulting single-crystalline SnS nanoribbons are ~ 2-5 μm long and ~150-500 nm wide, with thicknesses of ~10 nm. Their formation occurs by a simple colloidal process, initiated by the injection of a sulfur-oleylamine precursor into a hot tin-oleylamine solution in the presence of hexamethyldisilazane (HMDS). During the synthesis, sequential aliquots of the reaction mixture were removed and purified to monitor the kinetics of nanoribbon formation. As shown in figure 7.1, single crystalline SnS nanoribbons formed through a unique transition from the metastable zinc-blende phase to the stable orthorhombic phase.

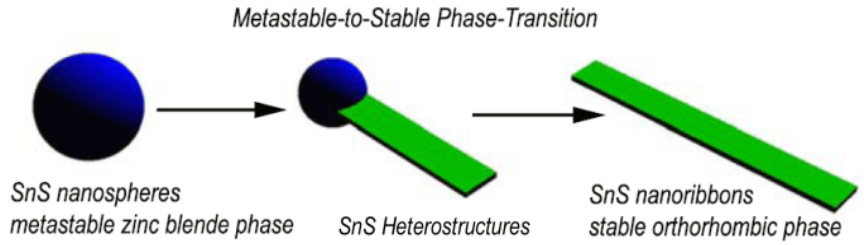

Figure 7.1. Schematic illustration of the growth of a single crystalline SnS nanoribbon via a unique metastable to stable phase transition.

15 minutes after initial injection of the sulfur-oleylamine precursor into the 250 °C tin solution, a black SnS product was observed. The solid product was purified and imaged by transmission electron microscopy (TEM). Nanospheres with an average diameter of ~ 280 nm were obtained (Figure 7.2A). High resolution TEM (HRTEM) images of the edge of the nanospheres reveal a two dimensional lattice with typical spacing of 0.21 nm, which corresponds to the distance between {220} facets of the cubic zinc blende SnS (with a crystal constant of a=0.5845 nm).[145] The X-ray diffraction (XRD) pattern (Figure 7.3A, black trace) indicates that the SnS nanospheres are zinc-blende phase with trace amounts (<5%) of orthorhombic phase present.

After 10 additional minutes at an elevated reaction temperature (330 °C), the zinc blende nanospheres are spontaneously converted to the orthorhombic phase. Intermediate SnS heterostructures with nanosphere-heads and nanoribbon-tails were observed (Figure 7.2B-D). High resolution TEM (HRTEM) images (Figure 7.2E) reveal that the "head" area of the heterostructure consists of a two-dimensional (2D) lattice with a typical spacing of 0.21 nm, which corresponds to the distance between {220} facets of zinc-blende SnS (with a crystal constant of

a=0.5845 nm). The indexed fast Fourier transform (FFT) of a HRTEM image (inset in Figure 7.2E) reveals a typical hexagonal pattern, indicating the SnS nanosphere "head" is single-crystalline zinc blende phase projected along the <111> direction. In contrast, a HRTEM image of the "tail" section of the heterostructure (Figure 7.2F) shows a 2D lattice with typical spacing of 0.29 nm, which corresponds to the distance between {101} facets of the orthorhombic phase of SnS (with a crystal constant of *a*=0.4329 nm, *b*=1.1192 nm, *c*=0.3894 nm, JCPDS Card No. 39-0354). The indexed FFT of this HRTEM image (inset in Figure 7.2F) reveals a typical rhombic pattern, indicating that the SnS nanoribbon is single-crystalline orthorhombic phase projected along the <010> direction. These results clearly indentify the unique, dual-phase property of the intermediate heterostructures. Further characterization of the intermediate product by XRD (Figure 7.3A, red trace) confirms a mixture of zinc-blende and orthorhombic SnS phases with a ~ 4:6 ratio.

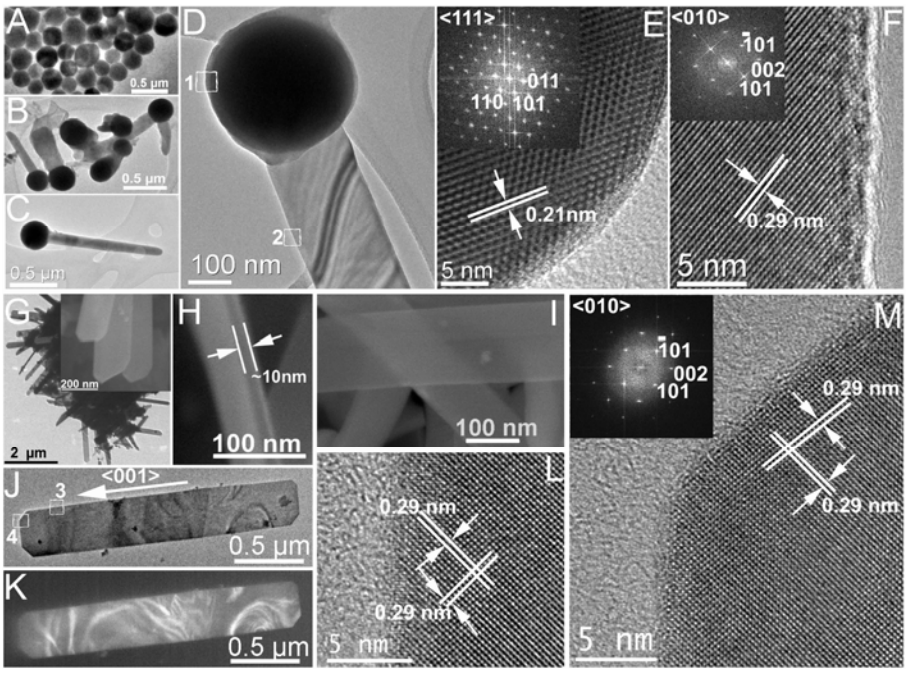

Figure 7.2. (**A**) TEM image of the initial zinc blende SnS nanospheres; (**B-D**) TEM images of the intermediate product, dual-phase heterostructures, each containing a nanosphere head and a nanoribbon tail; (**E, F**) HRTEM images of the head and tail sections corresponding to the boxes marked "1" and "2" in (**D**); (Inset in **E&F**) The indexed FFTs of the images in **E&F**; (**G**). TEM image of the final orthorhombic SnS nanoribbons; (Inset in **G, H & I**) SEM images of the final SnS nanoribbons; (**J, K**) Bright field and dark field TEM images of a typical nanoribbon; (**L, M**) HRTEM images of the end and long edge corresponding to the boxes marked "3" and "4" in **J,** respectively; (Inset **M**) indexed FFT of image **M**.

After 30 minutes at 330 ^{o}C, all the metastable zinc-blende SnS nanospheres are transformed to stable orthorhombic SnS nanoribbons, as shown in the TEM and scanning electron microscopy (SEM) images in Figures 7.2G-K. The XRD pattern of the final product (Figure 7.3A, blue trace), reveals highly pure orthorhombic phase SnS with no zinc-blende phase detected. The elemental composition of the nanoribbons was established using energy-dispersive X-ray spectroscopy (EDS). Only Sn and S peaks, with a 1:1 atomic ratio, were observed, indicating the

formation of pure SnS product. Typical nanoribbons are 2~5 μm long, 150 to 500 nm wide and ~10 nm thick. A simple mass calculation was executed to follow the transition from zinc-blende nanospheres to orthorhombic nanoribbons. The mass of a single SnS nanosphere (initial stage of the reaction) and a single SnS nanoribbon (final product) are nearly identical, which also supports the proposed transformation of a single SnS nanosphere to a single SnS nanoribbon.

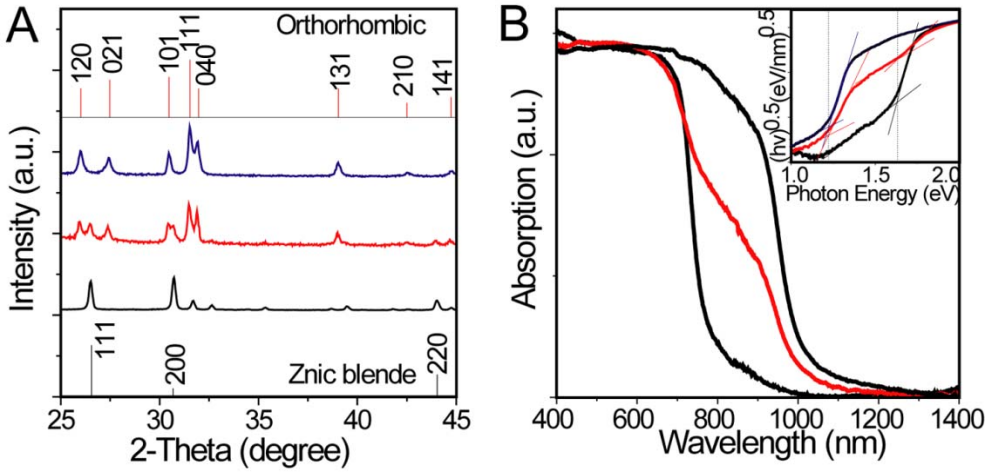

Figure 7.3. (**A**) Powder XRD pattern of the initial SnS nanospheres (black trace), the intermediate SnS heterostructures (red trace), and the final SnS nanoribbons (blue trace). The red vertical bars along the top are indexes of the orthorhombic phase of SnS crystals according to JCPDS card No. 39-0354. The black vertical bars along the bottom are the indexes of the cubic phase of SnS crystals according to literature[145]; (**B**) UV−Vis-NIR absorption spectra and (inset B) plots of $(ahv)^{0.5}$ versus photon energy (hv) of the initial SnS nanospheres (black trace), the intermediate SnS heterostructures (red trace), and the final SnS nanoribbons (blue trace). The spectra were recorded from powder samples drop cast at room temperature on a glass slide using an integrating sphere.

Bright field and corresponding dark field TEM images of a typical nanoribbon (Figure 7.2J&K) reveal that the nanoribbons are single crystalline. HRTEM analysis (Figure 7.2L&M) of both the end and edge of the nanoribbon showed the

same 2D lattice composition with a spacing of 0.29 nm, which corresponds to the distance between {101} facets of the orthorhombic phase of SnS. The indexed FFT of the HRTEM image (inset in Figure 7.2M) reveals a rhombic pattern, confirming that the SnS nanoribbon is single-crystalline in the orthorhombic phase. These analysis reveal that the long edge of the nanoribbon is in the [001] direction with the terminating facets {001} at the ends, {100} along the sides and {010} on the faces.

7.2 Electrical transport properties of SnS nanoribbons

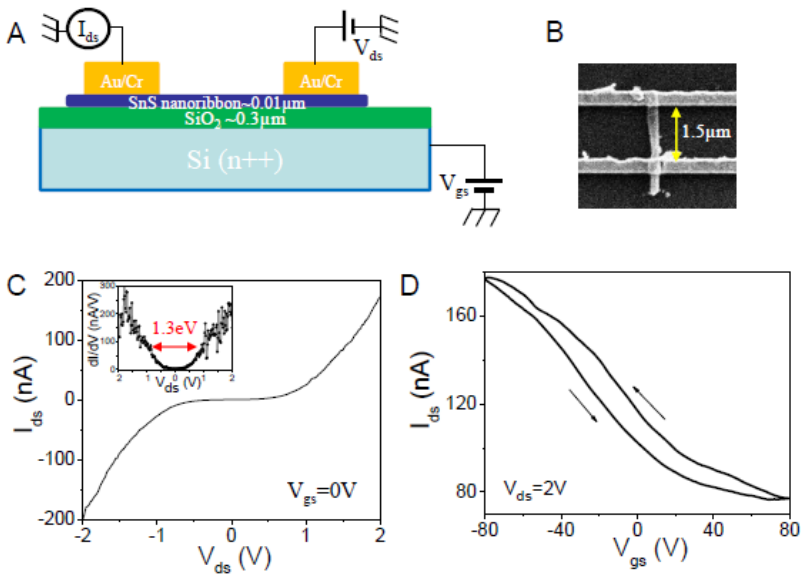

Figure 7.4. (**A**) Schematic illustration the structure and dimensions of a SnS single nanoribbon based field effect transistor device; (**B**) SEM image of a typical device. The distance between two electrodes is 1.5 μm and the width of the ribbon is about 200 nm; (**C**) I_{ds} vs. V_{ds} curve of a typical SnS single nanoribbon FET device (see image B) measured at V_{gs} = 0V. Inset shows the derivative of the I-V curve and the band gap energy is measured to be 1.3 eV; (**D**) I_{ds} vs. V_{gs} at V_{ds} = 2.0 V, exhibiting typical p-type semiconductor behavior.

The electrical transport properties of individual SnS nanoribbons were also studied in ambient conditions using a back- gated field-effect transistor (FET) configuration as shown in Figure 7.4A. Single nanoribbons were positioned on top of a highly doped n-type Si chip with a 300 nm thick SiO_2 dielectric layer between the chip and nanostructure. The details of device fabrication are given later. An SEM image of a typical nanodevice is shown in Figure 7.4B. The electrodes are composed of Cr (30 nm) and Au (120 nm), where Cr has a work function of 4.50 eV, close to that of orthorhombic SnS (4.2 eV). Curves of source–drain current (I_{ds}) vs. source–drain voltage (V_{ds}) at different gate voltages (V_{gs}) were measured, and a typical $I_{ds}V_{ds}$ curve at $V_{gs} = 0$ is shown in Figure 7.4C. A zero current region is visible at low voltage bias, suggesting the existence of an energy gap. The band gap of the SnS nanoribbon was determined to be 1.3 eV from the dI_{ds}/dV_{ds} vs. V_{gs} curve (inset in Fig. 7.4C), which matches the value obtained from the optical absorption study.

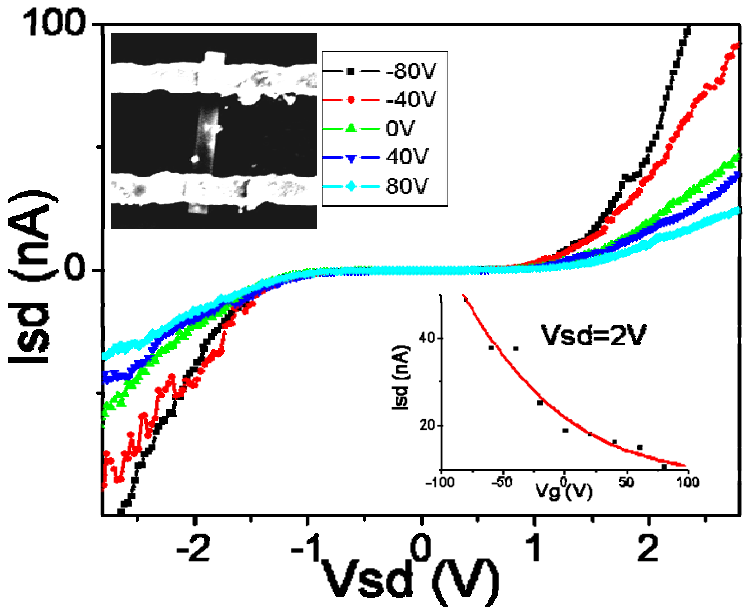

Figure 7.5 Electron transport characteristics of single SnS quantum ribbon. I_{sd}-V_{ds} plots at different Vgs from -80V to 80V. The insert plots of SEM image and I_{ds} vs. V_{gs} at V_{ds} = 2V.

Figure 7.4D and Figure 7.5 contains plots of I_{ds} vs. V_{gs} at V_{ds} = 2V for two devices. The SnS nanoribbon based FETs behave as p-type semiconductors. A small hysteresis was observed, likely originating from the water present in air or contaminations that were incorporated during the fabrication process. The trans-conductance $g_m(=dI_{ds}/dV_{gs})$ was acquired by fitting the linear region of the $I_{ds}V_{gs}$ curve. With knowledge of the backgate area capacitance and geometry of nanoribbons (Figures 7.4A, B), the hole mobility was calculated to be 0.3 $cm^2 V^{-1}s^{-1}$ and the hole carrier concentration was estimated to be 6×10^{18} cm^{-3} (see calculation details later). FET measurements were repeated on more than 10 devices fabricated with the as-synthesized nanoribbons. Reproducible results were obtained, and the derived carrier mobilities were all in the range of 0.3 to 1.1 cm^2

$V^{-1}s^{-1}$. It should be noted the hole mobility of our SnS nanoribbon FET device is comparable to the best known solution-processed organic and nanocrystal devices so far.[155, 156] Also, it is comparable to other IV-VI PbS and PbTe nanowire FET devices, where the nanowires are synthesized by the chemical vapor transport (CVT) method.[157] In addition, as suggested by Talapin et al.,[158] when an organic ligand is exchanged with an inorganic chalcogenide ligand, the electron transport in arrays of colloidal nanocrystals will increase by an order of magnitude. It is reasonable to expect that the carrier mobility of our SnS nanoribbon device could be further improved through a similar process.

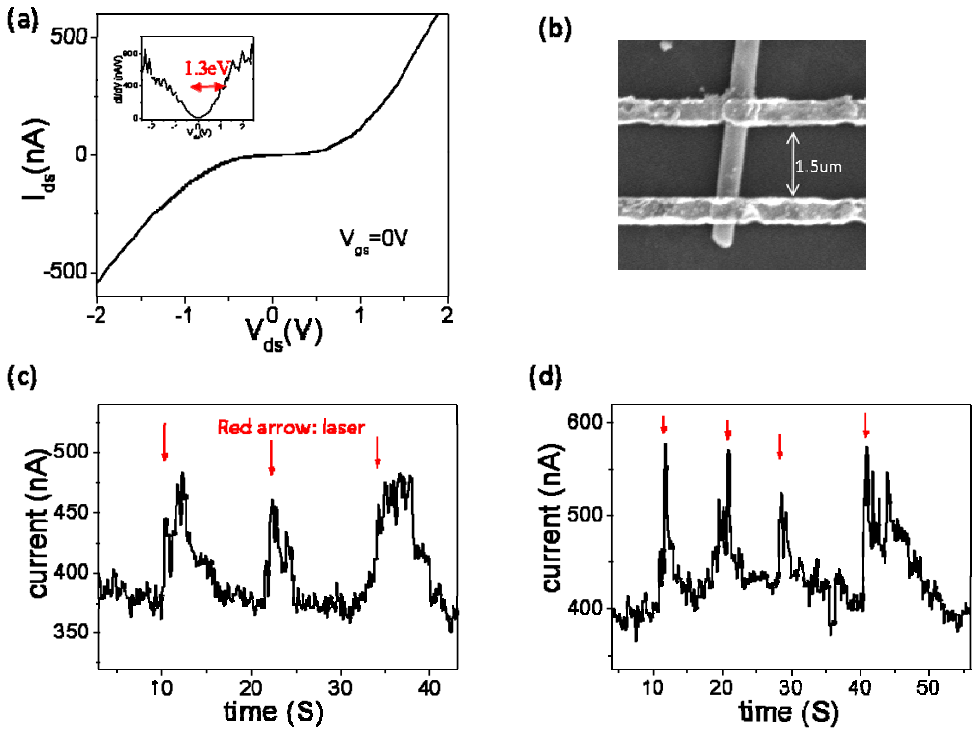

Figure 7.6 photocurrent response of the same single nanoribbon based field effect transistor device shown as (a),(b) with 532 nm laser intensity on the channel of the field effect transistor device calculated to be 0.07 nW.

To assess the suitability of the SnS nanoribbons as optically active centers for their incorporation into optoelectronic devices, we also measured the opto-electronic response of the FET device shown in Figure 7.6d, under conditions of illumination using a green laser (λ = 532 nm or 2.33 eV; 1.3 mW), which is greater than the calculated bandgap from optical and electronic measurements. As can be seen from Figure 7.6, upon illumination of the channel of the SnS FET device with laser intensity of 0.07 nW, the current is observed to quickly increase during the illumination and upon switching off the laser the current returns to its preillumination value. This photocurrent response profile is reproducible over many cycles, suggesting the potential application of the single SnS nanoribbon as highly sensitive photodetectors, as well as the widely used PbS based photodetectors in industry.

7.3 FET device fabrication and mobility calculation

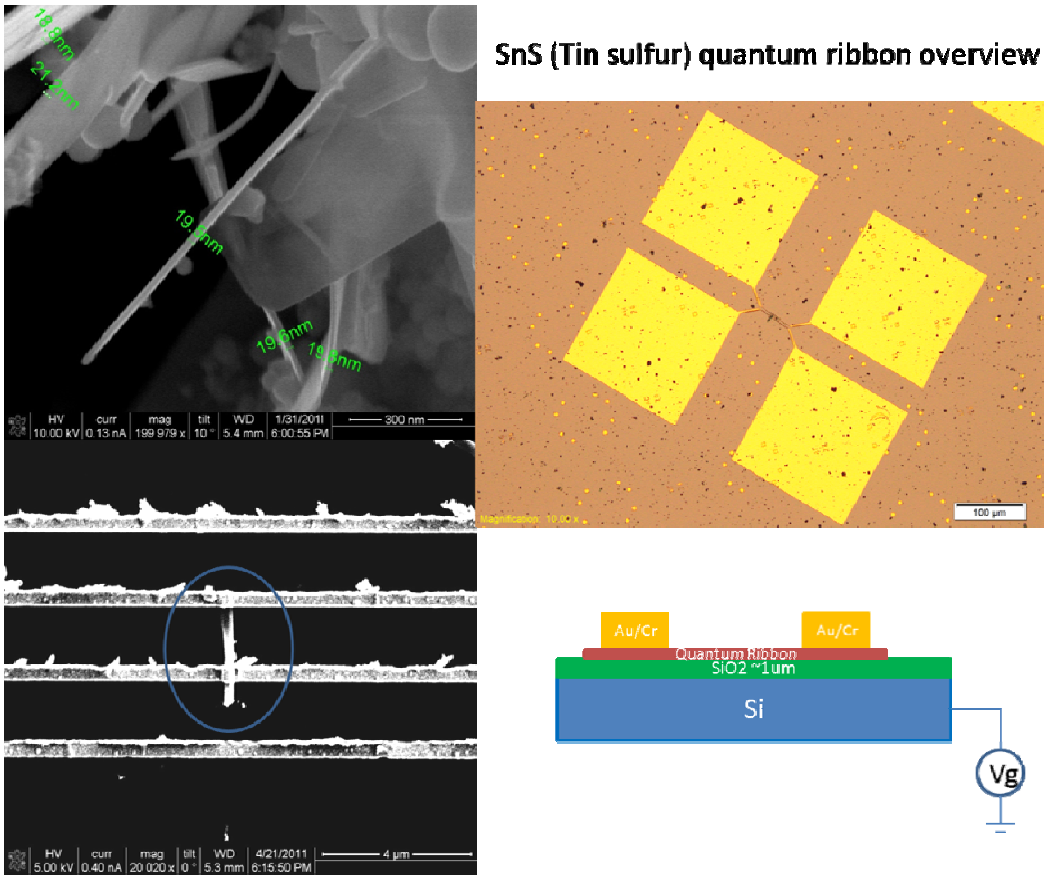

Figure7.7 FET device fabrication, including SEM images before and after adding electrodes, schematic and optical image of the electrodes.

FET device fabrication and mobility calculation: Metal (Au) markers for position registration were first fabricated by electron beam lithography (EBL) on n-type silicon substrates with 300nm thermal dioxide. The SnS nanoribbons were dispersed in DI-water and transferred to the substrates by a pipette. The nanoribbons remained on the SiO_2 surface after water evaporation. After determining the position of each nanoribbon by SEM with the aid of metal markers, source-drain electrodes (30nm Cr and 120nm Au) were fabricated by

EBL. The electrical measurements were conducted with a Keithley 2636A in a faraday cage. We followed a common method in literature to extract the carrier mobility from the electrical transport measurement. The transconductance ($g_m=dI_{ds}/dV_{gs}$) was obtained from the slope by fitting the linear region of the $I_{ds}V_{gs}$ curve (Figure 7.4d). The mobility was calculated by $\mu = \frac{g_m L}{C_g V_{ds} W}$, where C_g is the backgate capacitance per unit channel area, W and L is the width and length of the channel (nanoribbion) as determined from the SEM images.

$$Cox = \frac{\varepsilon_0 \varepsilon_R}{T} = \frac{8.85\times10^{-12}\times3.9}{0.3\times10^{-6}} = 115.05\times10^{-6}\ \mathrm{F/m^2} \tag{7.1}$$

$$\mu = \frac{slope\times L}{Cox\times V_{ds}\times W} = \frac{1.23\times10^{-9}\times1.5\times10^{-6}}{115.05\times10^{-6}\times2\times0.21\times10^{-6}} = 0.382 cm^2/Vs \tag{7.2}$$

Here C_g is mainly from the 300nm SiO_2 layer and therefore $C_g=1.15\text{x}10^{-4}\mathrm{F/m^2}$. The obtained mobility ranged from 0.256 to $1.1 cm^2/VS$ over 6 devices. The carrier concentration is calculated by $n_h = \sigma / e\mu_h$ at the current saturation region of the $I_{ds}V_{gs}$ curve for a p-type semiconductor.

$$n_h = \frac{\sigma}{e\mu_h} = \frac{0.357\Omega^{-1}cm^{-1}}{1.6\times10^{-19}C\times0.382cm^2/Vs} = 5.8\times10^{18}cm^{-3} \tag{7.3}$$

We estimated the hole concentration to be $5.8\times10^{18}cm^{-3}$ using the conductivity value at V_{gs}=-80V in Figure 7.4d.

In summary, we present the synthesis of the single crystalline SnS nanoribbons through a unique metastable zinc blende phase to stable orthorhombic phase transition. This phase transition process from meta-stable to

stable crystal is important in the field of crystal growth and engineering, which can be extended to other crystal growth system. Field effect transport properties of single SnS nanoribbons FET devices demonstrate p-type semiconductor characteristics with good gating dependence at small bias voltages. Much awaits to be explored on the applicability of solution processed IV-VI semiconductor nanostructures as nanoscale devices.

Chapter 8

FUTURE DIRECTIONS FOR NANOFABRICATION

This thesis comprised several experiments using CNT nanofludic devices. After presenting the significant applications in our project, there are still lots of limitation in this kind of field. The major uncontrollable part is the properties of the carbon nanotube when in growth, especially the diameter and the chirality. Under current conditions, the parameters to determine the diameter and the chirality are still unclear. But there is a hint to control the diameter in the near future. (see Ref. [159]) The inner diameter is the key factor when a carbon nanotube is used as a nanofludic channel. Precision control will pave the way for mass production of carbon nanotube devices. While the chirality can be selected from Raman spectra [31], the electrical prosperities, such as semiconducting or metallic is expected to be distinguished by a much simpler method. In addition to its extraordinary thermal and mechanical properties, carbon nanotube has great potential in application in the future.

In Chapter 4, we present the translocation of DNA through single wall nanotube. The next step is the sequencing of the DNA by embedded the base-reader into the CNT nanofludic device. Shuai Chang in Lindsay's group reported that single molecules in a tunnel junction can be interrogated reliably using chemically-functionalized electrodes. Functionalizing a pair of electrodes with recognition reagents can generate a distinct tunneling signal when an analyte molecule is trapped in the gap [160]. This gives the possibility for applying carbon nanotube

nanofludic device for rapid sequencing of single DNA molecules. The next generation DNA sequencing is possible to realize that sequence a diploid mammalian genome for around $1000 in 24 hours.

In a wide variety of industry, the whole "nanoscience" is promoted faster and faster. In the late 1980s, the term *microsystems* become common referring to the integration of sensors, actuators and signal-processing electronic on a common substrate.[161] This field is summarized as Micro-Electro-Mechanical systems (MEMS), combines knowledge from many disciplines and give rise to a new type of engineer described as *miniaturization engineering*. Chapter 5 & 6 give the basis for building sensors in CNT nanofludic devices. This application will extends micromachining into the submicron range, redefined as nanomachining, also Nano-Electro-Mechanical systems (NEMS) [32]. The nanotechnology will push the advanced IC fabrication methods into extreme and give impetus to new techniques such as nanochemistry. It's also expected that Biomimetics will go to nanometers and inspired us more by nature itself.

The CNT-FET changes the transistors from traditional two dimensions to one dimensional material. A similar change, from two dimensional surface micromachining to vertical, three dimensional, is going to happen. Intel just announced one of its most significant technology improvements that using 3D Tri-Gate transistors in its 22nm processors in 2011.[162] All these changes diversify the options of new transistor technology, which help to sustain the Moore's law –double the number of transistors in the same area in two years – continue effective in this decade.

Furthermore, in the modeling of microstructure, the Finite Element Analysis (FEA) software such as ABAQUS and COMSOL become mature. These programs integrated principles of materials, mechanics, electromagnetic and fluidic so that people could understand and predict the actual behavior in design. The fabrication techniques and modeling analysis method assist each other to make the design simpler and faster.

In general, there will still be remarkable progresses in nanoscience. As the physicist Richard Feynman described in proposing Microsystem forty years ago, “there is plenty of room at the bottom!”[163] It will continue give us impression in the future.

REFERENCES

1. Liu, H., et al., *Translocation of Single-Stranded DNA Through Single-Walled Carbon Nanotubes.* Science, 2010. **327**(5961): p. 64-67.

2. He, J., et al., *Translocation events in a single-walled carbon nanotube.* Journal of Physics-Condensed Matter, 2010. **22**(45).

3. Tang, J., *Encoding Molecular-Wire Formation Within Nanoscale Sockets and Mass Transport in Single Wall Carbon Nanotube.* Thesis for Doctor of Philosophy in Columbia University, 2008.

4. Iijima, S., *Helical Microtubules of Graphitic Carbon.* Nature, 1991. **354**(6348): p. 56-58.

5. Donev, L., *Carbon Nanotube Transistors: Capacitance Measurements, Localized Damage, And Use As Gold Scaffolding.* Theses and Dissertations at Cornell University, 2009.

6. Saito, R., G. Dresselhaus, and M.S. Dresselhaus, *Physical properties of carbon nanotubes*1998: Imperal College Press.

7. Dresselhaus, M.S., Dresselhaus, G., Avouris, Ph. , *Carbon Nanotubes-Synthesis, Structure, Properties, and Applications; Topics in Applied Physics* Vol. 80. 2001: Springer.

8. Charlier, J.-C., X. Blase, and S. Roche, *Electronic and transport properties of nanotubes.* Reviews of Modern Physics, 2007. **79**(2): p. 677.

9. Zheng, L.X., et al., *Ultralong single-wall carbon nanotubes.* Nat Mater, 2004. **3**(10): p. 673-676.

10. Dresselhaus, M.S., G. Dresselhaus, and A. Jorio, *Unusual properties and structure of carbonnanotubes.* Annual Review of Materials Research, 2004. **34**: p. 247-278.

11. Reich, S., et al., *Tight-binding description of graphene.* Physical Review B, 2002. **66**(3): p. 035412.

12. Saito, R., et al., *Electronic structure of chiral graphene tubules.* Appl. Phys. Lett., 1992. **60**: p. 2204-2206.

13. Garaj, S., et al., *Graphene as a subnanometre trans-electrode membrane.* Nature, 2010. **467**(7312): p. 190-193.

14. Pourfath, M., *Numerical Study of Quantum Transport in Carbon Nanotube Based Transistors* Dissertation in TU Wien, 2007.

15. Odom, T.W., *Atomic structure and electronic properties of single-walled carbon nanotubes.* Nature, 1998. **391**: p. 62-64.

16. Wilder, J.W.G., et al., *Electronic structure of atomically resolved carbon nanotubes.* Nature, 1998. **391**(6662): p. 59-62.

17. *Optical properties of carbon nanotubes.* Wikipedia. **http://en.wikipedia.org/wiki/Optical_properties_of_carbon_nanotubes** .

18. Javey, A., et al., *Carbon Nanotube Field-Effect Transistors with Integrated Ohmic Contacts and High-k Gate Dielectrics.* Nano Letters, 2004. **4**(3): p. 447-450.

19. Tans, S.J., *Individual single-wall carbon nanotubes as quantum wires.* Nature, 1997. **386**: p. 474-477.

20. Bockrath, M., et al., *Single-Electron Transport in Ropes of Carbon Nanotubes.* Science, 1997. **275**(5308): p. 1922-1925.

21. Yao, Z., C.L. Kane, and C. Dekker, *High-Field Electrical Transport in Single-Wall Carbon Nanotubes.* Physical Review Letters, 2000. **84**(13): p. 2941.

22. Martel, R., et al., *Single- and multi-wall carbon nanotube field-effect transistors.* Applied Physics Letters, 1998. **73**(17): p. 2447-2449.

23. Rosenblatt, S., *Pushing the limits of carbon nanotube transistors.* Thesis (Ph.D.)--Cornell University, 2006.

24. Tans, S.J., A.R.M. Verschueren, and C. Dekker, *Room-temperature transistor based on a single carbon nanotube.* Nature, 1998. **393**(6680): p. 49-52.

25. Cao, D., et al., *Electronic sensitivity of carbon nanotubes to internal water wetting.* ACS Nano, 2011. **5**(4): p. 3113-3119.

26. Huang, L., et al., *Long and Oriented Single-Walled Carbon Nanotubes Grown by Ethanol Chemical Vapor Deposition.* The Journal of Physical Chemistry B, 2004. **108**(42): p. 16451-16456.

27. Kong, J., A.M. Cassell, and H. Dai, *Chemical vapor deposition of methane for single-walled carbon nanotubes.* Chemical Physics Letters, 1998. **292**(4-6): p. 567-574.

28. Sreekar, B. and et al., *Block-copolymer assisted synthesis of arrays of metal nanoparticles and their catalytic activities for the growth of SWNTs.* Nanotechnology, 2006. **17**(20): p. 5080.

29. Sreekar, B., et al., *Block-copolymer assisted synthesis of arrays of metal nanoparticles and their catalytic activities for the growth of SWNTs.* Nanotechnology, 2006(20): p. 5080.

30. Huang, L., et al., *Long and Oriented Single-Walled Carbon Nanotubes Grown by Ethanol Chemical Vapor Deposition.* J. Phys. Chem. B, 2004. **108**(42): p. 16451-16456.

31. Jorio, A., et al., *Structural (n, m) Determination of Isolated Single-Wall Carbon Nanotubes by Resonant Raman Scattering.* Physical Review Letters, 2001. **86**(6): p. 1118.

32. Madou, M.J., *Fundamentals of microfabrication: the science of miniaturization.* CRC Press 2002.

33. Sheats, J.R., *Microlithography Science and Technology.* CRC, 1998.

34. Andrew, M.C. and et al., *Characterization of interconnects used in PDMS microfluidic systems.* Journal of Micromechanics and Microengineering, 2005. **15**(5): p. 928.

35. Huang, S., et al., *Identification of the Structures of Superlong Oriented Single-Walled Carbon Nanotube Arrays by Electrodeposition of Metal and Raman Spectroscopy.* Journal of the American Chemical Society, 2008. **130**(36): p. 11860-11861.

36. Kim, W., et al., *Hysteresis Caused by Water Molecules in Carbon Nanotube Field-Effect Transistors.* Nano Letters, 2003. **3**(2): p. 193-198.

37. Krapf, D., et al., *Fabrication and characterization of nanopore-based electrodes with radii down to 2 nm.* Nano Letters, 2006. **6**(1): p. 105-109.

38. Howorka, S. and Z. Siwy, *Nanopore analytics: sensing of single molecules.* Chemical Society Reviews, 2009. **38**(8): p. 2360-2384.

39. Kasianowicz, J., et al., *Characterization of individual polynucleotide molecules using a membrane channel.* Proceedings of the National

Academy of Sciences of the United States of America, 1996. **93**(24): p. 13770-13773.

40. Kasianowicz, J.J., et al., *Simultaneous multianalyte detection with a nanometer-scale pore.* Analytical Chemistry, 2001. **73**(10): p. 2268-2272.

41. Kasianowicz, J.J., et al., *Applications for DNA transport in a single nanopore.* Biophysical Journal, 2001. **80**(1): p. 1418.

42. Branton, D., et al., *The potential and challenges of nanopore sequencing.* Nature Biotechnology, 2008. **26**(10): p. 1146-1153.

43. Mattia, D. and Y. Gogotsi, *Review: static and dynamic behavior of liquids inside carbon nanotubes.* Microfluidics and Nanofluidics, 2008. **5**(3): p. 289-305.

44. Schoch, R.B., J. Han, and P. Renaud, *Transport phenomena in nanofluidics.* Reviews of Modern Physics, 2008. **80**(3): p. 839.

45. Noy, A., et al., *Nanofluidics in carbon nanotubes.* Nano Today, 2007. **2**(6): p. 22-29.

46. Whitby, M. and N. Quirke, *Fluid flow in carbon nanotubes and nanopipes.* Nat Nano, 2007. **2**(2): p. 87-94.

47. Hummer, G., J.C. Rasaiah, and J.P. Noworyta, *Water conduction through the hydrophobic channel of a carbon nanotube.* Nature, 2001. **414**(6860): p. 188-190.

48. Wei, C. and D. Srivastava, *Theory of Transport of Long Polymer Molecules through Carbon Nanotube Channels.* Physical Review Letters, 2003. **91**(23): p. 235901.

49. Yinghong, X., et al., *Electric field-induced translocation of single-stranded DNA through a polarized carbon nanotube membrane.* The Journal of Chemical Physics, 2007. **127**(22): p. 225101.

50. Yeh, I.-C. and G. Hummer, *Nucleic acid transport through carbon nanotube membranes.* Proceedings of the National Academy of Sciences of the United States of America, 2004. **101**(33): p. 12177-12182.

51. Gao, H., et al., *Spontaneous Insertion of DNA Oligonucleotides into Carbon Nanotubes.* Nano Letters, 2003. **3**(4): p. 471-473.

52. Chen, M., et al., *Outer membrane protein G: Engineering a quiet pore for biosensing.* Proceedings of the National Academy of Sciences of the United States of America, 2008. **105**(17): p. 6272-6277.

53. Maniwa, Y., et al., *Water-filled single-wall carbon nanotubes as molecular nanovalves.* Nat Mater, 2007. **6**(2): p. 135-141.

54. Byl, O., et al., *Unusual Hydrogen Bonding in Water-Filled Carbon Nanotubes.* J. Am. Chem. Soc., 2006. **128**(37): p. 12090-12097.

55. Naguib, N., et al., *Observation of Water Confined in Nanometer Channels of Closed Carbon Nanotubes.* Nano Letters, 2004. **4**(11): p. 2237-2243.

56. Rossi, M.P., et al., *Environmental Scanning Electron Microscopy Study of Water in Carbon Nanopipes.* Nano Letters, 2004. **4**(5): p. 989-993.

57. Hinds, B.J., et al., *Aligned Multiwalled Carbon Nanotube Membranes.* Science, 2004. **303**(5654): p. 62-65.

58. Holt, J.K., et al., *Fast mass transport through sub-2-nanometer carbon nanotubes.* Science, 2006. **312**(5776): p. 1034-1037.

59. Majumder, M., N. Chopra, and B.J. Hinds, *Effect of Tip Functionalization on Transport through Vertically Oriented Carbon Nanotube Membranes.* Journal of the American Chemical Society, 2005. **127**(25): p. 9062-9070.

60. Fornasiero, F., et al., *Ion exclusion by sub-2-nm carbon nanotube pores.* Proceedings of the National Academy of Sciences, 2008. **105**(45): p. 17250-17255.

61. Corry, B., *Designing Carbon Nanotube Membranes for Efficient Water Desalination.* The Journal of Physical Chemistry B, 2007. **112**(5): p. 1427-1434.

62. Sun, L. and R.M. Crooks, *Single Carbon Nanotube Membranes: A Well-Defined Model for Studying Mass Transport through Nanoporous Materials.* Journal of the American Chemical Society, 2000. **122**(49): p. 12340-12345.

63. Shashank, S., et al., *Induction and measurement of minute flow rates through nanopipes.* Physics of Fluids, 2007. **19**(1): p. 013603.

64. Liang, X. and S.Y. Chou, *Nanogap Detector Inside Nanofluidic Channel for Fast Real-Time Label-Free DNA Analysis.* Nano Letters, 2008. **8**(5): p. 1472-1476.

65. Fan, R., et al., *DNA Translocation in Inorganic Nanotubes.* Nano Letters, 2005. **5**(9): p. 1633-1637.

66. Li, J., et al., *Ion-beam sculpting at nanometre length scales.* Nature, 2001. **412**(6843): p. 166-169.

67. Johnson, R.R., A.T.C. Johnson, and M.L. Klein, *Probing the Structure of DNA-carbon Nanotube Hybrids with Molecular Dynamics.* Nano Letters, 2007. **8**(1): p. 69-75.

68. Gowtham, S., et al., *Physisorption of nucleobases on graphene: Density-functional calculations.* Physical Review B, 2007. **76**(3): p. 033401.

69. Robert, R.J., A.T.C. Johnson, and L.K. Michael, *The Nature of DNA-Base-Carbon-Nanotube Interactions.* Small. **6**(1): p. 31-34.

70. Manohar, S., et al., *Peeling Single-Stranded DNA from Graphite Surface to Determine Oligonucleotide Binding Energy by Force Spectroscopy.* Nano Letters, 2008. **8**(12): p. 4365-4372.

71. Zheng, M., et al., *Structure-Based Carbon Nanotube Sorting by Sequence-Dependent DNA Assembly.* Science, 2003. **302**(5650): p. 1545-1548.

72. Stein, D., M. Kruithof, and C. Dekker, *Surface-Charge-Governed Ion Transport in Nanofluidic Channels.* Phys. Rev. Lett., 2004. **93**: p. 035901-1-4.

73. Chow, K.-F., F. Mavre, and R.M. Crooks, *Wireless Electrochemical DNA Microarray Sensor.* J. Am Chem Soc, 2008. **130**: p. 7544-7545.

74. Warakulwit, C., et al., *Dissymmetric Carbon Nanotubes by Bipolar Electrochemistry.* Nano Lett., 2008. **8**: p. 500-504.

75. Smeets, R.M.M., et al., *Noise in Solid State Nanopores.* Proc. Natl. Acad. Sci. (USA), 2008. **105**: p. 417-421.

76. Gatimu, E., et al., *Perturbation of microfluidic transport following electrokinetic injection through a nanocapillary array membrane: Injection and biphasic recovery.* J. Phys. Chem. C, 2008. **112**: p. 19242-19247.

77. Joseph, S. and N.R. Aluru, *Hierarchical multiscale simulation of electrokintetic transport in silica nanochannels at the point of zero charge.* Langmuir, 2006. **22**: p. 9041-9051.

78. Joseph, S. and N.R. Aluru, *Why are carbon nanotubes fast transporters of water?* Nano Lett., 2008. **8**: p. 452-458.

79. Wong, S., et al., *Covalently functionalized nanotubes as nanometre-sized probes in chemistry and biology.* Nature, 1998. **394**: p. 52-55.

80. Chen, Y.-F. and M.S. Fuhrer, *Tuning from Thermionic Emission to Ohmic Tunnel Contacts via Doping in Schottky-Barrier Nanotube Transistors.* Nano Lett., 2006. **9**: p. 2158-2162.

81. Heller, I., et al., *Individual single-walled carbon nanotubes as nanoelectrodes for electrochemistry.* Nano Lett., 2005. **5**: p. 137-142.

82. Dekker, C., *Solid-state nanopores.* Nature Nanotechnology, 2007. **2**(4): p. 209-215.

83. Fan, R., et al., *DNA Translocation in Inorganic Nanotubes.* Nano Lett., 2005. **5**: p. 1633-1637.

84. Jin, X., et al., *Induced electrokinetic transport in micro-nanofluidic interconnect devices.* Langmuir, 2007. **23**: p. 13209-13222.

85. Jin, X., et al., *Induced Electrokinetic Transport in Micro-Nanofluidic Interconnect Devices.* Langmuir, 2007. **23**(26): p. 13209-13222.

86. Kim, S.J., et al., *Concentration Polarization and Nonlinear Electrokinetic Flow near a Nanofluidic Channel.* Physical Review Letters, 2007. **99**(4): p. 044501.

87. Kong, J., et al., *Nanotube Molecular Wires as Chemical Sensors.* Science, 2000. **287**(5453): p. 622-625.

88. Douglas, R.K. and S. Alexander, *Carbon Nanotube Gas and Vapor Sensors.* Angew. Chem. Int. Edit., 2008. **47**(35): p. 6550-6570.

89. Wenrong, Y., et al., *Carbon Nanomaterials in Biosensors: Should You Use Nanotubes or Graphene?* Angew. Chem. Int. Edit., 2010. **49**(12): p. 2114-2138.

90. Dujardin, E., et al., *Capillarity and Wetting of Carbon Nanotubes.* Science, 1994. **265**(5180): p. 1850-1852.

91. Erik, D., et al., *Wetting of Single Shell Carbon Nanotubes.* Adv. Mater., 1998. **10**(17): p. 1472-1475.

92. Joseph, S. and N.R. Aluru, *Why Are Carbon Nanotubes Fast Transporters of Water?* Nano Lett., 2008. **8**(2): p. 452-458.

93. Naguib, N., et al., *Observation of Water Confined in Nanometer Channels of Closed Carbon Nanotubes.* Nano Lett., 2004. **4**(11): p. 2237-2243.

94. Cambr, et al., *Experimental Observation of Single-File Water Filling of Thin Single-Wall Carbon Nanotubes Down to Chiral Index (5,3).* Phys. Rev. Lett., 2010. **104**(20): p. 207401.

95. Chen, Q., et al., *Identification of Endohedral Water in Single-Walled Carbon Nanotubes by 1H NMR.* Nano Lett., 2008. **8**(7): p. 1902-1905.

96. Maniwa, Y., et al., *Water-Filled Single-Wall Carbon Nanotubes as Molecular Nanovalves.* Nat. Mater., 2007. **6**(2): p. 135-141.

97. Byl, O., et al., *Unusual Hydrogen Bonding in Water-Filled Carbon Nanotubes.* J. Am. Chem. Soc., 2006. **128**(37): p. 12090-12097.

98. Kolesnikov, A.I., et al., *Anomalously Soft Dynamics of Water in a Nanotube: A Revelation of Nanoscale Confinement.* Phys. Rev. Lett., 2004. **93**(3): p. 035503.

99. Whitby, M. and N. Quirke, *Fluid Flow in Carbon Nanotubes and Nanopipes.* Nat. Nano., 2007. **2**(2): p. 87-94.

100. Liang, X. and S.Y. Chou, *Nanogap Detector Inside Nanofluidic Channel for Fast Real-Time Label-Free DNA Analysis.* Nano Lett., 2008. **8**(5): p. 1472-1476.

101. Dekker, C., *Solid-State Nanopores.* Nat. Nano., 2007. **2**(4): p. 209-215.

102. Fan, R., et al., *DNA Translocation in Inorganic Nanotubes.* Nano Lett., 2005. **5**(9): p. 1633-1637.

103. Lee, C.Y., et al., *Coherence Resonance in a Single-Walled Carbon Nanotube Ion Channel.* Science, 2010. **329**(5997): p. 1320-1324.

104. Lee, R.S., et al., *Conductivity enhancement in single-walled carbon nanotube bundles doped with K and Br.* Nature, 1997. **388**(6639): p. 255-257.

105. Staii, C., et al., *DNA-Decorated Carbon Nanotubes for Chemical Sensing.* Nano Lett., 2005. **5**(9): p. 1774-1778.

106. Star, A., et al., *Electronic Detection of Specific Protein Binding Using Nanotube FET Devices.* Nano Lett., 2003. **3**(4): p. 459-463.

107. Heinze, S., et al., *Carbon Nanotubes as Schottky Barrier Transistors.* Phys. Rev. Lett., 2002. **89**(10): p. 106801.

108. Avouris, P., Z. Chen, and V. Perebeinos, *Carbon-Based Electronics.* Nat. Nano., 2007. **2**(10): p. 605-615.

109. Pati, R., et al., *Effect of H_2O Adsorption on Electron Transport in a Carbon Nanotube.* Appl. Phys. Lett., 2002. **81**(14): p. 2638-2640.

110. Na, P.S., et al., *Investigation of the humidity effect on the electrical properties of single-walled carbon nanotube transistors.* Appl. Phys. Lett., 2005. **87**(9): p. 093101.

111. Sung, D., et al., *Ab Initio Study of the Effect of Water Adsorption on the Carbon Nanotube Field-Effect Transistor.* Appl. Phys. Lett., 2006. **89**(24): p. 243110.

112. Kim, W., et al., *Hysteresis Caused by Water Molecules in Carbon Nanotube Field-Effect Transistors.* Nano Lett., 2003. **3**(2): p. 193-198.

113. Zahab, A., et al., *Water-Vapor Effect on the Electrical Conductivity of a Single-Walled Carbon Nanotube Mat.* Phys. Rev. B, 2000. **62**(15): p. 10000.

114. Heller, I., et al., *Optimizing the Signal-to-Noise Ratio for Biosensing with Carbon Nanotube Transistors.* Nano Lett., 2009. **9**(1): p. 377-382.

115. Cui, X., et al., *Controlling Energy-Level Alignments at Carbon Nanotube/Au Contacts.* Nano Lett., 2003. **3**(6): p. 783-787.

116. Douglas, R.K. and S. Alexander, *Carbon Nanotube Gas and Vapor Sensors.* Angewandte Chemie International Edition, 2008. **47**(35): p. 6550-6570.

117. Bradley, K., et al., *Influence of Mobile Ions on Nanotube Based FET Devices.* Nano Lett., 2003. **3**(5): p. 639-641.

118. Zuo, G., et al., *Transport Properties of Single-File Water Molecules inside a Carbon Nanotube Biomimicking Water Channel.* ACS Nano, 2009. **4**(1): p. 205-210.

119. Joseph, S. and N.R. Aluru, *Pumping of Confined Water in Carbon Nanotubes by Rotation-Translation Coupling.* Phys. Rev. Lett., 2008. **101**(6): p. 064502.

120. Chang, Y.W., J. Sony, and N.R. Aluru, *Effect of Quantum Partial Charges on the Structure and Dynamics of Water in Single-Walled Carbon Nanotubes.* J. Chem. Phys., 2006. **125**(11): p. 114701.

121. Kolesnikov, A.I., et al., *Anomalously Soft Dynamics of Water in a Nanotube: A Revelation of Nanoscale Confinement.* Physical Review Letters, 2004. **93**(3): p. 035503.

122. Lu, D., et al., *Finite-Size Effect and Wall Polarization in a Carbon Nanotube Channel.* Nano Letters, 2004. **4**(12): p. 2383-2387.

123. Yang, M.H., et al., *Carbon Nanotube Schottky Diode and Directionally Dependent Field-Effect Transistor Using Asymmetrical Contacts.* Appl. Phys. Lett., 2005. **87**(25): p. 253116.

124. Marcus, F., et al., *Controlled Creation of a Carbon Nanotube Diode by a Scanned Gate.* Appl. Phys. Lett., 2001. **79**(20): p. 3326-3328.

125. Majumder, M., N. Chopra, and B.J. Hinds, *Effect of Tip Functionalization on Transport through Vertically Oriented Carbon Nanotube Membranes.* J. Am. Chem. Soc., 2005. **127**(25): p. 9062-9070.

126. Fornasiero, F., et al., *Ion Exclusion by Sub-2-nm Carbon Nanotube Pores.* P. Natl. Acad. Sci., 2008. **105**(45): p. 17250-17255.

127. Kendall, R.A., et al., *High Performance Computational Chemistry: An Overview of NWChem a Distributed Parallel Application.* Comput. Phys. Commun., 2000. **128**(1-2): p. 260-283.

128. Biswas, P.K. and V. Gogonea, *A Regularized and Renormalized Electrostatic Coupling Hamiltonian for Hybrid Quantum-Mechanical--Molecular-Mechanical Calculations.* J. Chem. Phys., 2005. **123**(16): p. 164114.

129. Staii, C., et al., *DNA-Decorated Carbon Nanotubes for Chemical Sensing.* Nano Letters, 2005. **5**(9): p. 1774-1778.

130. Star, A., et al., *Electronic Detection of Specific Protein Binding Using Nanotube FET Devices.* Nano Letters, 2003. **3**(4): p. 459-463.

131. Heller, I., et al., *Optimizing the Signal-to-Noise Ratio for Biosensing with Carbon Nanotube Transistors.* Nano Letters, 2009. **9**(1): p. 377-382.

132. Cui, X., et al., *Controlling Energy-Level Alignments at Carbon Nanotube/Au Contacts.* Nano Letters, 2003. **3**(6): p. 783-787.

133. Qin, X., et al., *Measurement of the Rate of Water Translocation through Carbon Nanotubes.* Nano letters, 2011. **11**(5): p. 2173-2177.

134. Jiang, Z. and D. Stein, *Electrofluidic Gating of a Chemically Reactive Surface.* Langmuir, 2010. **26**(11): p. 8161-8173.

135. Nishizawa, M., V.P. Menon, and C.R. Martin, *Metal Nanotubule Membranes with Electrochemically Switchable Ion-Transport Selectivity.* Science, 1995. **268**(5211): p. 700-702.

136. Wei, R., et al., *Fabrication of Metallized Nanopores in Silicon Nitride Membranes for Single-Molecule Sensing.* Small, 2010. **6**(13): p. 1406-1414.

137. Schneider, G.F., et al., *DNA Translocation through Graphene Nanopores.* Nano Letters, 2010. **10**(8): p. 3163-3167.

138. Napoli, M., J.C.T. Eijkel, and S. Pennathur, *Nanofluidic technology for biomolecule applications: a critical review.* Lab on a Chip, 2010. **10**(8): p. 957-985.

139. Merchant, C.A., et al., *DNA Translocation through Graphene Nanopores.* Nano Letters, 2010. **10**(8): p. 2915-2921.

140. Matthew, R.L., et al. *Fabrication and characterization of carbon nanotube field-effect transistor biosensors*. 2010. SPIE.

141. Huang, S.-C.J., et al., *Carbon Nanotube Transistor Controlled by a Biological Ion Pump Gate.* Nano Letters, 2010. **10**(5): p. 1812-1816.

142. Polking, M.J., et al., *Controlled Synthesis and Size-Dependent Polarization Domain Structure of Colloidal Germanium Telluride Nanocrystals.* Journal of the American Chemical Society, 2011. **133**(7): p. 2044-2047.

143. Baumgardner, W.J., et al., *SnSe Nanocrystals: Synthesis, Structure, Optical Properties, and Surface Chemistry.* Journal of the American Chemical Society, 2010. **132**(28): p. 9519-9521.

144. Franzman, M.A., et al., *Solution-Phase Synthesis of SnSe Nanocrystals for Use in Solar Cells.* Journal of the American Chemical Society, 2010. **132**(12): p. 4060-+.

145. Greyson, E.C., J.E. Barton, and T.W. Odom, *Tetrahedral zinc blende tin sulfide nanoand microcrystals.* Small, 2006. **2**(3): p. 368-371.

146. Antunez, P.D., J.J. Buckley, and R.L. Brutchey, *Tin and germanium monochalcogenide IV-VI semiconductor nanocrystals for use in solar cells.* Nanoscale, 2011. **3**(6): p. 2399-2411.

147. Xu, Y., et al., *Synthesis of SnS Quantum Dots.* Journal of the American Chemical Society, 2009. **131**(44): p. 15990-+.

148. Hickey, S.G., et al., *Size and Shape Control of Colloidally Synthesized IV-VI Nanoparticulate Tin(II) Sulfide.* Journal of the American Chemical Society, 2008. **130**(45): p. 14978-+.

149. Brus, L., *Solid state chemistry - Metastable dense semiconductor phases.* Science, 1997. **276**(5311): p. 373-374.

150. Burda, C., et al., *Chemistry and properties of nanocrystals of different shapes.* Chemical Reviews, 2005. **105**(4): p. 1025-1102.

151. Zhang, Y., et al., *Ultralarge single crystal SnS rectangular nanosheets.* Chemical Communications, 2011. **47**(18): p. 5226-5228.

152. Biswas, P.K. and V. Gogonea, *A regularized and renormalized electrostatic coupling Hamiltonian for hybrid quantum-mechanical--molecular-mechanical calculations.* The Journal of Chemical Physics, 2005. **123**(16): p. 164114.

153. Koktysh, D.S., J.R. McBride, and S.J. Rosenthal, *Synthesis of SnS nanocrystals by the solvothermal decomposition of a single source precursor.* Nanoscale Research Letters, 2007. **2**(3): p. 144-148.

154. Deng, Z., H. Yan, and Y. Liu, *Controlled Colloidal Growth of Ultrathin Single-Crystal ZnS Nanowires with a Magic-Size Diameter.* Angewandte Chemie International Edition, 2010. **49**(46): p. 8695-8698.

155. Talapin, D.V., et al., *Seeded growth of highly luminescent CdSe/CdS nanoheterostructures with rod and tetrapod morphologies.* Nano Letters, 2007. **7**(10): p. 2951-2959.

156. Coropceanu, V., et al., *Charge transport in organic semiconductors.* Chemical Reviews, 2007. **107**(4): p. 926-952.

157. Fardy, M., et al., *Synthesis and thermoelectrical characterization of lead chalcogenide nanowires.* Advanced Materials, 2007. **19**(19): p. 3047-+.

158. Lee, J.-S., et al., *Band-like transport, high electron mobility and high photoconductivity in all-inorganic nanocrystal arrays.* Nature Nanotechnology, 2011. **6**(6): p. 348-352.

159. Lu, C. and J. Liu, *Controlling the Diameter of Carbon Nanotubes in Chemical Vapor Deposition Method by Carbon Feeding.* The Journal of Physical Chemistry B, 2006. **110**(41): p. 20254-20257.

160. Stuart, L. and et al., *Recognition tunneling.* Nanotechnology, 2010. **21**(26): p. 262001.

161. Senturia, S.D., *MICROSYSTEM DESIGN* Springer, 2001.

162. Coldewey, D., *Intel's 3D Transistors Promise Small Physical And Electrical Footprint.* http://techcrunch.com/, 2011.

163. Feynman, R., *There's Plenty of Room at the Bottom* the 1959 meeting of the American Physical Society at Caltech, 1959.

APPENDIX A

SAMPLE EBL PROGRAM FILES

Sample jdf and sdf file for EBL exposure

A: jdf file for PMMA making gold alignment marker

```
JOB 'CNT_MARKER',2.0
PATH   WEI01     ;Initial Check (INIMSH,PDEF)
 ARRAY (0,1,0)/(0,1,0) ;only one pattern, 1 row and 1 column
  ASSIGN P(1)->(*,*)
 AEND
PEND

LAYER 1
 P(1)  'CNT_marker_small' ;choose pattern
 EOS   7,'U50_500pA'  ;choose mode
SHOT   A,4
RESIST 540,4  ; Area(uC/cm2) , Line(nC/cm) for PMMA

END
```

B: jdf file for PMMA making reservoirs

```
JOB 'SINGLE_RESERVIOR', 2.0

 GLMPOS    P=(-4955,-370), Q=(4845,-370)   ;coordinate of P&Q alignment marker
 GLMP      8.0,30,1,0 ; P Mark  width = 8um   Length = 30um
 GLMQRS    8.0,30,1,0 ; Q Mark  width = 8um   Length = 30um

 PATH   WEI01         ;Auto CALIB Menu File   Initial Check (INIMSH,PDEF)

  ARRAY   (-4919,71,140)/(4849.5,43,230) ;use up left corner as start point,
define 71 rows and 43 columns
  ASSIGN  P(1) -> (56,9)  ;put the row and column number here
  ASSIGN  P(2) -> (56,5)
  ASSIGN  P(3) -> (56,2)
  ASSIGN  P(4) -> (57,4)
  ASSIGN  P(5) -> (58,6)
  ASSIGN  P(6) -> (60,8)
  ASSIGN  P(7) -> (61,11)
  ASSIGN  P(8) -> (61,7)
  ;define control reservoirs
  ASSIGN  P(13) -> (40,9)
  ASSIGN  P(14) -> (40,10)
  ASSIGN  P(15) -> (40,11)
  AEND

 PEND

 LAYER          1

 P(1)   'SINGLE_RESERVOIR_2UM'(33,-22.8)     ;define reservoir pattern, put the
coordinate x,y here
 P(2)   'SINGLE_RESERVOIR_2UM'(56.2,-31.5)
 P(3)   'SINGLE_RESERVOIR_5UM'(42.5,20.8)
 P(4)   'SINGLE_RESERVOIR_2UM'(18,-17.5)
 P(5)   'SINGLE_RESERVOIR_2UM'(5.7,-61.9)
 P(6)   'SINGLE_RESERVOIR_2UM'(11.8,-31.76)
 P(7)   'SINGLE_RESERVOIR_2UM'(59.8,-18.75)
 P(8)   'SINGLE_RESERVOIR_2UM'(19.5,14)
```

```
 ;control
 P(13)   'SINGLE_RESERVOIR_5UM'
 P(14)   'SINGLE_RESERVOIR_2UM'
 P(15)   'SINGLE_RESERVOIR_2UM'

 EOS     7,'U50_100pA'                 ; Mode, Condition Name for 50kv 5th LENS
 SHOT    A,4                           ; Shot Time (Auto) , Np (Point)
 RESIST  550,4                         ; Area(uC/cm2) , Line(nC/cm) for PMMA
 END

END
```

C: sdf file, making alignment marker and open reservoirs are similar

```
MAGAZIN ' '

#1
 %2C
 JDF     'SINGLE_RESERVIOR',1     ;choose the job file
 EOS     7,'U50_100pA'
 GLMDET  M                         ;use manual alignment
 OFFSET  (0,0)

END  1
```

Note: For EBL equipment initialization, first choose EOSSET, use ‘50U_500pA’ mode 7. Second, set current to 500pA. Then focus on mesh mark, burn a dot on chip surface (SEI rapid scan mode, MAG: 87, SPD: 00, brightness: 540, contrast: 720, wait for 3min for PMMA, half time for ZEP), fine focus on the dot. When ready for expose, apply INIMSH, PDEF, DISTOR. Finally load mgn file to expose. The exposure time is usually overnight, higher current is encouraged to use to short the time.

APPENDIX B

CO-AUTHOR APPROVAL

VERIFICATION OF CO-AUTHOR APPROVALS

I verify that the following co-authors have approved of my use of our publications in my dissertation.

Stuart Lindsay	(Arizona State University)
Jin He	(Arizona State University)
Pei Pang	(Arizona State University)
Hao Liu	(Arizona State University)
Tao Luo	(Arizona State University)
Zhengtao Deng	(Arizona State University)
Hao Yan	(Arizona State University)
Yan Liu	(Arizona State University)
Colin Nuckolls	(Columbia University)
Jinyao Tang	(Columbia University)
Predrag Krstic	(Oak Ridge National Laboratory)
Sony Joseph	(Oak Ridge National Laboratory)
Jae Hyun Park	(Oak Ridge National Laboratory)

Note: The author's address is listed as when the research was performed.

BIOGRAPHICAL SKETCH

Di Cao was born in Xiangfan, Hubei Province, China in 1983. He was brought up by a dream to be a scientist. He began his journey in the palace of science with a book of Jules Verne's science fiction: *Captain Grant's Children.* In the middle school, he eagerly explored every culture subject, including literature and history. He loves reading and travelling, to experience the diversity of the world. He likes climbing and realized a dream to climb the Everest in Tibet several years later. He showed the better understanding in the Physics and Mathematics. And at that time he established long term goals to get further education and use his learning to increase individual influence and public benefits. In high school, he won the National First Prize of 18th Chinese Physics Olympiad, and then received an offer from University of Science and Technology of China (USTC) for exempting the university entrance examination. In there, he heard lots of legendary stories about USTC alumni's achievement in US. So he followed the forth goers' steps and got on board the flight to US. Five years' foreign life increased his insight and knowledge, and also increased his confidence to discover the future. Within the five years, he was shocked by the rising of China, and gave birth to the idea to do something connecting China and US. With the dream impacting the reality, he plans to choose semiconductor or finance industry after finishing PhD. Hope he will have a great adventure in the future.